High-Resolution Analysis of Perovskite Absorbers in Photovoltaics

Dissertation

zur Erlangung des Doktorgrades
der Technischen Fakultät der
Albert-Ludwigs-Universität
Freiburg im Breisgau

vorgelegt von

Laura Elena Mundt

angefertigt am Fraunhofer-Institut für Solare Energiesysteme
Freiburg im Breisgau

2018

Erstgutachter: Prof. Dr. Stefan Glunz

Zweitgutachter: Prof. Dr. Steve Albrecht

Dekanin: Prof. Dr. Hannah Bast

Datum der mündlichen Prüfung: 15.03.2019

All dwelling in one house are strange brothers three,
as unlike as any three brothers could be,
yet try as you may to tell brother from brother,
you'll find that the trio resemble each other.
The first isn't there, though he'll come beyond doubt.
The second's departed, so he's not about.
The third and the smallest is right on the spot,
and manage without him the others could not.
Yet the third is a factor with which to be reckoned
because the first brother turns into the second.
You cannot stand back and observe number three,
for one of the others is all you will see.
So tell me, my friend, are the three of them one?
Or are there but two? Or could there be none?
Just name them, and you will at once realize
that each rules a kingdom of infinite size.
They rule it together and are it as well.
In that, they're alike, so where do they dwell?

Michale Ende, Momo

Table of contents

List of Abbreviations

2T	2-terminal
4T	4-terminal
AC	alternating current
AFM	atomic force microscopy
ALD	atomic layer deposition
AM	air mass
AZO	aluminum-doped Zinc Oxide
BCP	2,9-Dimethyl-4,7-diphenyl-1,10-phenanthroline
CCD	charge coupled device
c-Si	crystalline silicon
cw	continuous wave
DC	direct current
DLIT	dark lock-in thermography
DMF	N,N-dimethylformamide
DMSO	dimethylsulfoxide
DSSC	dye sensitized solar cell
EDX	energy dispersive x-ray spectroscopy
EQE	external quantum efficiency
ETL	electron transport layer
FA	formamidinium
FTO	fluorine doped tin oxide
FWHM	width at half maximum
GI-WAXS	grazing incidence wide angle X-ray scattering
HJ	heterojunction
HTL	hole transport layer
ILIT	illuminated lock-in thermography
IR	infrared
ITO	indium tin oxide
J-V	current-voltage
LBIC	light beam-induced current
LED	light emitting diode
LIT	lock-in thermography

MA	methyl ammonium
MAI	methyl ammonium iodide
MJ	multi junction
MPP	maximum power point
MWIR FPA	midwave infrared focal plane array
NA	numerical aperture
Nd:YAG	neodymium-doped yttrium aluminum garnet; Nd:$Y_3Al_5O_{12}$
NIR	near infrared
OPV	organic photovoltaic
P1	process for flat perovskite morphology
P2	process for moderately wrinkled perovskite morphology
P3	process for heavily perovskite morphology
PCBM	[6,6]-phenyl-C_{61}-butyric acid methyl ester
PEDOT:PSS	poly(3,4-ethylenedioxythiophene) polystyrene sulfonate
PL	photoluminescence
PLS	photoluminescence spectroscopy
PMMA	polymethylmethacrylat
PSC	perovskite solar cell
PTAA	poly[bis(4-phenyl)(2,4,6-trimethylphenyl)amine]
PV	photovoltaic
RMS	root mean square
SEM	scanning electron microscope
SHJ	silicon hetero junction
SJ	single junction
SPAD	single photon avalanche diode
Spiro-OMeTAD	2,2',7,7'-Tetrakis[N,N-di(4-methoxyphenyl)amino]-9,9'-spirobifluorene
SRH	Shockley-Read-Hall
TCO	transparent conductive oxide
TCSPC	time-correlated single photon counting
trPL	time-resolved photoluminescence
UV	ultraviolett
vis	visible

List of Symbols

a	lattice constant
A	amplitude
α	absorption coefficient
B_{rad}	radiative recombination coefficient
β	angle of the light collection cone
c	vaccum velocity of light
c_P	specific heat
χ_e	electron affinity
D_e	density of electron states in the condution band
Δ_n	excess charge carrier density
D_h	density of hole states in the valence band
e	elemenary charge
E_{FC}/E_{FV}	Quasi-Fermi level
E_t	defect energy level
E_C	conduction band energy
E_F	Fermi energy
E_G	bandgap energy
ϵ	dielectric permitivity
ϵ_0	dielectric constant
EQE	external quantum efficiency
η	solar cell conversion efficiency
E_V	valence band energy
F	free energy
$f(E)$	Fermi-Dirac distribution
$f_{lock-in}$	lock-in frequency
FF	fill factor
G	generation rate
G_γ	generation rate from photon absorption
γ	photon
$\hbar$	planck constant
$\hbar\omega$	photon energy
I_{PL}	photoluminescence intensity
j_γ	photon current density

J_{dark}	current density under dark conditions
J_{illum}	current density under illumination
J_{mpp}	current at the maximum power point
J_{sc}	short-cirucit current density
J_{01}	dark saturation current density first diode
J_{02}	dark saturation current density second diode
k	Boltzmann konstant
λ_{th}	heat conductivity
λ	wavelength
Λ	thermal diffusion length
M_{ω}	spectral specific irradiation
m_e	electron mass
m_e^*	effective electron mass
m_h^*	effective hole mass
n_A^-	ionized acceptor density
n_{air}	refractive index of air
n_D^+	ionized donor density
N_t	defect state density
$N_{t,e/h}$	density of occuied surface states per area
NA	numerical aperture
$N_{C/V}$	effective density of states
n_e	electron density in the conduction band
n_{e/h_1}	SRH electron/hole density
n_h	hole density in the valence band
n_i	intrinsic charge carrier density
Ω	solid angle
p	power density
P_{in}	input power from illumination
p_{loc}	local power density
P_{mpp}	power at the maximum power point
P_{whole}	global power density
ϕ	phase
R	recombination rate
R_{γ}	radiative recombination rate

R_p	parallel resistance
R_s	series resistance
R_{SRH}	SRH recombination rate
r_0	ionic radius X-site anion
r_A	ionic radius A-site cation
r_B	ionic radius B-site cation
ρ	density
S	entropy
$S_{e/h}$	surface recombination velocity
$\sigma_{e/h}$	capture cross section for electrons/holes
T	temperature
t_{int}	integration time
T_S	temperature of the sun
τ	lifetime
$\tau_{e0/h0}$	SRH electron/hole lifetime
t_G	Goldschmidt tolerance factor
V_{bias}	bias voltage
V_{mpp}	voltage at the maximum power point
V_{oc}	open-circuit voltage
v_{th}	thermal velocity

Abstract

This thesis discusses studies performed by the author at the Fraunhofer Institute for Solar Energy Systems, ISE. The presented work focuses on the characterization of hybrid organic-inorganic halide perovskite materials used for photovoltaic application.

In an in situ study of the perovskite crystal formation, multiple stages are identified. Taking advantage of a graphite-based cell structure where both contacts are in place before the perovskite crystal formation occurs within the mesoporous scaffold, the photovoltaic performance along with optoelectronic properties are monitored in real time during the crystallization.

As perovskite solar cells are prone to spatial heterogeneity, spatially resolved characterization techniques mainly based on photoluminescence spectroscopy, light beam-induced current and thermography are employed to analyze non-uniform optoelectronic properties and quantify local loss mechanisms.

A novel characterization method is introduced by the author, allowing for the quantitative assessment of local loss mechanisms. The technique is demonstrated on blade coated perovskite solar cells, which represent a scalable deposition route, and it highlights the detrimental impact of layer non-uniformity on the overall solar cell performance. It presents a powerful tool for the targeted improvement of layer homogeneity and consequential benefit the enhancement of the cell efficiency.

In high bandgap perovskite films made from a mixed cation and halide alloy, the local optoelectronic properties are analyzed with micrometer resolution. Non-uniform emission properties are revealed and related to the layer morphology.

A subcell-selective analysis of monolithic two-terminal silicon perovskite tandem solar cells is presented, accessing the individual subcells by multi-wavelength photoluminescence spectroscopy. The mapping approach additionally yields spatial distribution of the photoluminescence emission, allowing for the identification of process influences on the two subcells.

The results from this thesis generated insights about the perovskite crystal formation and spatial heterogeneities on different length scales. Overall, the findings support the targeted optimization of hybrid organic-inorganic halide perovskite solar cells.

Detaillierte deutsche Zusammenfassung

Der Schwerpunkt dieser Arbeit lag auf der Analyse von hybriden organisch-anorganischen Metall-Halogenid Perowskit Absorbern, angefangen bei einzelnen Kristallschichten bis hin zu komplexen Tandemsolarzellen. Das übergreifende Ziel war es, ein umfassendes Verständnis der Material- und Zellparameter zu erzeugen und durch die Qualitätsbewertung der vielfältigen Materialien und Herstellungsprozesse die Effizienz der Solarzellen zu steigern.

Dies wurde durch die Anwendung mehrerer state-of-the-art Charakterisierungs-techniken erreicht, die eine hohe zeitliche und räumliche Auflösung erlauben. Interne und externe Kooperationen ermöglichten den Zugang zu Testproben für alle Untersuchungen im Rahmen dieser Arbeit.

In enger Zusammenarbeit mit mehreren Gruppen innerhalb des Fraunhofer Institut für Solare Energiesysteme wurde eine in-situ-Studie zur Perowskit-Kristallisation durchgeführt. Als Referenzsystem für Perowskite in Photovoltaikanwendungen wurde Methylammoniumbleiiodid als Absorbermaterial für die Untersuchung ausgewählt. Eine graphitbasierte Zellstruktur ermöglichte die Messung der externen Quanten-effizienz während des Kristallisationsprozesses:

Die Zellarchitektur beinhaltete sowohl die Elektronen- als auch die Lochtransportschicht, bereits bevor die Absorberschicht ausgebildet wurde. Zwischen den Kontakten befand sich ein mit PbI_2 gefülltes, mesoporöses Gerüst aus TiO_2 und ZrO_2. Das Eintauchen in Methylammoniumlösung führte daher zu einer sofortigen Einleitung der Perowskitkristallbildung und damit zu einer betriebsbereiten Solarzelle. Die Kinetik dieser Kristallisation wurde durch Echtzeitmessungen der externen Quanteneffizienz sowie des Photolumineszenz-Emissionsspektrums analysiert. Ein wesentliches Ergebnis war die Identifizierung einer zusätzlichen Stufe während der Perowskitbildung, die von früheren Studien zur Perowskitkristallisation übersehen worden war. In diesem Schritt steigt der Photostrom deutlich an, nachdem die Kristallbildung selbst als abgeschlossen angenommen wird. Dieser Anstieg ist auf die Bildung von elektrischen Pfaden zwischen den Elektronen- und Lochkontaktschichten zurückzuführen, die eine effiziente Ladungsträger-Extraktion ermöglichen.

Da es für die Anwendung von Tandemsolarzellen von hoher Relevanz ist, wurde ein Absorbermaterial mit hoher Bandlücke untersucht, welches eine anomale, wurmartige Morphologie aufwies. Die vorgestellte Arbeit war Teil einer umfangreichen, gemeinschaftlichen Studie zusammen mit Wissenschaftlern des Helmholtz-Zentrum Berlin über den Einfluss der Perowskitzusammensetzung und der

Verarbeitungsparameter auf die Morphologie und die optoelektronischen Eigenschaften. Der Beitrag der Autorin zur Studie war die räumlich aufgelöste Analyse der Morphologie und der optoelektronischen Eigenschaften der $Cs_xFA_{1-x}Pb(I_{1-y}Br_y)_3$ Perowskit-Absorberschicht. Mithilfe eines konfokalen Mikroskops wurde die räumliche Auflösung bis zur Brechungsgrenze erhöht. Dadurch ergab die Überlagerung von Rasterelektronenmikroskopbildern mit den spektralen Eigenschaften aus der emittierten Photolumineszenz eine eindeutige Korrelation zwischen der Morphologie und den Photolumineszenz-Emissionseigenschaften. Es wurde festgestellt, dass erhöhten Bereiche im Vergleich zu den flachen Bereichen größere Kristalle und eine leichte Rotverschiebung des Photolumineszenzspektrum aufweisen, was auf eine geringere Spannung im Kristallgitter in den größeren Kristallen zurückzuführen ist. Diese Annahme wurde durch energiedispersive Röntgenspektroskopie-Messungen über den Querschnitt des Films unterstützt. Eine Phasentrennung des Absorbermaterials konnte ausgeschlossen werden, da die Elementverteilung entlang der Morphologie keinen Hinweis auf eine kompositorische Entmischung gab.

Eine wichtige Errungenschaft dieser Arbeit im Bereich der ortsaufgelösten Analysen war die Einführung einer quantitativen lokalen Verlustanalyse, die auf bildgebender Dunkel-Thermographie und lichtinduzierten Strommessungen bei mehreren Anregungswellenlängen basiert. Hiermit wurde der Schritt von der qualitativen Detektion von Heterogenitäten hin zu einer quantitativen Verlustanalyse von Leerlaufspannung, Kurzschlussstrom und dem daraus resultierenden Wirkungsgrad erfolgreich vollzogen. Die Leerlaufspannung wurde durch Anwendung der lokalen Strom-Spannungsanalyse bestimmt, einem etablierten Verfahren zur Charakterisierung von Silizium-Solarzellen. Eine Schätzung der Querverteilung des Kurzschlussstroms wurde durch mehrere ortsaufgelöste Messungen des lichtinduzierten Stroms ermittelt, welche durch externe Quanteneffizienzmessungen gewichtet wurden. Die Technik wurde an Perowskit-Solarzellen mit im Klingenbeschichtungsverfahren abgeschiedener Absorberschicht und einer aktiven Zellfläche von $1.1\,cm^2$ demonstriert. Es wurden zwei Zellen ausgewählt, die verschiedene Stufen der Prozessoptimierung repräsentieren. Als Architektur der Zellen wurde eine planare invertierte (p-i-n) Struktur mit verschiedenen Lochtransportmaterialien: PEDOT:PSS oder NiO_x gewählt. Nachdem in einem frühen Stadium der Prozessoptimierung ein Randverlust von ca. 1% des absoluten Zellwirkungsgrades für die PEDOT:PSS-Zelle festgestellt wurde, konnte der Herstellungsprozess angepasst werden, was zu einem deutlich reduzierten Randverlust

führte. Dennoch wurde für beide Zellen festgestellt, dass die Heterogenität den Gesamtwirkungsgrad der Zellen um etwa 3% im absoluten Zellwirkungsgrad verringert. Daraus wurde geschlossen, dass die Optimierung der Zellleistung entscheidend von der Verbesserung der Schichthomogenität abhängt.

Bei der ortsaufgelösten Analyse von Mehrfachsolarzellen war das Hauptziel, die Tiefenauflösung durch schichtselektive Anregung zu ermöglichen. Es wurde eine photolumineszenzbasierte Analyse monolithischer Tandemsolarzellen, die durch das Helmholtz-Zentrum Berlin zur Verfügung gestellt wurden, durchgeführt. Die Zellen bestanden aus einer planaren Perwskit-Solarzelle und einer Silizium-Heteroübergangssolarzelle. Die Querverteilung der Heterogenitäten konnte eindeutig auf die einzelnen Teilzellen und darüber hinaus auf die Fertigungsschritte zurückgeführt werden. Der Ansatz der tiefenselektiven Sondierung der Silizium-Solarzelle wurde durch einen Vergleich eines reflexionsgedämpfenten Bildes und, für einen abschließenden Proof-of-Principle, durch eine Messung der Silizium-Solarzelle nach Entfernen der Perowskit-Solarzelle verifiziert.

Zusammenfassend lässt sich sagen, dass die Studien wertvolle Erkenntnisse für die gezielte Optimierung von organisch-anorganischen Metall-Halogenid Perowskit-solarzellen liefern.

Die vorgestellten Techniken sind wichtige Werkzeuge für die Charakterisierung verschiedener Solarzellenarchitekturen. Die Untersuchung einzelner Teilzellen durch Anregung mit verschiedenen Wellenlängen ist eine geeignete Messmethode für siliziumbasierte Tandemsolarzellen sowie reine Perowskit-Tandemsolarzellen. Dieser Ansatz kann außerdem auf andere bildgebende Messverfahren wie die Hell-Thermographie und die Messung des lichtstrahlinduzierten Stroms ausgedehnt werden.

Als weitere wichtige Herausforderung in der Perowskit-Forschung wird die Skalierung der aktiven Zellfläche vom Labormaßstab auf Wafergröße nach wie vor durch Heterogenitätsverluste erschwert. Die Erhöhung des Skalierungsfaktors, d.h. des Verhältnisses von Zellwirkungsgrad und Zellfläche, wird durch die Identifizierung und Quantifizierung lokaler Effizienzverluste unterstützt.

Daher sind umfassende und räumlich aufgelöste Analysen auch für die zukünftige Perowskitforschung unerlässlich.

1 Introduction

1.1 Motivation

“Early experiments with semiconductors were hampered by the extreme sensitivity of the electronic properties to minute concentrations of impurities. Semiconductors were viewed as a family of solids with irreproducible properties.” – Hans J. Queisser [1]

64 years after Bell Labs announced the invention of the first practical silicon solar cell, no one doubts the significance of this technology, nor its reproducibility even though there has been great skepticism in the early days of semiconductor research as H.J. Queisser indicated. A continuous increase in the share of electricity production in Germany and worldwide brings the share of renewable energy sources to 40.3% in 2018, the solar share being 8.9% [2]. While silicon based solar cells provide the majority of this electricity production, the prospective growth demands novel solar cells technologies that allow for even higher energy conversion efficiencies at the same or even lower costs. In recent years, one very promising candidate has emerged from the realm of dye sensitized and organic photovoltaic (PV) technologies. Holding greatly valued physical properties such as a strong absorption with small Urbach energies, hybrid halide perovskite solar cells (PSCs) have great potential as shown by demonstrated energy conversion efficiencies increasing from 3.8% in 2009 to 22.7% in 2017 [3, 4]. Another formidable property of this material is its bandgap tunability which can be adjusted either by chemistry or dimensionality [5–12]. Hence, the material is advantageous for the application in a silicon-based tandem architecture [13–18]. Tandem solar cells have the potential to surpass the Shockley-Queisser limit for single junction (SJ) solar cells, allowing for conversion efficiencies exceeding 30%. They are predicted to be a market-relevant technology in the near future [19]. In 2018, the record conversion efficiency of a two-terminal perovskite silicon tandem solar cell by Oxford Photovoltaics exceeded the record for a SJ silicon solar cell for the first time [20]. Despite the undeniable great potential of this still adolescent technology, skeptics remain throughout the PV community just as semiconductors have once been viewed as a family with irreproducible properties when they were “discovered”. In perovskites, this lack of reproducibility is due to the low formation energy and soft lattice which results in ion movement and chemical degradation, which is accelerated by moisture, oxygen, light and an electric field [21–25]. These phenomena can be mitigated by use of alloys, such as formamidinium (FA)/Cs or I/Br compositions [26–33]. Despite the immense progress in both efficiency and stability, most achievements are phenomenological results rather than outcomes based on

fundamental understanding of the material. To further such fundamental understanding, access to the chemical, structural, optical and electronic properties in perovskite films and solar cells is of crucial importance. Due to various peculiarities of this novel photovoltaic technology, concerning transient behavior [21–23, 34–43] and the predisposition for spatial heterogeneity [44–60] the development of advanced characterization techniques that account for these peculiarities is necessary to investigate the properties of interest. Both the transient behavior and the non-uniformity occur across multiple orders of magnitude, charge carrier lifetimes of nanoseconds to long-term degradation over days and spatial expansion from nanometer wide grain boundaries to process heterogeneities in large-area modules in the order of decimeters. Hence, it is essential for time and spatially resolved characterization techniques to be able to cover numerous orders of magnitude.

1.2 Thesis structure

The thesis' title reflects the overarching topic addressed in this work, which is the analysis of different dimensions in perovskite materials used as absorber in photovoltaic devices. The investigations performed by the author pursued the overall goal of generating in-depth understanding and enabling targeted optimization of perovskite solar cells. The investigations conducted during this thesis covered a large span of topics, from the formation of perovskite crystals to the analysis of complex tandem device structures.

For this monograph, the four investigated dimensions, time and space, were grouped to three major sections, related to temporal, lateral and depth resolution. Each section presents and discusses selected studies out of the work of the author that demonstrate the relevance and value of high-resolution analyses for current key topics in perovskite research.

Methyl ammonium lead iodide ($MAPbI_3$) is the most-analyzed perovskite absorber material and frequently serves as a reference system for other perovskite material. Therefore, it was chosen for an in situ study of the perovskite crystal formation.

To date, common lab-scale PSCs feature active cell areas still well below 1 cm^2 and increasing the area is generally accompanied by a significant reduction of the cell efficiency. As a roll-to-roll compatible process, blade coating is a highly relevant deposition route with regard to upscaling efforts. Therefore, blade coated PSCs were chosen for a spatially resolved loss analysis.

Both silicon-based and all perovskite tandem solar cells are a major and possibly even the most important application for PSCs due to their high efficiency-potential.

Nevertheless, a tandem device is a complex interplay of a large number of functional layers and it is often challenging to determine the origin of malfunctions. Also the bandgaps of the two absorber layers need to be well-matched. Therefore, studies related to high bandgap absorber material and to in-depth characterization of tandem devices are presented in this thesis.

The monograph is structured in the following chapters:

The most relevant theoretical principles and concepts are introduced in the **first chapter**. The chapter covers a range from electron densities in semiconductors to the derivation of charge carrier dynamics, introducing the basic working principle of solar cells and, in continuation, tandem solar cells. Since perovskite materials and solar cells are the main material system investigated in this work, the history of this material's development is briefly introduced along with an overview of the most relevant cell architectures, absorber materials and the corresponding optoelectronic properties.

The fabrication of materials and solar cells was not part of this work. Therefore, the processing details in the thesis' main body are restricted to the minimum required for the analysis and the interpretation of the results. Further details are given in the appendix.

The **second chapter** discusses the time regime. An in situ study of the crystallization of $MAPbI_3$ in a two-step deposition process is presented. The process of perovskite crystallization and its correlation to the photovoltaic performance is one of the fundamental questions in perovskite-related research. By employing a special, graphite-based monolithic device structure, an in situ study of the electric and optoelectronic properties during the crystallization was made possible. Monitoring the temporal evolvolution of the external quantum efficiency and the photoluminescence emission during the manufacturing steps lead to the discovery of a hitherto unknown stage in the crystallization and contact formation. This has contributed to an improved general model concept of $MAPbI_3$ crystal formation.

In the **third chapter**, two examples were chosen to demonstrate the impact of spatial heterogeneities on different length-scales

First, a micrometer-resolution analysis of high-bandgap perovskite absorber with particular micro-morphology is presented. Both global and local optoelectronic properties were investigated and correlated to the film morphology. Non-uniform

photoluminescence emission properties suggest the influence of strain in the perovskite crystals, which in turn strongly depends on the processing conditions.

Second, a novel quantitative analysis of current and voltage losses across the solar cell together with a comprehensive analysis of efficiency loss mechanisms is suggested. It is demonstrated on blade coated perovskite solar cells with an active cell area of 1.1 cm^2. The technique assesses the severity of local heterogeneities and their impact on solar cell performance and ultimately fosters the development of high-efficiency devices.

The **fourth chapter** discusses a multi-wavelength excitation approach to characterize silicon perovskite tandem solar cells with depth resolution. It not only provides spatial resolution but also allows for the separation of signals from the two subcells, hence exploiting all three dimensions of space. By subcell-selective excitation with suitable wavelengths, the photoluminescence emission can be collected individually for both cells.

The **appendix** contains details about the cell fabrication, the manufacturing of materials and cells was not part of this thesis. If a detailed discussion of the fabrication process is available elsewhere, the reader is referred to the corresponding journal publication.

2 Fundamentals

A range of theoretical principles and concepts that are essential for the understanding of the work presented in this thesis are introduced in this chapter. The first part is a general introduction of the physics of semiconductors and the application in photovoltaics. The second part gives an encompassing overview of hybrid organic-inorganic perovskite materials with its characteristic optoelectronic properties and relevant device architectures.

The methodologies employed within this thesis strongly rely on the analysis of charge carrier dynamics in semiconductors and interactions across junctions to functional charge extraction layers. Hence, it is convenient to start with an introduction to the electronic properties of semiconductors as well as the generation and recombination mechanisms of charge carriers. Since this work involves the analysis of single- and multijunction solar cells, the electrical characteristics and specific features for both cell types are introduced.

Halide perovskite solar cells and related materials are the main object of investigation within this thesis, yet there is a large variety in the specific samples, ranging over various chemical compositions, device architectures and deposition techniques that can have significant influence on the properties of interest. Therefore it is essential to establish context, introduce and highlight the differences of materials, deposition techniques and device architectures, which will be relevant in the course of this monograph. Due to the novelty of perovskite photovoltaics, a brief historical introduction is given.

2.1 Semiconductors for Photovoltaics

The first section is dedicated to lay the fundaments for the physical description of electronic states in semiconductors. If no references are stated explicitly, the following section is based on the theoretical framework introduced by Würfel [61].

2.1.1 Electronic Properties

In contrast to the discrete energy states of single atoms, the energy states of the many electrons in a crystal lattice overlap to bands of allowed energies. The regular distance between the atoms in a crystal lattice determines the strength of the electron-electron interaction and thereby the width of the energy bands. In semiconductors, gaps of quantum mechanically “forbidden” energy states separate these energy bands. The highest, at zero temperature completely occupied band is the valence band, with its highest energy state referred to as the valence band edge E_V. The closest band above the forbidden gap is the conduction band, with the lowest energy state referred to as conduction band edge E_C. Determined by the energetic difference of the edge of

valence and conduction band, the bandgap is $E_G = E_C - E_V$. The characteristic difference between semiconductors and isolators is, whether thermal excitation at room temperature is sufficient to cause relevant occupation of states in the conduction band. Free states in the conduction band are referred to as holes and can in principle be regarded as quasi charge carriers with a single positive charge.

For electrons in the conduction band and holes in the valence band, the density of allowed energetic states $D_{e/h}(E)$ can be derived as

$$D_e(E) = \frac{(2m_e^*)^{3/2}}{2\pi^2\hbar^2}(E - E_C)^{1/2} \tag{2.1}$$

$$D_h(E) = \frac{(2m_h^*)^{3/2}}{2\pi^2\hbar^2}(E_V - E)^{1/2} \tag{2.2}$$

with $\hbar$ denoting the Planck constant and $m_{e/h}^*$ the effective mass for electrons and holes, respectively. The effective mass accounts for deviations from the unperturbed electron gas and is defined by the band curvature.

Regarding the occupation of energy states, several conditions need to be taken into account. Electrons and holes are non-integer spin particles. Therefore not more than a single particle can be in one quantum state according to the Pauli Exclusion Principle. Further, the occupation of states is a function of energy and must minimize the free energy $F = E - TS$, with the temperature T and the entropy S.

As a result of the Pauli Exclusion Principle and the minimization of F, the probability for the occupation of an energy state E is given by the Fermi-Dirac distribution $f(E)$:

$$f(E) = \frac{1}{exp\left(\frac{E - E_F}{kT}\right) + 1} \tag{2.3}$$

Here, k denotes the Boltzmann constant. The Fermi energy E_F describes the energy value for which $f(E_F) = 0.5$. At zero temperature $T = 0\ K$, all states above the Fermi energy are occupied and all states below it unoccupied:

$$f(E) = \begin{cases} 0, & E < E_F \\ 1, & E > E_F \end{cases} \tag{2.4}$$

Integration of the product of $D_{e/h}(E)$ and the occupation probability f over all energy states yields the density of electrons in the conduction band n_e and the density of holes in the valence band n_h, respectively.

$$n_e = \int_{E_C}^{\infty} D_e(E) f(E)\, dE \tag{2.5}$$

For $E_C - E_F \gg kT$, the Boltzmann-approximation can be applied, leading to the expression

$$n_e = N_C exp\left(-\frac{E_C - E_F}{kT}\right) \tag{2.6}$$

$$n_h = N_V exp\left(-\frac{E_F - E_V}{kT}\right) \tag{2.7}$$

$$N_{C/V} = 2\left(\frac{m^*_{e/h} kT}{2\pi\hbar^2}\right)^{3/2} \tag{2.8}$$

The prefactors $N_{C/V}$ are referred to as effective density of states. Remarkably, the product of electron density in the conduction band and hole density in the valence band is independent of the Fermi energy, it is known as the intrinsic charge carrier density n_i^2. In semiconductors, where all conduction band electrons originate from the valance band, the density of electrons and holes are equal, it is $n_e = n_h$.

$$n_e n_h = n_i^2 = N_C N_V exp\left(-\frac{E_G}{kT}\right) \tag{2.9}$$

These charge carrier densities can be manipulated by introducing atoms of a different species into the lattice. Atoms with one valance electron more than required for chemical bonding to the neighboring atoms are electrical donors. The electrical Coulomb bond of the "extra" electron to its atom can be described similar to an electron in a Hydrogen atom. Then the mass m_e is replaced by the effective mass m_e^* and the dielectric permittivity ε_0 complemented by the permittivity of the respective semiconductor ε. The resulting ionization energy of such dopant atoms then ends up slightly below the lower edge of the conduction band and it donates its additional electrons easily to the conduction band. In case the impurity atoms features one valence electron less than required for the chemical bonds, the resulting unoccupied orbital can be filled by electrons again resulting in an easy ionization of the dopant atom. In analogy to the donor, the resulting energy level differs only slightly from the upper valence band edge and therefore accepts electrons from the valence band, increasing the hole density in the valence band. Thus, these species are called acceptors.

By doping a semiconductor, the electrical conductivity can be increased. However, due to the remaining ionized dopant atom the crystal stays neutral. The occupation of

states is still determined by the Fermi-Dirac distribution, hence the densities of ionized donors and acceptors are functions of the Fermi energy. As a consequence to the semiconductor's neutrality, the sum of electron/hole and ionized donor/acceptor densities (n_A^- and n_D^+) must be equal.

$$n_e + n_A^- = n_h + n_D^+ \tag{2.10}$$

In the case of an illuminated semiconductor at room temperature, electrons from the valence band are excited to the conduction band. The density of electrons in the conduction band increases and thus the Fermi level is shifted towards the conduction band. However, simultaneously the density of holes in the valence band is increased, which would shift the Fermi level towards the valence band.

As a result, the occupation of states in the energy bands can be described using two different, so-called Quasi-Fermi distributions with different Quasi-Fermi energies $E_{F,C}$ and $E_{V,F}$, respectively.

$$n_e = N_C exp\left(-\frac{E_C - E_{FC}}{kT}\right) \tag{2.11}$$

$$n_h = N_V exp\left(-\frac{E_{FV} - E_V}{kT}\right) \tag{2.12}$$

The difference between the charge carrier densities in thermal equilibrium $n_{e/h}^0$ and the illuminated case $n_{e/h}$ is quantified by the excess charge carrier density $\Delta n_{e/h}$.

$$\Delta n_{e/h} = n_{e/h} - n_{e/h}^0 \tag{2.13}$$

2.2 Charge Carrier Dynamics

The dynamic equilibria of charge carriers in semiconductors are crucial for the photovoltaic performance of solar cells. They can be probed by luminescence-based characterization techniques. As these are central tools employed the this thesis, the generation and different recombination mechanisms in crystalline semiconductors are introduced here.

2.2.1 Generation

Besides thermal excitation of electrons from the valence band to the conduction band as a statistical process, energy can be transferred to the crystal lattice via illumination.

Thus, electrons can be excited from the valence band to the conduction band, given the supplied energy is larger than the bandgap. Generation of electron-hole pairs via the absorption of photons is the most relevant generation process in semiconductors for PV application:

$$\gamma \rightarrow e + h \tag{2.14}$$

The probability of absorbing a photon with energy $\hbar\omega$ is given by the absorption coefficient $\alpha(\hbar\omega)$. The absorption coefficient is defined by the penetration depth of light depending on the material and the photon energy, the change of photon current density dj_γ/j_γ in an interval dx and determines.

$$\alpha(\hbar\omega) = -\frac{dj_\gamma(\hbar\omega)/dx}{j_\gamma(\hbar\omega)} \tag{2.15}$$

It is proportional to the density of occupied states in the valence band and the density of unoccupied states in the conduction band since the absorption leads to the generation of an electron-hole pair. In direct transitions, only two particles are involved, whereas for indirect transition, the participation of a phonon is necessary to ensure the conservation of momentum. Such indirect transitions are most relevant in indirect semiconductors, where the valence band maximum and the conduction band minimum are shifted in momentum.

Figure 2.1 depicts the absorption coefficients for different absorber materials as a function of the photon energy. The probability for the absorption of a photon with $\hbar\omega < \mathrm{E_G}$ is zero and increases steeply for higher energies. For direct semiconductors such as GaAs, the edge is significantly steeper than for indirect semiconductor as silicon. For direct transitions the probability follows a square root dependency on the difference between bandgap energy and photon energy :

$$\alpha(\hbar\omega) \propto (\hbar\omega - E_G)^{1/2} \tag{2.16}$$

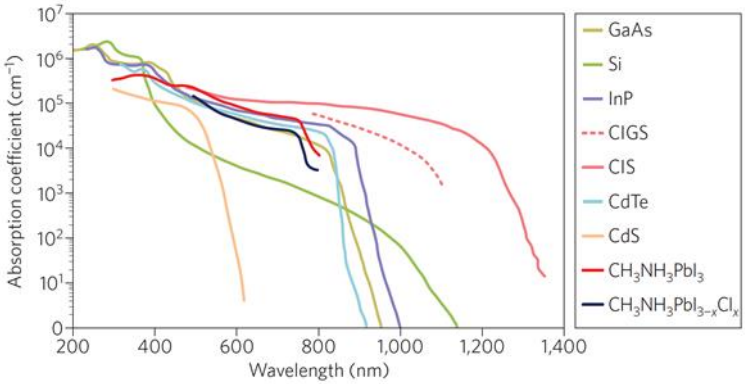

Figure 2.1 Absorption coefficient for common absorber materials in PV [62][1].

2.2.2 Recombination

The generation of electron hole pair is counterbalanced by their recombination. Here, the transition of an electron from an energy state in the conduction band to an unoccupied energy state in the valence band releases energy in form of photons, phonons or both. This process can also be regarded as the annihilation of an excited electron in the conduction band and an excited hole in the valence band. In thermal and chemical equilibrium (in the following denoted by a superscripted 0), the generation rate G and recombination rate R are equal. Following the equation of continuity, the change in the excess charge carrier density equals the difference between the rate for charge carrier generation and the rate for their recombination minus the diffusion:

$$\frac{d\Delta n(t)}{dt} = G - R - \nabla j \tag{2.17}$$

The charge carrier lifetime is the mean time between the generation and its annihilation via recombination with a charge carrier of the opposite species. As the most direct approach to define the charge carrier lifetime, it will be derived here for a simplified case, assuming a homogeneous system without diffusion and switched off

[1] Reprinted by permission from Springer Nature Customer Service Centre GmbH: Springer Nature, Nature Photonics, „*The Emergence of Perosvkite Solar Cells*“, M.A.Green, A. Ho-Baillie, H.J. Snaith, 2014

generation. In first order, it is $\Delta n \propto R$ and therefore the solution for the ordinary differential equation can be found:

$$\Delta n(t) = \Delta n_0 \exp(-\frac{t}{\tau}) \tag{2.18}$$

Where Δn_0 denotes the excess carrier density at a given time $\Delta \mathrm{n}(\mathrm{t}_0) =: \Delta n_0$ and τ is the characteristic lifetime. In the considered case, it is given by $\tau = \frac{\Delta \mathrm{n}}{R}$. As the linear correlation between recombination rate and excess carrier density is not given in most cases, the lifetime itself becomes a function of Δn. If multiple recombination channels are considered, the lifetime reads:

$$\tau(\Delta \mathrm{n}) = \frac{\Delta \mathrm{n}}{\sum_i R_i(\Delta \mathrm{n})} \tag{2.19}$$

2.2.2.1 Radiative Recombination

The reverse process to the generation of an electron-hole pair by absorbing a photon is the radiative recombination; it is the spontaneous transition of an electron from the conduction band to an unoccupied state in the valance band, emitting a photon with the energy $\hbar\omega$ corresponding to the transition (cf. Figure 2.2). The probability of this two-particle process R_γ depends linearly on the densities of electrons and holes, the proportionality factor is given by the coefficient of radiative recombination B_{rad}.

$$R_\gamma = B_{rad} n_e n_h \tag{2.20}$$

$$G_\gamma^0 = R_\gamma^0 = B_{rad} n_i^2 \tag{2.21}$$

For equilibrium state, the radiative recombination rate R_γ^0 equals the rate of the generation G_γ^0 and is proportional to the intrinsic concentration of electrons and holes ($n_e^0 n_h^0 = n_i^2$). This holds true also for small intervals of photon energy $d\hbar\omega$, as a consequence of Kirchhoff's law of radiation ($\alpha(\hbar\omega) = \epsilon(\hbar\omega)$). Known as the Principle of Detailed Balance, in thermal and chemical equilibrium, all individual generation processes are compensated by corresponding recombination processes at equal rates, both with the same initial and final conditions. Due to this equality, the black-body radiation at 300 K yields access to the radiative recombination coefficient B_{rad}, given that the wavelength dependent absorption coefficient $\alpha(\hbar\omega)$ and the intrinsic carrier concentration n_i are known, Ω denotes the solid angle.

$$B_{rad} n_i^2 = R_\gamma^0 = \frac{\Omega}{4\pi^3 \hbar^3 c^2} \int_0^\infty \frac{\alpha(\hbar\omega)(\hbar\omega)^2}{\exp\left(\frac{\hbar\omega}{kT_0}\right) - 1} d\hbar\omega \tag{2.22}$$

When additional charge carriers are generated by external illumination or charge carriers are extracted with an electric current, the electron and hole densities deviate from the equilibrium conditions and the relation of the intrinsic charge carrier density and the radiative recombination rate R_γ changes to:

$$n_e^0 n_h^0 = n_i^2 \neq n_e n_h \tag{2.23}$$

$$R_\gamma = R_\gamma^0 \frac{n_e n_h}{n_i^2} = R_\gamma^0 \exp\left(\frac{E_{FC} - E_{FV}}{kT}\right) \tag{2.24}$$

The proportional relation between rate and charge carrier density as well as the spectral distribution of the 300 K radiation remains unaffected. Taking into account the different Fermi distributions for electron an hole densities leads to the generalized Planck Radiation Law, as given in Equation (2.25). Tt describes the emission for $E_{FC} - E_{FV} = 0$ (thermal radiation) and $E_{FC} - E_{FV} \neq 0$ (photoluminescence radiation, cf. 3.1) and reveals the dependency of the radiative recombination rate on the Quasi-Fermi level splitting $E_{FC} - E_{FV}$.

$$dR_\gamma = \alpha(\hbar\omega) \frac{\Omega}{4\pi^3 \hbar^3 c^2} \frac{(\hbar\omega)^2}{exp\left(\frac{\hbar\omega - (E_{FC} - E_{FV})}{kT}\right) - 1} d(\hbar\omega) \tag{2.25}$$

2.2.2.2 Auger Recombination

Other recombination pathways for non-radiative recombination include the three-particle process Auger recombination. The energy, corresponding to the recombination of an electron from the conduction band with a hole from the valence band, is transferred to a third charge carrier. Depending on the species of this third particle, the Auger recombination rate is proportional either to $n_e^2 n_h$ or $n_e n_h^2$. If the energy is transferred to an electron in the conduction band, it is excited to a higher energy state within the band. Subsequently the excited electron relaxes back to the conduction band edge via thermalization. The analogous event happens if the energy is transferred to a hole at a low energy state within the valence band. An illustration of all recombination processes is given in Figure 2.2.

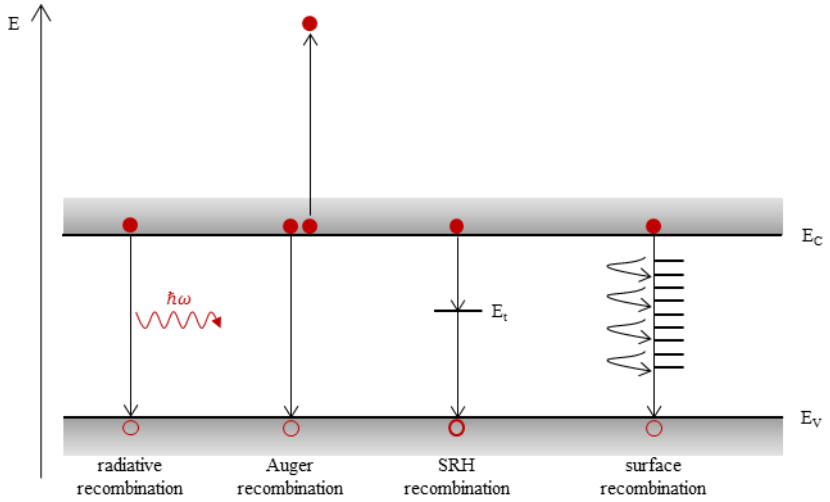

Figure 2.2 Recombination mechanisms in a schematic band diagram. From left to right, it shows radiative recombination, Auger recombination for the case of the third charge carrier being an electron, SRH recombination and surface recombination.

2.2.2.3 SRH-Recombination

Another non-radiative pathway is the recombination via energy levels within the bandgap. Comparable to doping atoms, impurities or defects in the crystal lattice can cause additional energy states in the band. However, depending on the position within the bandgap, these states causes recombination, which can constitute a major or even the most dominant recombination pathway.

These impurity states capture electrons from the conduction band and holes from the valence band, successively imparting the energy to the lattice. The principle is illustrated in Figure 2.2.

In 1951 and 1952, Shockley, Read and Hall introduced the theoretical description of the generation and recombination rate, this kind of recombination is commonly referred as Shockley-Read-Hall (SRH) recombination [63, 64]. In summary it is found that the rate is strongly dependent on the position of the energy state in the bandgap, the density of the concerning defect, its capture cross sections for electrons and holes and since both charge carrier species are involved, it is, as has been seen before, proportional to the product of electron and hole density.

$$R_{SRH} = \frac{n_e n_h - n_i^2}{\tau_{e0}(n_h + n_{h1}) + \tau_{h0}(n_e + n_{e1})} \tag{2.26}$$

In this equation, τ_{e0} and τ_{h0} denote the SRH lifetimes, which are functions of the defect density N_t, the capture cross sections for electrons/holes $\sigma_{e/h}$ and the thermal velocity v_{th}:

$$\tau_{e0} = \frac{1}{N_t \sigma_e v_{th}} \tag{2.27}$$

Further, n_{h1} and n_{e1} denote the SRH densities, analogous to the electron and hole carrier densities in Equation (2.11) and (2.12), that depend on the defect energy level E_t.

$$n_e = N_C exp\left(-\frac{E_C - E_t}{kT}\right) \tag{2.28}$$

$$n_h = N_V exp\left(-\frac{E_t - E_V}{kT}\right) \tag{2.29}$$

2.2.2.4 Surface Recombination

Recombination at surfaces poses a special case of SRH recombination. Interfaces present a large number of defects: unsaturated atomic bonds introduce multiple energy states within the bandgap and thus cause considerable recombination via these defect states as illustrated in Figure 2.2. The recombination via these numerous surface states is commonly summarized in the surface recombination velocity $S_{e/h}$. It is referred to as velocity due to its dimension. For electrons, it is the product of the surface states' capture cross section for electrons $\sigma_{s,e}$, the density of surface states per area occupied by a hole $n_{s,h}$ and the thermal velocity v_{th}:

$$S_e = n_{s,h} \sigma_e v_{th} \tag{2.30}$$

2.3 Single Junction Solar Cells

The basic working principle of a solar cell is based on the absorption of photons and the subsequent separation and extraction of the generated charge carriers to an external circuit.

In this section, the most relevant solar cell structure for this thesis, the heterojunction solar cell, is briefly introduced along with the fundamental current-

voltage characteristics and the parameters most commonly used to describe the quality of photovoltaic performance. For a more thorough discussion, the reader is referred to [61].

2.3.1 Heterojunction Solar Cells

Although conventional pn-junction solar cells are most common in PV, heterostructures are currently receiving much attention. While at a homojunction, the material of both sides of the pn-junction consists of the same material with different doping, a heterojunction is the interface between two different semiconductors. Silicon heterojunction (SHJ) solar cells deliver very high efficiencies and are frequently employed in high-efficiency tandem structures [15, 17, 65], also novel cell concepts such as perovskite solar cells (PSCs) base on heterojunction structures. This introduction is based on the theoretical description by Würfel [61] and Green [66].

In an ideal solar cell, there is no flow of electrons to the hole contact and no flow of holes to the electron contact to minimize surface recombination and charge current of the wrong polarity, reducing the cell's efficiency. By introducing charge carrier selective contacts consisting of materials with larger bandgaps and suitable electron affinities at either side of the absorber, the minority charge carrier density at the interface can be lowered, hence reducing the surface recombination. This approach is also useful, if a pn-junction cannot be induced in the absorber material because it can either not be doped at all or only towards p- or n-type. A basic heterojunction solar cell consists therefore of an absorber material, which is either intrinsic, p- or n-type, and two contact materials with different electron affinities χ_e and bandgaps. In Figure 2.3, the band diagrams for two different semiconductor materials prior to contact and in contact with each other are shown. Upon contact, the Fermi-level is constant across the interface, assuming thermal equilibrium. The discontinuity between the two conduction band edges at the junction equals the difference in the electron affinities $\Delta E_C = |\chi_e^1 - \chi_e^2|$, for the valence band edges, it is $\Delta E_V = |\chi_e^1 - \chi_e^2| + |E_G^1 - E_G^2|$. In the ideal case of no existing surface energy states at the interface, the electrical potential φ is continuous across the junction.

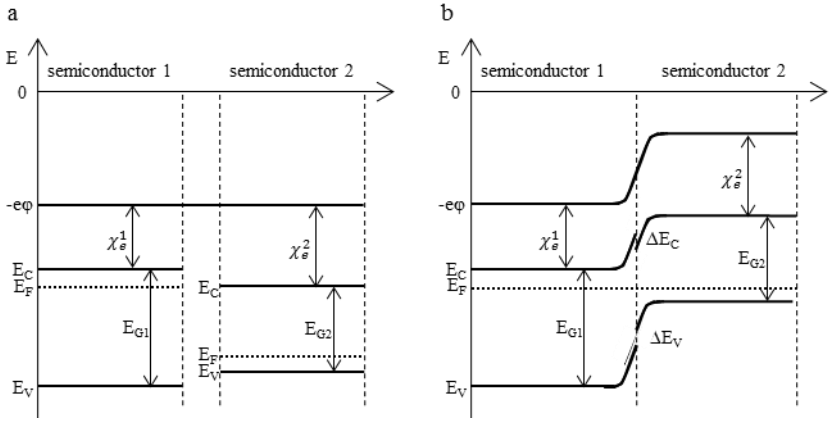

Figure 2.3 Two semiconductor materials with different electron affinities and bandgaps before (a) and after (b) contact.

2.3.2 Current-Voltage Characteristic of Solar Cells

A solar cell is a diode and commonly, two equivalent circuit models are used to describe the current-voltage characteristics of a solar cell [61, 66]. In a simplified view, a solar cell can be described as a system of one diode with a saturation current density J_0 in a circuit with a series resistance R_s and parallel resistance R_p and the photocurrent J_{illum}. The series resistance accounts for voltage drops at high current densities while the parallel resistance represents shunt contributions. Deviation from non-ideal diode behavior is accounted for by the so-called ideality factor n. In case of a theoretically ideal diode n should be unity. The current-voltage (J-V) characteristics in this model are given by the one-diode equation:

$$J(V) = J_0 exp\left(\frac{q(V - JR_s)}{nkT} - 1\right) + \frac{V - JR_s}{R_p} - J_{illum} \tag{2.31}$$

J_{illum} denotes the current density induced under illumination. The dark J-V characteristics follow from Equation (2.31) for $J_{illum} = 0$. The derivation of the single-diode equation neglects the recombination in the space charge region and consequently a constant value for the ideality factor n and a single dark saturation current J_0 are assumed. In a more accurate description, the recombination in the space charge region is taken into account, leading to two contributions with different voltage

dependencies. The total current can be derived considering two diodes connected in parallel, resulting in the two-diode equation for the current-voltage characteristics:

$$J(V) = J_{01} exp\left(\frac{q(V - JR_s)}{n_1 kT} - 1\right) + J_{02} exp\left(\frac{q(V - JR_s)}{n_2 kT} - 1\right) + \frac{V - JR_s}{R_p} - J_{illum} \tag{2.32}$$

The current is considered being generated by the two diodes with the dark current densities J_{01} and J_{02} connected in parallel. Both diodes are additionally described by two ideality factors n_1 and n_2. The theoretical values for ideal diodes are $n_1 = 1$ and $n_2 = 2$.

Equivalent to the one-diode equation, for $J_{illum} = 0$, the equation represents the diode characteristics in the dark. This model is used in the iterative fitting procedure in the local J-V analysis (cf. Section 3.3.2).

Although the direct interpretation of the two-diode model for perovskite solar cells but also silicon solar cells is still the topic of ongoing discussion, it is nevertheless well applicable to describe the current-voltage characteristics.

One major difference between the current-voltage characteristics of conventional solar cells and perovskite solar cells is an anomalous dependency on both the scan speed and scan direction observed for perovskites. This hysteresis behavior is due to ionic movement in the solar cell and will be discussed in Section 2.6.3.

In Figure 2.4, the current-voltage characteristics for a solar cell are depicted to illustrate the characteristic working conditions. The intersection of the J-V curve for the illuminated solar cell and the x-axis yields the cell voltage at open-circuit conditions (V_{oc}), the intersection with the y-axis gives the highest current density at short-circuit conditions (J_{sc}). A third characteristic point on the J-V curve is the point of maximum power (P_{MPP}) (cf. Figure 2.4). Here, the product of voltage and current density reaches its highest value. The ratio between the maximum power output P_{MPP} and the input power from illumination P_{in} gives the corresponding solar cell efficiency:

$$\eta = \frac{P_{MPP}}{P_{in}} = \frac{J_{MPP} V_{MPP}}{P_{in}} = \frac{J_{sc} V_{oc} FF}{P_{in}} \tag{2.33}$$

The fill factor FF in Equation (2.33) is the ratio between the product of short-circuit current and open-circuit voltage and the maximum power P_{MPP}:

$$FF = \frac{J_{MPP} V_{MPP}}{J_{sc} V_{oc}} \tag{2.34}$$

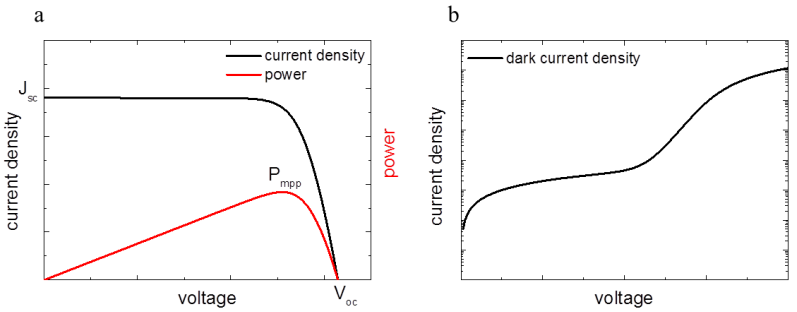

Figure 2.4 Current-voltage and power-voltage characteristics of a solar cell for illuminated conditions (a), and current-voltage characteristics for dark conditions (b) in linear / logarithmic scaling, respectively, illustrating most relevant operating conditions.

The current is determined by the absorption properties of the absorber material and extraction quality, while the voltage is mainly governed by the material's bandgap and recombination losses.

2.4 Multi-Junction Solar Cells

Certain high-efficiency concepts are based on solar cells incorporating more than one absorber material within a single device. These multi-junction (MJ) solar cell can surpass the efficiency limit for a single-junction solar cell and hence received a lot of attention in recent years. This efficiency limit as well as the different ways to electrically connect multi-junction solar cells with its benefits and drawbacks, are introduced in this section.

2.4.1 Shockley-Queisser-Limit

Intrinsic losses such as thermalization losses for high-energy photons and non-absorption of photons with sub-bandgap energies limit the efficiency of single solar junction solar cells. Given a black-body solar spectrum (temperature of the sun $T_S = 5800\,K$) and assuming ideal absorption a (cf. Equation (2.35)) for a solar cell

with bandgap E_G, its short-circuit current J_{sc} is given by Equation (2.36), where Ω denotes the solid angle.

$$a = \begin{cases} 0, & \hbar\omega < E_G \\ 1, & \hbar\omega \geq E_G \end{cases} \tag{2.35}$$

$$J_{sc} = -e\frac{\Omega}{4\pi^3\hbar^3c^2}\int_{E_G}^{\infty}\frac{(\hbar\omega)^2}{\exp\left(\frac{\hbar\omega}{kT_S}\right)-1}d\hbar\omega \tag{2.36}$$

Considered as a function of the bandgap energy, the conversion efficiency attains a maximum between the influences of thermalization non-absorbable photons, if the entire energy of electron-hole pairs could be converted into electrical energy. The theoretical limit of 30% for a single-junction cell with a bandgap of 1.1 eV was originally derived by Shockley and Queisser in 1961 [67]. Since part of the electron-hole pairs' energy is room temperature heat due to entropy conservation, this limit cannot be reached above absolute zero.

.

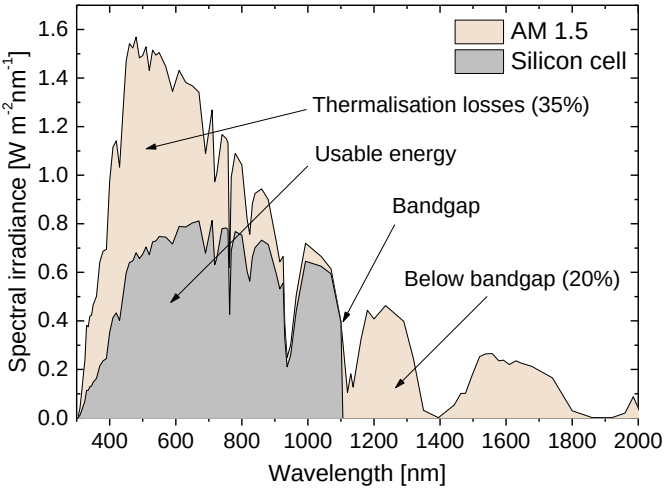

Figure 2.5 Comparison between AM 1.5 solar spectrum and usable energy for a silicon single junction solar cell, revealing significant thermalization and sub-bandgap losses.

In the case of silicon, the theoretical efficiency limit is 29.6 % [68], which is below the Shockley-Queisser-Limit due to non-negligible intrinsic Auger recombination. In Figure 2.5, the spectrally resolved losses for a silicon solar cell are illustrated

In the effort to increase the conversion efficiency beyond this limit, multi-junction (MJ) solar cells are an eligible solution. The combination of several absorber materials of descending bandgap allows for the reduction of thermalization losses as well as sub-bandgap losses by utilization of low energy photons in the low bandgap absorber (cf. Figure 2.6 a,b). In its most simple approach, a tandem device combines two absorber materials featuring one high and one low bandgap (E_{G_1} and E_{G_2}, respectively). Assuming AM1.5g solar spectrum and exclusive radiative recombination, the optimal match of bandgap energies is $\mathrm{E_{G_1}} = 1.9$ eV and $\mathrm{E_{G_2}} = 1.0$ eV, yielding a theoretical efficiency of 42.2% [69].

Generally, two different configurations for tandem solar cells can be distinguished, each holding its individual benefits:

2.4.2 2-Terminal Tandem

In this architecture, the two subcells are monolithically integrated. The subcells are connected in series; i.e. the total voltage equals the sum of the subcells' voltages. Hence, it is crucial that both voltages must have the same sign, meaning that both cells must have the same pole facing the sun. Either a tunnel junction or a recombination layer constitutes the electrical connection between top and rear cell, ensuring efficient recombination of the charge carriers at the cell interface without requiring a difference in their Fermi levels. The overall current equals the lowest current of the single subcells, requiring a balance of the subcells' bandgaps and thicknesses in order to achieve current matching. The direct deposition on top of the rear cell might also create some restraints with regard to processing techniques (e.g. temperature) in order not to affect the rear cell negatively. Direct depositing the top cell on the bottom cell is the most common approach of processing monolithic two-terminal devices, yet other process routes such as wafer-bonding are also eligible options [70].

One major advantage, with regard to the photocurrent, is the comparably low parasitic absorption in the interconnection layer (tunnel junction or recombination layer) and the transparent top electrode in contrast to three transparent contacts in the four-terminal configuration (cf. Figure 2.6 c,d). Another benefit as a consequence of the high resulting voltage is the reduction of resistive losses in PV systems. The reduced number of processing steps makes this approach also more feasible to integrate it into an existing manufacturing process.

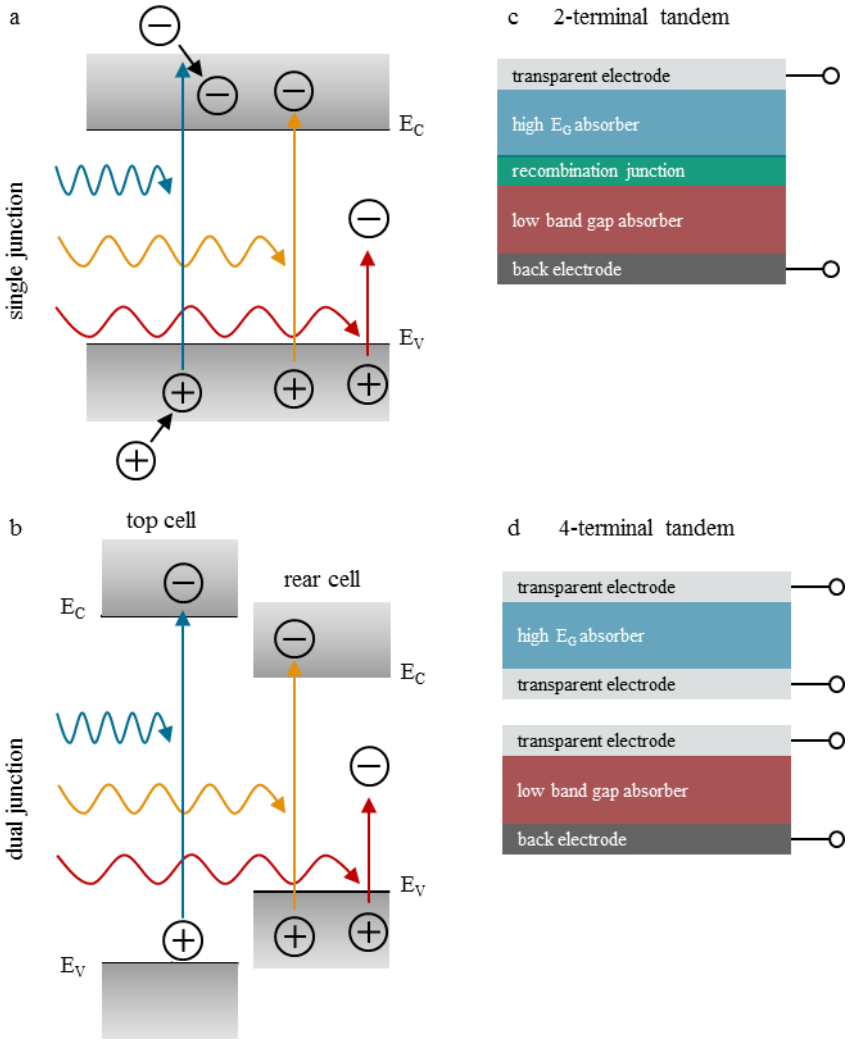

Figure 2.6 Illustration of the working principle of a tandem solar cell: wavelength-dependent excitation in a single junction (a) and reduced thermalization losses in a dual junction (b). Schematic structure of a 2-terminal tandem solar cell (c) in comparison to a 4-terminal tandem solar cell (d).

2.4.3 4-Terminal Tandem

This configuration is realized by mechanical stacking of two subcells, each including its individual electron and hole contact. The cells can then be contacted separately. This obviously lifts the processing restraints and does not require current matching. During operation, the cells are kept at their individual maximum power points, making them less sensitive to spectral variations. This leads to very high efficiencies with lower restraints towards the bandgap selection.

Yet, the structure requires two additional transparent contacts, which increases the parasitic absorption and lowers the generated photocurrent in the rear cell. From an application's point of view, this approach is less favorable, for it requires all power electronics for both subcells, contributing significantly to the overall costs.

2.5 Perovskites

As the main object of investigation in this thesis, an overview of the historical development of perovskite materials as absorber for photovoltaic application is given in this section. Concerning the perovskite material, also the crystal structure, the bandgap tunability and common deposition techniques are introduced.

2.5.1 Brief History

As perovskites, we denote any material assuming the same crystal structure as the mineral $CaTiO_3$. It was originally discovered by the German mineralogist Gustav Rose in the Ural Mountains in 1839 and named in compliment to the Russian nobleman and mineralogist Count Lev Alekseyevich von Perovski. The perovskite structure generally assumes the chemical formula ABX_3 where A and B are cations of different sizes, A being larger than B, and X is an anion.

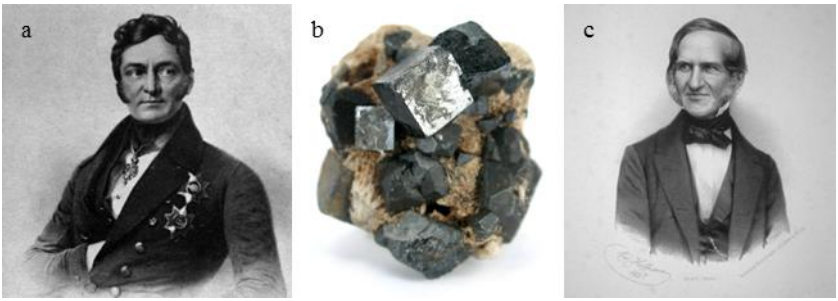

Figure 2.7 Name giver Count Lev Alekseyevich von Perovski (a) [71], calcium titanium oxide mineral composed of calcium titanate ($CaTiO_3$) (b) [72], discoverer of the original mineral and German mineralogist Gustav Rose (c) [73].

The first application of perovskites as photovoltaic absorber material was published in 2009 by Miyasaka et al. [74]. His group employed an organic inorganic halide perovskite as sensitizer in a dye-sensitized solar cell and thereby achieved low single-digit conversion efficiencies. Over the next three years, two collaborations transferred the liquid-containing to a solid-state device and reported efficiencies around 10% in 2012 [75, 76]. Since then, cell efficiencies have skyrocketed to 22.7% in 2017 [3].

2.5.2 Crystal Structure

The generic formula unit is ABX_3, the cubic crystal structure is depicted in Figure 2.8. Most commonly used is methyl ammonium (CH_3NH_3, MA) lead triiodide with MA being the organic cation A, Pb the metal component B and iodide the halide X. The section about the perovskite crystal structure follows the monograph by Park et al. [77].

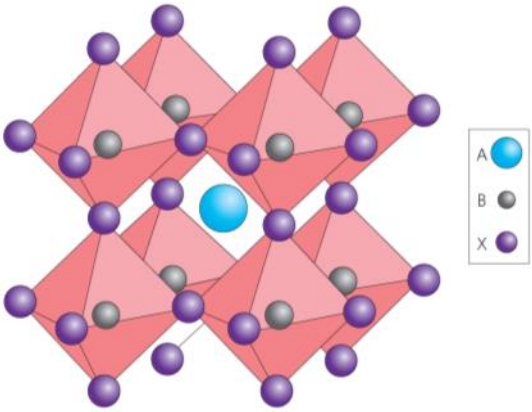

Figure 2.8 Cubic perovskite crystal structure. BX_6 octahedra surround the larger cation in the middle. The lattice constant of the unit cell is given by the distance between two B sites [62][2].

At room temperature, iodide perovskite is tetragonal, with a phase transition to the cubic phase at 327 K. The tetragonal lattice can be described as $\sqrt{2}a \times \sqrt{2}a \times a$ expansion of the cubic unit cell. At lower temperatures (< 165 K), the perovskite adopts an orthorhombic structure. Comparable to the tetragonal phase, the lattice is a $\sqrt{2}a \times \sqrt{2}a \times a$ expansion of the cubic unit cell but with additional distortion in the PbI_6 octahedra. Crucial for the determination which structure a perovskite will adopt, is the Goldschmidt tolerance factor t_G [78–80], taking into account the ratio of the ionic radii:

[2] Reprinted by permission from Springer Nature Customer Service Centre GmbH: Springer Nature, Nature Photonics, „*The Emergence of Perosvkite Solar Cells*“, M.A.Green, A. Ho-Baillie, H.J. Snaith, 2014

$$t_G = \frac{r_A + r_0}{\sqrt{2}(r_B + r_0)} \tag{2.37}$$

The Goldschmidt tolerance factor is a reliable empirical index to predict the stability of perovskite structures. General perovskite materials assume ideal cubic structures for a tolerance factor of $0.9 < t_G < 1$, deviations from this value result in geometric strain and crystal distortions leading to lower symmetry, values in the range of $0.71 < t_G < 9$ result in structures with tilted octahedra. For inorganic-organic halide perovskites, they assume the desired cubic phase for $0.8 < t_G < 1$. The chemical composition is generally not deterministic for the crystal structure. More than one can be adopted, depending on the temperature and the preparation method. In case there is a photoactive (black phase), it will be denoted as α–phase while the non-photoactive state will be denoted as δ–phase (yellow phase), this phase will presumably yield a tolerance factor $t_G \ll 1$ or $t_G \gg 1$

Alterations in the crystal lattice such as octahedral tilting or isotropic contraction/expansion influence the bandgap of the material. Tight binding modelling and first principle electronic structure calculations showed that the bandgap variation as a function of the lattice strain is predominantly related to the antibonding combination of metal s- and halide p-orbitals, which comprises the valence band maximum [81–85]. Its energy rises under compressive strain to the lattice that increases the metal-halide overlap and thereby destabilizes the valence band. Decrease in the overlap, e.g. by distortion in the metal-halide bond, lowers the valence band maximum accordingly.

2.5.3 Bandgap Tunabiliy

This paragraph follows in its main contents the reviews by Correa-Baena, Abate and Saliba et al. from 2017 [86] and is complemented by the article of Li et al. [80].

The majority of investigations of perovskites for PV application focuses on $MAPbI_3$. Yet, a seemingly endless number or of elements and molecules can be arranged in perovskite structure, yielding results worthy of detailed examination. Despite the variety of compounds, the most eligible alloys are comprised of a limited number of components. These most common ingredients are summarized in Table 2.1. Chemical engineering is a key instrument in influencing material properties and has been employed to increase the intrinsic stability and tune the bandgap.

Table 2.1 Summary of most common components in perovskite absorbers.

A	B	X
MA	Pb	I
FA	Sn	Br
Cs		Cl
Rb		

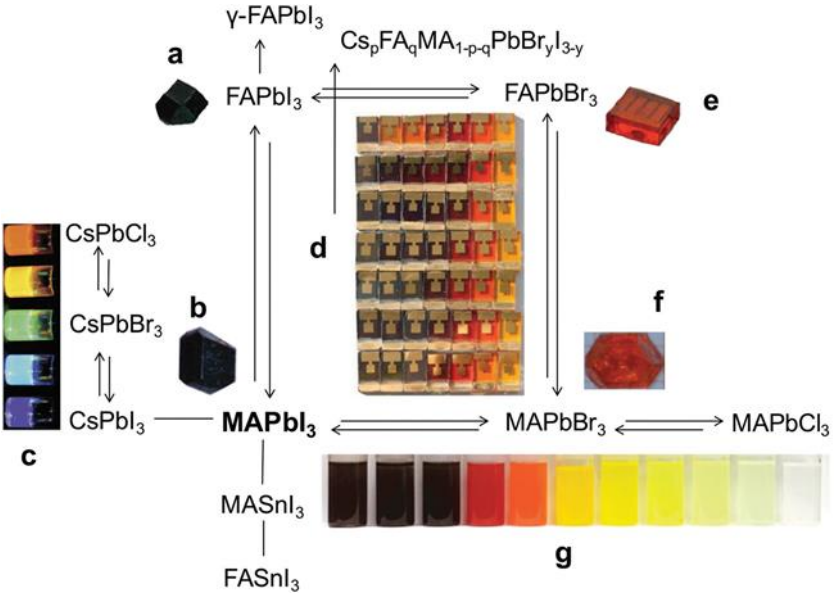

Figure 2.9 Overview of the correlation between perovskite composition and the tunable bandgap: photographs of $FAPbI_3$ (a) and $MAPbI_3$ (b) single crystal. Colloidal solutions of $CsPb(Cl/Br/I)_3$ perovskites (c), solar cells made of a compositional spread-sheet (d). Single crystals of $FAPbBr_3$ (e) and $MAPbBr_3$ (f). Colloidal nanocrystals of $MAPb(Cl/Br/I)_3$ perovskites [86][3].

[3] Reprinted by permission from RSC Publishing: Royal Society of Chemistry, Energy & Environmental Science, „*The Rapid Evolution of Highly Efficient Perovskite Solar Cells*“, J.P. Correa-Baena, A. Abate, M. Saliba, W. Tress, T.J. Jacobsson, M. Grätzel, A. Hagfeldt, 2017

Substitution and alloying enables an exceptional continuous tunability of the perovskite's bandgap in the range of 1.2 eV to 3.1 eV. By introducing smaller halide ions such as chlorine and bromine in the crystal lattice instead of iodine, the bandgap increases. Reported values for polycrystalline films of $MAPbI_3$ are around 1.6 eV, for $MAPbBr_3$ and $MAPbCl_3$, bandgaps are as high as 2.3 eV and 3.1 eV, respectively.

Mixed halide compositions allow to continuously tune the bandgap over a wide range. Yet, for $MAPb(Br_xI_{1-x})_3$, severe light-induced phase segregation was observed by Hoke et al. [41], the mechanism was thus named "Hoke effect".

Furthermore, the A site cation can be exchanged for a single component listed in Table 2.1, or then a mixture of multiple components. Changing to the slightly larger formamidinium ion $(CH(NH_2)_2^+$, FA) has less effect on the bandgap than the stability. The slight change of the bandgap from 1.6 eV for $MAPbI_3$ to ~1.45 -1.52 eV for $FAPbI_3$ is due to a small lattice expansion together with a tilt of the PbI_6-octahedra. The Goldschmidt tolerance factor increases for the α–phase of this composition including the larger ion, however, solution processed films also showed the existence of a non-photoactive δ–phase for $FPbI_3$ (cf. Section 2.5.2). The α–$FAPbI_3$ phase displays an increased resistivity against degradation upon exposure to moisture. Increased thermal stability was achieved by introducing the inorganic cation Cs^+ to the composition. Though the small cation results in a tolerance factor < 0.8 and the cubic α–$CsPbI_3$ phase is obtained only for high temperatures (> 600 K), alloys including the solid state cation yield optimized tolerance factor and generally suppress ion segregation for the case of mixed halides. The approach of the triple cation perovskites Cs/MA/FA also improved the crystal quality. For the additional incorporation of the Cs^+ and the even smaller Rb^+ cation, the influence on the bandgap is negligible, but beneficial influence on trap density in the case of Cs^+ and charge carrier mobility for Rb^+ has been observed [87].

Lastly, B site alloying enables access to low bandgap perovskites: $MA(Sn_xPb_{1-x})I_3$ alloys show tunable bandgaps down to 1.17 eV, the reduction of the bandgap being due to a lattice contraction. Interestingly, an anomalous behavior of the bandgap occurs for tin/lead alloys: the lowest bandgap is not found for pure tin perovskites but an intermediate composition. Via the combination of A- and B-site alloying, a wide range of low bandgap perovskites with reasonable to high efficiencies has been achieved successfully [11].

The vast variety of applicable materials enables a multi-dimensional alloying matrix for which the ideal compositions with regard to bandgap, efficiency and stability are yet to be determined.

2.5.4 Perovskite Film Fabrication

Besides the wide range of applicable materials, there are also multiple techniques in the fabrication of perovskite thin films. An introduction to the most common methods will be given based on the review paper of Correa-Baena et al. from 2017 [86]. Schematic display of the different approaches is given in Figure 2.10.

2.5.4.1 One-Step Deposition

The metal halide and the organic halide precursor salts are both dissolved in an polar solvent, e.g. N,N-dimethylformamide (DMF), dimethylsulfoxide (DMSO) or mixtures of those, and spin coated onto a substrate. Perovskite formation is induced through an annealing step. Alternatively, the deposition is realized via dual-source co-evaporation of the metal halide and organic halide salt, again followed by an annealing step. An advancement of the one-step process is the anti-solvent method: an anti-solvent such as chlorobenzene or toluene, is dropped onto the substrate during the spin coating of the perovskite precursor solution. This technique yields the highest efficiencies to date, however the results strongly vary with the timing and exact deposition of the anti-solvent and hence crucially depend on the manual dexterity.

2.5.4.2 Two-Step Deposition

The sequential deposition of the two precursor solutions allows for additional control over the perovskite crystal morphology. Firstly, the metal halide is deposited via spin coating the precursor solution or evaporated onto the substrate. Subsequently, the film is exposed to the organic ion either in solution or in vapor. The perovskite crystal formation commences immediately, intercalating the organic ions between the layers of the metal-halide octahedra. One sub-category in the two-deposition approach is the hybrid route: a combination of evaporated metal halide layer and subsequent wet-chemical deposition of the organic halide precursor.

In order to create well-working photovoltaic devices, a homogeneous perovskite layer with high crystal quality is essential. Influences of grain boundaries and defect chemistry (e.g. excess or deficiency of the metal halide salt) are the topic of ongoing investigations. Numerous post-deposition treatments are employed to increase the perovskite film quality: solvent annealing for grain growth or improvement of the film

homogeneity, chemical treatments are generally employed to induce Oswald ripening or for surface and trap passivation [88, 89].

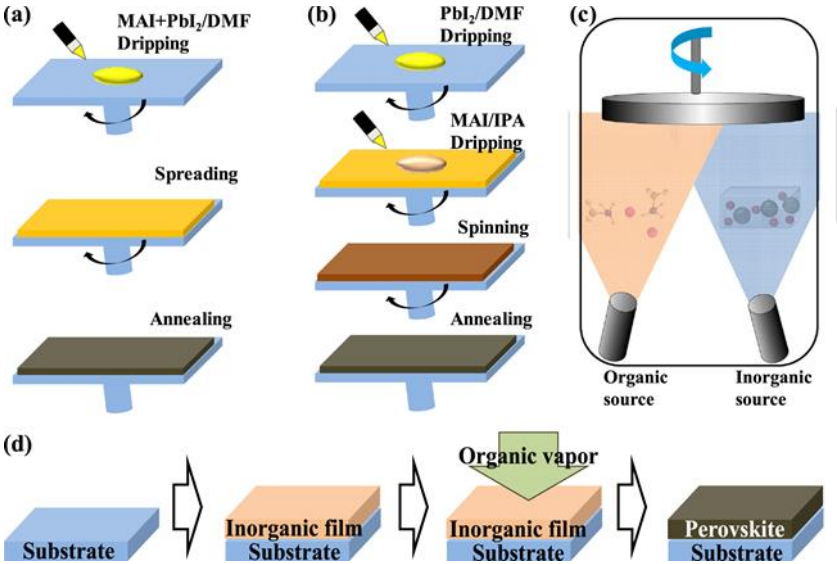

Figure 2.10 Schematic representation of the different deposition techniques: wet-chemical deposition for the one-step (a) and two-step (b) process. Co-evaporation of metal halide and organic cation (c) and the two-step evaporation process (d) [90][4].

2.6 Optoelectronic Properties

As the general theoretical basics of absorption and charge carrier dynamics in semiconductors have been discussed in Section 2.2, this section is about the specific characteristics of perovskite materials. Additionally, ionic movements, their effect on the optoelectronic properties and their correlation to anomalous hysteresis behavior in current-voltage characteristics are introduced.

[4] Reprinted with permission according to the Creative Commons Attribution 3.0 license.

2.6.1 Absorption Coefficient

One of the first remarkable properties of perovskite materials (initially, $MAPbI_3$) was the high absorption coefficient whose wavelength dependency features a very steep onset [62]. This particularly steep onset is comparable to characteristics found for established, monocrystalline materials of high electrical quality and a direct bandgap such as GaAs (cf. Figure 2.11). For energies below the band edge, the absorption coefficient decreases exponentially, the slope of this part of the curve indicates absorption tail states and is known as Urbach energy. $MAPbI_3$ features an Urbach energy as low as 15 meV, which suggest very low density of sub-bandgap energy states near to the band edge and highly ordered microstructures [91, 92]. All three phases of $MAPbI_3$, cubic, orthorhombic and tetragonal, are considered semiconductors with a direct bandgap [93–95]. However, Rashba-splitting of the conduction band as a consequence of spin-orbit coupling causes a weakly indirect bandgap close to the direct transition [96, 97]. This indirect bandgap is also conjectured to be responsible for long charge carrier lifetimes [98].

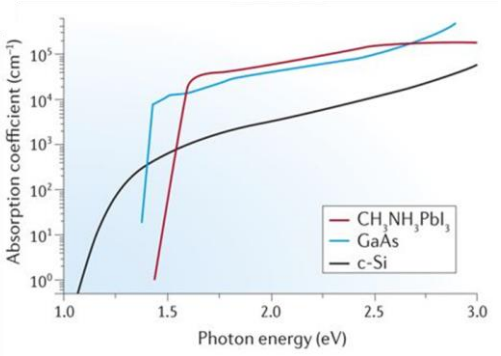

Figure 2.11 Absorption coefficient as a function of the photon energy for $MAPbI_3$ in comparison to established photovoltaic materials GaAs and crystalline silicon (c-Si). $MAPbI_3$ features an absorption edge comparable to GaAs [99][5].

[5] Reprinted by permission from Springer Nature Customer Service Centre GmbH: Springer Nature, Nature Reviews Materials, „*Hybrid organic—inorganic perovskites: low-cost semiconductors with intriguing charge-transport properties*“, T. Brenner, D.A. Egger, L. Kronik, G. Hodes, D. Cahen, 2015

Compared to the silicon, as an indirect semiconductor, the absorption coefficient is several orders of magnitude higher, which enables much lower film thickness. While a typical silicon cell has an absorber layer of $150 - 200\,\mu m$, a high-efficiency perovskite solar cell requires few hundred nanometers to absorb incident light sufficiently.

2.6.2 Charge Carriers

While excitons do not play a significant role in inorganic semiconductors, they are the predominant charge carrier in organic semiconductors. Exciton binding energies range from few meV in inorganic [100, 101] to $100 - 1000\,meV$ in organic semiconductors [102]. The binding energy measures the energy required to dissociate excitons into free electrons and holes that can be collected. Based on their organic-inorganic nature, the nature of the charge carriers in PSCs was thoroughly investigated. Values for the exciton binding energy for $MAPbI_3$ were found to be between $2\,meV$ and $75\,meV$ [103–110] and assuming solar cell working conditions, the predominant species is free charge carriers [111].

2.6.2.1 Charge Transport

Essential for every solar cell is that charge carriers reach the respective extraction layer before they recombine. Hence, the diffusion length, the distance a charge carrier travels before recombining with a charge carrier of the opposite species, needs to be longer than the distance to the contacts. Especially DSSCs have very short diffusion lengths, which evoked the development of mesoporous structures in order to reduce the distance to the extraction layer. However, studies of the diffusion length in perovskite materials have revealed unexpectedly large values up to several micrometers for mixed halide compositions and single crystals [112–117]. With an average absorber film thickness of few hundred nanometers, this is more than sufficient to work efficiently as a thin film solar cell [112, 113, 118–123].

Charge carrier mobilities have been reported ranging from $1 - 100\,cm^2/Vs$ for the most typical perovskite compositions (overview can be found in [124]).

2.6.2.2 Charge Carrier Recombination

General recombination kinetics are discussed in Section 2.2. For halide perovskite materials, the predominant recombination mechanisms are surface recombination at the interfaces to the contacts, SRH recombination via defect energy levels in the bandgap and radiative recombination as they are direct semiconductors. It has been

found that Auger recombination plays a minor role in the charge carrier dynamics of perovskites at normal operating conditions (charge carrier densities of $10^{15} - 10^{16}$ cm^{-3}). For the application both in photovoltaic devices and in light emitting diodes, having radiative recombination as the sole recombination channel is desirable and one of the most important material quality attributes. Typical values reported for $MAPbI_3$ are in the range of $10^{-11} - 10^{-9}$ cm^{3}s^{-1} [110, 114, 125–130]. Nevertheless, recombination via trap states is dominating the charge carrier dynamics in most perovskite materials, with recombination rates ranging between $10^{-7} - 10^{-5}$ s^{-1} [110, 114, 126–128, 131]. The lower end of that range corresponds to charge carrier lifetimes as high as tens of microseconds for $MAPbI_3$ single crystals. Single crystals naturally exhibit lower defect densities but also chemical passivation layers can suppress the non-radiative recombination [117, 117, 132, 133].

The injection dependency, that is dependency of the charge carrier density, of the total recombination rate for $MAPbI_3$ is shown in Figure 2.12. As the individual recombination mechanisms exhibit different injection dependencies, they govern different ranges of charge carrier densities as indicated by the differently colorized symbols.

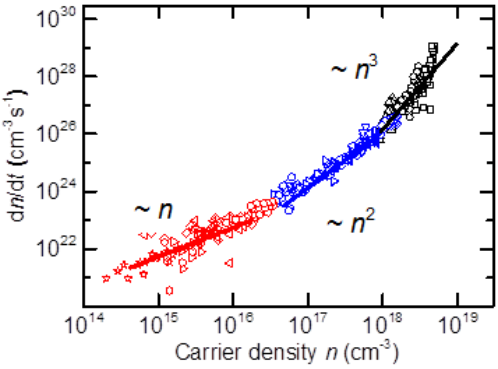

Figure 2.12 Recombination rate of $MAPbI_3$ as a function of the charge carrier density[134][6].

[6] Reprinted with permission according to the Creative Commons Attribution 4.0 license.

2.6.3 Ion Migration

Several peculiar phenomena exhibited by halide perovskite materials and solar cells are related to the migration of ions in the material:

- Anomalous hysteresis: the deviation of measurable current when scanning the current-voltage characteristics from short-circuit conditions to open-circuit conditions in comparison to the reverse scan direction, along with the dependency on the scan-speed [34, 36, 135–137] (Figure 2.13).
- Anomalous photovoltaic effect: open-circuit voltages exceeding the bandgap of the halide perovskite [138]. The highest observed values were multiple times higher than the corresponding bandgap.
- Light-induced halide segregation in mixed halide perovskites [41] (cf. Figure 2.14), reduction of the trap density [48] and expansion of the crystal lattice [81].
- Self-healing: increase in cell performance either under illumination [139] or in the dark [140] (cf. Figure 2.15).

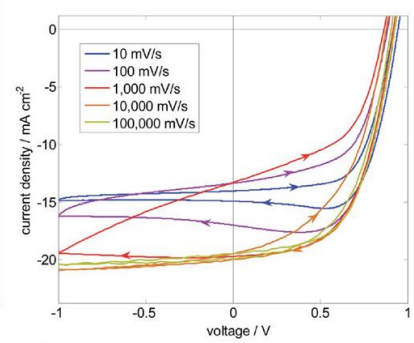

Figure 2.13 Current-voltage characteristics of a PSC for different scan directions and rates, showing pronounced hysteresis [135][7].

[7] Reprinted by permission from RSC Publishing: Royal Society of Chemistry, Energy & Environmental Science, „*Understanding the Rate-Dependent J–V Hysteresis, Slow Time Component, and Aging in $CH_3NH_3PbI_3$ Perovskite Solar Cells: The Role of a Compensated Electric Field*“, W. Tress, N. Marinova, S.M. Zakeeruddin, M.K. Nazeeruddin, M. Grätzel, 2015

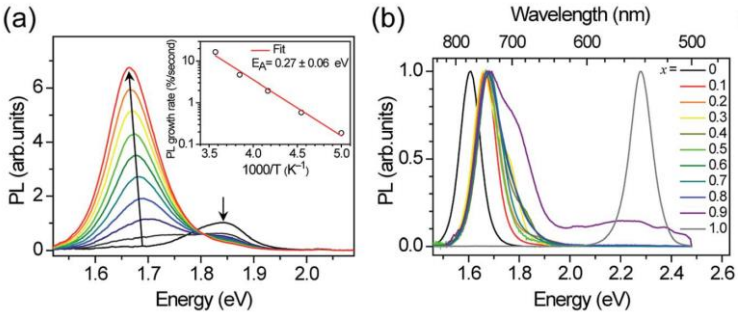

Figure 2.14 Demonstration of photo-induced shifts in the PL spectra of $MAPb(Br_xI_{1-x})_3$ mixed halide perovskite under monochromatic illumination: time evolution for a x=0.4 thin film (a), normalized PL spectra for a variation of the Br/I ratio after illumination (b) [41][8].

The diffusion of ions through a crystal can occur via lattice defects such as interstitials or vacancies, an overview over possible mechanisms is given in Figure 2.16. Both the density of lattice defects (which in turn is influenced by multiple factors such as processing conditions) and the corresponding activation energy determine diffusion rates for the various mechanisms. Additionally, charged ions can be gathered by extended defects such as grain boundaries, interfaces and dislocations [141].

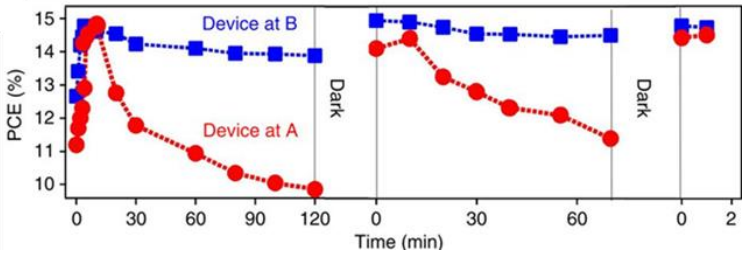

Figure 2.15 Example for self-healing of PSCs in the dark: Efficiency over time at open-circuit conditions (A) or short-circuit conditions (B) under constant $1000\ W/m^2$, AM1.5g equivalent illumination, interrupted by periods in the dark [140][9].

[8] Reprinted with permission according to the Creative Commons Attribution 3.0 license.
[9] Reprinted with permission according to the Creative Commons Attribution 4.0 license.

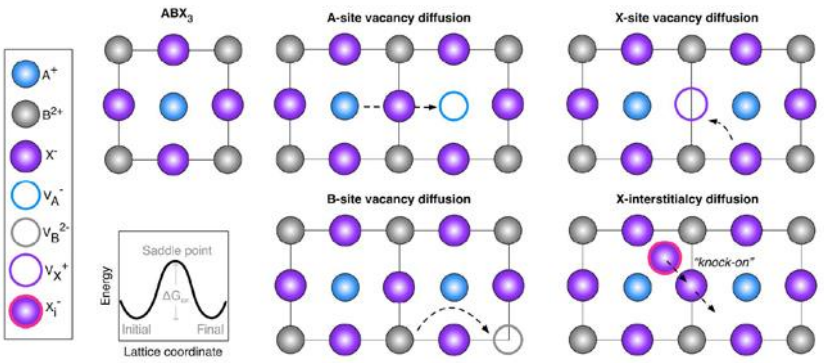

Figure 2.16 Illustration of possible lattice defect-based diffusion mechanisms in ABX_3 crystal structures [141][10].

In iodine perovskites, vacancy-mediated diffusion of iodine appears to be the major diffusion mechanism [41, 48, 142–144]. Yet, there is experimental evidence that all components in a perovskite structure are potentially mobile [145, 146].

Solar cell operation or characterization pose extrinsic influences and can influence the ionic movement in the material. Ion migration due to an electric field is the main cause of the commonly observed hysteresis. Charged ions accumulate at the interfaces of the absorber layer and the contacts, effectively screening the applied field. Consequently, the potential is slowly decreased and thereby causes the hysteresis [135].

Upon illumination, ions migrate away from the illuminated area both in pure $MAPbI_3$ crystals and mixed compositions [41, 48, 142, 147–149]. While there are multiple possible effects including electrical and thermal changes, direct photochemistry (conversion of methyl ammonium to methylamine) and the access of metastable charge states of defects, the exact microscopic description is yet to develop [141].

[10] Reprinted with permission from ACS Energy Letters, "*Taking Control of Ion Transport in Halide Perovskite Solar Cells*",A. Walsh, S. Stranks, Copyright 2018 American Chemical Society

2.7 Perovksite Solar Cells

Turning towards complete devices, the basic heterostructure always comprises a perovskite absorber layer sandwiched between selective contacts. The selectivity is achieved via offsets in the conduction and valance band, respectively. A second major criterion is the recombination at the perovskite/contact interface. In order to avoid voltage loss, minimizing this surface recombination is essential.

Again adding to the general variety, several architectures can be distinguished (cf. Figure 2.17) and numerous candidates for both electron and hole transport layer (ETL and HTL [150], respectively) are available. In the following, three cell architectures, which all yield the potential of conversion efficiencies above 20 % [151], and, in this context, the most commonly deployed contact layers for the individual architectures, are introduced (cf. [86]):

2.7.1 Mesoporous n-i-p

Initially, perovskites were used as sensitizer in dye-sensitized solar cells (DSSCs), hence their early development was based on a layer stack comprising a mesoporous scaffold comparable to those in DSSCs of few micrometers thickness. High efficiencies were achieved with a thinner scaffold of approximately 200 nm, which is composed of either TiO_2 or Al_2O_3. Together with an underlying compact layer of TiO_2, this assembles the electron contact and is in the n-i-p configuration turned towards the incident light (cf. Figure 2.17 a). Illumination occurs through a glass substrate coated with a transparent conductive oxide (TCO). Most common is fluorine doped tin oxide (FTO) or indium tin oxide (ITO). On the opposite side of the perovskite infiltrated mesoporous scaffold, a layer of 2,2',7,7'-Tetrakis[N,N-di(4-methoxyphenyl)amino]-9,9'-spirobifluorene (spiro-OMeTAD) covered with a gold electrode constitutes the HTL [152].

2.7.2 Planar n-i-p

The planar configuration was developed from the background of organic photovoltaics, exploiting that the perovskite layer acts both as absorber and charge transporter. Excluding the mesoporous scaffold, it features the same layers as the mesoporous n-i-p architecture (cf. Figure 2.17 b) [118]. For high-efficiency cells, a layer of SnO_2 on FTO forms the electron contact while the hole selective contact is identical to the mesoporous n-i-p structure.

2.7.3 Planar inverted p-i-n

Aiming for low-temperature processes to enable compatibility with flexible polymer substrates, an inverted p-i-n planar cell architecture was developed. In this structure, the position of ETL and HTL are transposed [153] (cf. Figure 2.17 c) and vary from

the materials applied in regular n-i-p structures. One possibility is a combination of fullerene-C60 and 2,9-Dimethyl-4,7-diphenyl-1,10-phenanthroline (BCP) as ETL together with copper as metal electrode. The HTL can be comprised of Poly[bis(4-phenyl)(2,4,6-trimethylphenyl)amine] (PTAA) on top of the ITO covered glass substrate.

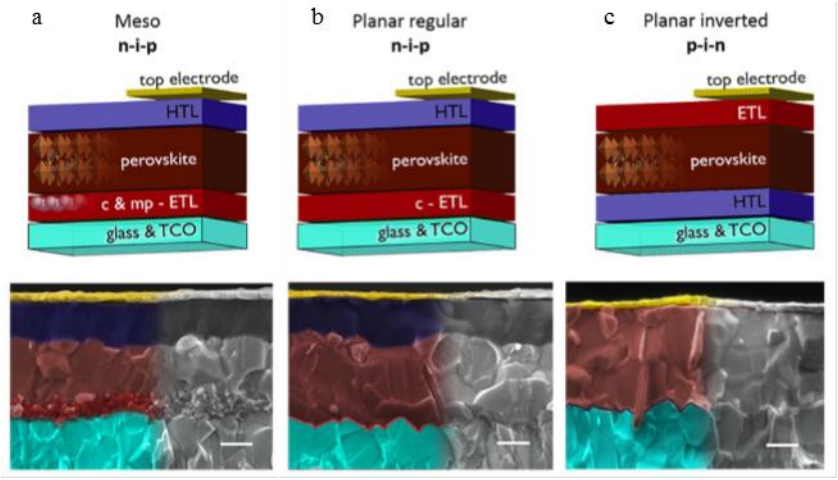

Figure 2.17 Schematic cell architectures for perovskite solar cells in the n-i-p structure with mesoporous scaffold (a), in a planar structure (b) and a planar inverted p-i-n structure (c). The cells are illuminated from the glass/TCO side[151][11].

2.7.4 Silicon Perovskite Tandem

For the low bandgap absorber, silicon is particularly well suited with a bandgap of 1.1 eV. Therefore, the optimal bandgap for a top cell is 1.7 eV – 1.8 eV for 2-terminal (2T) tandem and 1.6 eV – 2.0 eV for 4-terminal (4T) tandem configuration. The narrow range for the 2T is a consequence of the current matching imperative. In this challenge, the tunability of the perovskite's bandgap is a key advantage. Hence, differently balanced alloys of mixed cation and mixed halide perovskite composition are employed in recent high-efficiency tandem solar cells. The theoretical efficiency limit,

[11] Reprinted with permission from Chemistry of Materials, "*How to Make over 20% Efficient Perovskite Solar Cells in Regular (n–i–p) and Inverted (p–i–n) Architectures*", M. Saliba, J.P. Correa-Baena, C.M. Wolff, M. Stolterfoht, N. Phung, S. Albrecht, D. Neher, A. Abate, Copyright 2018 American Chemical Society

for both 2T and 4T cell design, is 43% [154–156]. A detailed discussion of the development of silicon perovskite tandem solar cells is given in the review by Werner et al. from 2017 [157]. Being more relevant within the scope of this work, the state of the art for monolithically integrated 2T solar cells are introduced here:

Chosen for their high voltage and high near-infrared spectral response, silicon heterojunction (SHJ) solar cells are most commonly employed as rear cell, imposing a process temperature limit of 200°C for the perovskite top cell. Although textured silicon surface is superior in terms of light-management [158], the wet chemical deposition of the perovskite layer on a textured substrate has proven very challenging. Hence, most 2T devices include flat silicon bottom cell.

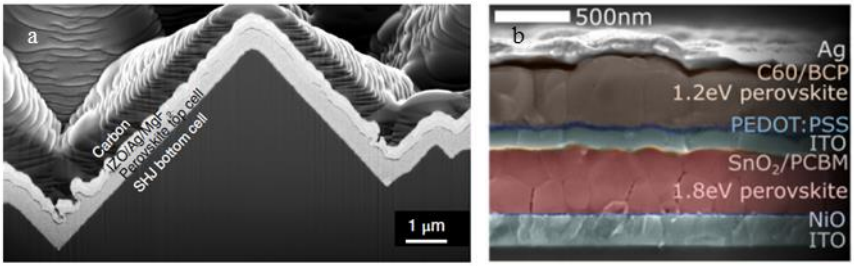

Figure 2.18 SEM images of the cells' cross sections for the 2T perovskite silicon tandem with focus on the uniform coverage of the textured silicon surface (a) [17][12] and the all perovskite 2T tandem showing the two subcells including their respective contact layers (b) [159][13].

Only recently, Sahli et al. [17] were able to successfully process a monolithic tandem solar cell on textured silicon using the hybrid deposition approach of co-evaporating the metal halide PbI_2 and CsBr followed by a wet chemical deposition

[12] Reprinted by permission from Springer Nature Customer Service Centre GmbH: Springer Nature, Nature Materials, „*Fully Textured Monolithic Perovskite/Silicon Tandem Solar Cells With 25.2% Power Conversion Efficiency*", F. Sahli, J. Werner, B.A. Kamino, M. Bräuninger, R. Monnard, B. Paviet-Salomon, L. Barraud, L. Ding, J.J. Diaz Leon, D. Sacchetto, G. Cattaneo, M. Despeisse, M. Boccard, S. Nicolay, Q. Jeangros, B. Niesen, C. Ballif, 2018

[13] Reprinted with permission from American Association for the Advancement of Science. From, Science, „*Perovskite-Perovskite Tandem Photovoltaics With Optimized Bandgaps*", G.E. Eperon, T. Leijtens, K.A. Bush, R. Prasanna, T. Green, J. Tse-Wie Wang, D.P. McMeekin, G. Volonakis, R.L. Milot, R. May, A. Palmstrom, D. J. Slotcavage, R.A. Belisle, J.B. Patel1, E.S. Parrott, R.J. Sutton, W. Ma, F. Moghadam, B. Conings, A. Babayigit, H.-G.Boyen, S. Bent, F. Giustino, L.M. Herz, M.B. Johnston, M.D. McGehee, H.J. Snaith, 2016

of the organic halide solution (cf. Section 2.5.4.2), thereby exceeding 25 % efficiency. Either different TCOs (e.g. ITO) or a nanocrystalline silicon layer poses as recombination junction, interconnecting the two cells. Depending on the perovskite structure, either the ETL (regular n-i-p) or the HTL (inverted p-i-n) follows the interconnection layer. Due to stability issues, such as light-induced phase segregation (Hoke-effect), for bandgaps exceeding 1.65 eV, a $CsFAPb(I_xBr_{1-x})_3$ composition with a bandgap of 1.63 eV is employed as absorber material in the top cell. A layer of LiF reduces reflectance at the front side, it is placed either below or on top the front contact (HTL/regular, ETL/inverted). A top TCO layer and in some cases an additional metal grid concludes the device stack. The cell's cross section is depicted in Figure 2.18 a, the SEM image shows the uniform coverage of the textured silicon surface.

Analogous to perovskite single junction, the applicable contacts and absorber materials in tandem solar cells cover a wide range and optimal combinations are still under investigation.

2.7.5 All Perovskite Tandem

Alternative to a silicon based design, two PSCs cells with optimized bandgaps can be combined to an all-perovskite tandem [159–161]. For highest efficiencies, the bandgap of the rear cell should range between 0.9 eV and 1.2 eV, the one complementing top cell one of 1.7 eV to 1.9 eV. Successful realization of such tandem solar cells in both 2T and 4T configurations was achieved by Eperon et al. [159], employing a 1.2 eV Pb/Sn alloy rear cell, a 1.8 eV mixed cation/mixed halide alloy with high bromine content for the 2T top cell and the established high-performing 1.6 eV perovskite absorber for the 4T configuration. Already in this early stage, the tandem efficiencies exceeded the single subcells' efficiencies. In Figure 2.18 b, a scanning electron microscope (SEM) image of the 2T cell's cross section is depicted in comparison to the silicon-based tandem.

2.7.6 Triple Junction

Only recently, a monolithic triple junction solar cell was reported, combining a SHJ rear cell with two perovskite cells on top [162]. The perovskite absorber consists of mixed cation/mixed halide alloys with varying Br/I ratio.

3 Characterization Techniques

Within the scope of this thesis, multiple characterization techniques have been developed, adapted and applied. The entity of these techniques provide information on charge carrier density and decay characteristics, band gap properties, local current extraction efficiency, heat dissipation and J-V characteristics. The theoretical foundations and details to the individual measurement setups are given in this chapter.

3.1 Photoluminescence

Analyzing the photoluminescence emission upon optical excitation is a non-destructive, contactless technique to probe the electronic structure and material quality of semiconductors. The generalized Plank equation (cf. Eq. (2.25)) describes the emission of photons as a function of the material's absorptivity and the chemical potential of the electron-hole pairs. It is derived from the transition rates, taking into account different electron distributions which are described by different Fermi functions [61]. The intensity of the emitted photoluminescence I_{PL} is proportional to the radiative recombination rate as described in Section 2.2.2.1.

$$I_{PL} = B_{rad} n_e n_h \tag{3.1}$$

Hence, the emitted PL intensity is a measure of the charge carrier density via inversion of Equation *(3.1)*, the absorption coefficient via *(2.22)* and the Fermi-level-splitting via *(2.25)*, making the PL emission a sensitive probe for a material's bandgap properties.

3.1.1 Confocal Microscopy

Conventional wide-field microscopy is subject to a resolution limit d:

$$d = \lambda / NA^2 \tag{3.2}$$

i.e. the resolution is a function of wavelength λ and numerical aperture NA, which gives the range of angles for light collection of an objective lens:

$$NA = n_{air} \sin(\beta) \tag{3.3}$$

with n_{air} being the refractive index of air as the immersion medium and β the angle of the light collection cone with respect to the optical axis. The resolution can be enhanced by introducing a pinhole into the detection pathway, thus suppressing light emitted away from the focal plane. In such a "confocal microscope", the detection is limited to a single spot and the microscopic image is assembled by raster scanning the sample via a movable x-y-stage. Under ideal conditions, the resolution can be enhanced by a factor of $\sqrt{2}$ in an confocal setup compared to conventional microscopy (cf. Equation (3.2)).

3.1.2 Microscopic Photoluminescence Spectroscopy Mapping

This section details the experimental setup used in this thesis.

Based on a commercially available confocal Raman scanning microscope, custom-made modifications have been added to the existing setup for the first experimental realization of confocal microscopic PL spectroscopy on silicon by Gundel et al. [163–168]. The setup has been developed further within the PhD thesis of Friedemann Heinz [169–171]. Suitable optical components for perovskite characterization have been added within this thesis.

Built in a modular system, it allows to combine various excitation and detection components. The overall setup enables spatially, spectrally and temporally resolved detection of emitted luminescence. Including all available components, the experimental setup is depicted in Figure 3.1:

The center shows the core of the tool, the confocal microscope. It is situated in a closed, optically opaque casing. Both excitation and detection pathways are realized via fiber-optics.

3.1.2.1 Excitation

On the excitation side, besides a Köhler white light source for conventional bright field microscopy, four different lasers are available in either continuous wave (cw) mode or frequency modulated (pulsed):

- 355 nm, frequency-tripled Nd:YAG solid state laser, cw mode
- 532 nm, frequency-doubled Nd:YAG solid state laser, cw mode
- 635 nm, diode laser, both cw and pulsed mode
- 905 nm, diode laser, both cw and pulsed mode

The different excitation sources are fiber-coupled to the microscope, employing collimating lenses to focus the parallel light output from the laser to the fiber core and re-establish a parallel light path after leaving the fiber. Usually, the excitation light is filtered by a suitable bandpass filter before being directed to the sample surface via a beam splitter, which ideally reflects the incident laser wavelength at 45° completely while totally transmitting the desired measurement parameter (back-scattered Raman or PL).

The parallel laser light is focused onto the sample surface using a lens: depending on the required resolution, the numerical aperture (NA) of the available lenses ranges between 0.26 ($\times$ 10 magnification) and 0.9 ($\times$ 100 magnification). For maximum resolution, merely limited by diffraction, a high NA lens (0.9) is employed. A benefit of the low NA lens is its lower sensitivity to surface topography variation due to its low depth of focus.

Upon excitation, the emitted PL or Raman signal, as well as the reflected laser light, is collected by the same lens. Ideally, the beam splitter would suppress any spurious laser light reflected from the sample surface, yet due to imperfect transmission/reflection properties, additional suppression via a long pass filter is necessary. The collected light is subsequently collimated by a stack of lenses and eventually transferred to the spectrometer via an optical fiber, the core diameter of which determines the confocal pinhole size. Available fiber core diameters are 25, 50, 100 and 1000 µm. While small confocal pinholes increase the resolution by decreasing the detection volume, they also weaken the signal intensity. For samples with low luminescence efficiency, the larger pinhole can be more suitable.

For recording the collected signal, multiple options are available, depending on the nature of the investigated signal and the demands on the desired outcome.

3.1.2.2 Spectrally Resolved Detection

For spectral resolution, lens-based (visible (vis) range) or mirror-based (near infrared (NIR) range) grating spectrometer featuring different grating properties (1800 g/mm, 600 g/mm for vis, 320 g/mm, 160 g/mm for NIR) are applied either for highest spectral resolution or to observe a broader spectral range in the visible range, respectively. Detectors suited for the probed spectral range are thermo-electrically cooled 1024 px silicon (vis range) or 512 px InGaAs (near IR range) line charge coupled devices (CCDs).

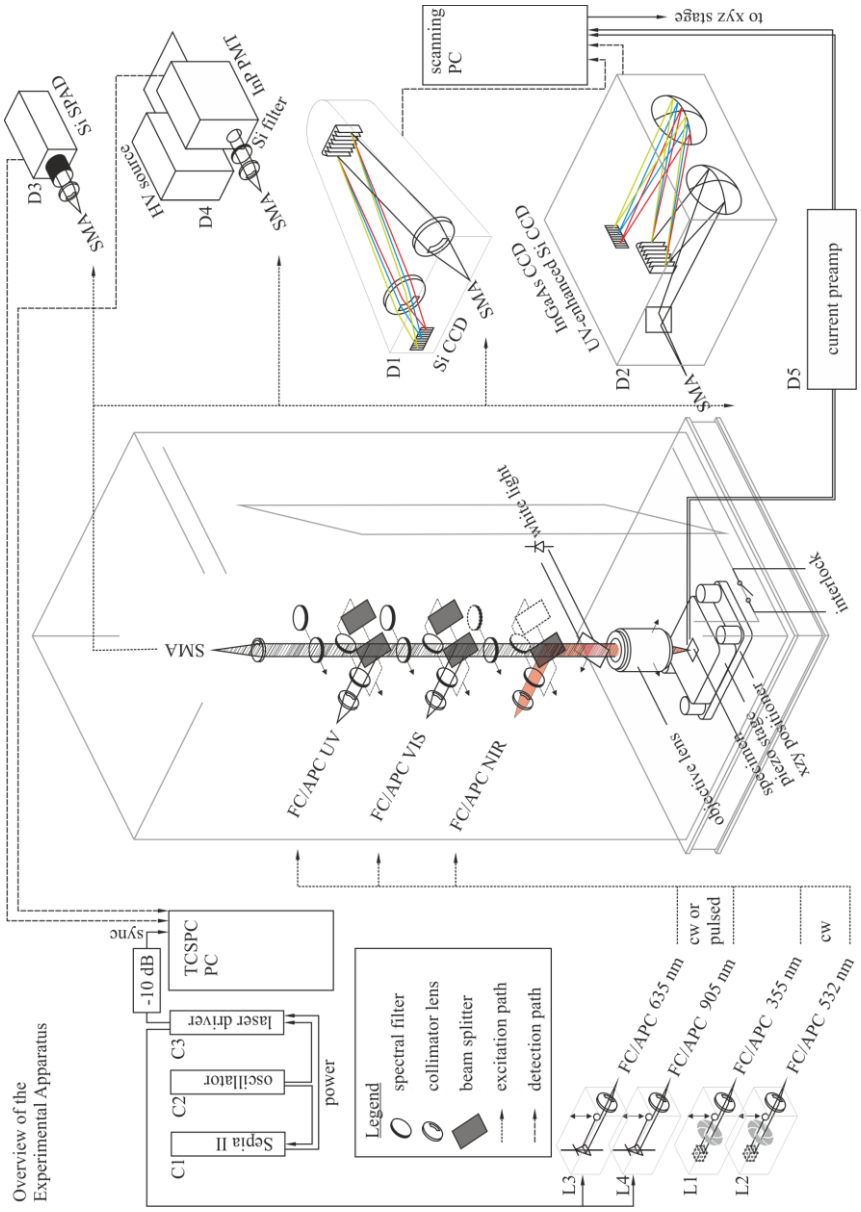
Overview of the Experimental Apparatus
Legend
spectral filter
collimator lens
beam splitter
excitation path
detection path
Sepia II
C1
oscillator
C2
laser driver
C3
power
- 10 dB
TCSPC PC
sync
FC/APC 635 nm
FC/APC 905 nm
FC/APC 355 nm
FC/APC 532 nm
L3
L4
L1
L2
cw or pulsed
cw
FC/APC UV
FC/APC VIS
FC/APC NIR
SMA
objective lens
piezo stage
xyz positioner
white light
interlock
D1
Si CCD
SMA
D2
InGaAs CCD
UV-enhanced Si CCD
SMA
D3
Si SPAD
SMA
D4
HV source
InP PMT
Si filter
SMA
scanning PC
to xyz stage
D5
current preamp

Figure 3.1 Schematic of the microscopic photoluminescence spectroscopy setup. The components are named in the legend if not labelled directly. [14]

3.1.2.3 Spatially Resolved Detection

The spectrally resolved analysis of the collected light is compatible with spatial resolution: a movable x-y-z stage is mounted below the lens, allowing to map the specimen. For highest spatial resolution, a piezo-stage can be added on top of the x-y-z stage, allowing steps in the sub-micrometer range. Controlling the height of the stage during the mapping is crucial to account for an inclined probe surface: As the confocal principle allows efficient collection exclusively from the focal plane, it yields highest spatial resolution, but one drawback is that deviation from the focal plane even in the low micrometer scale can significantly hamper extracting a meaningful image of the probed area. Hence, for most measurements, a 3-point-plane correction is applied. The stage's z-position is regulated to compensate slopes.

3.1.2.4 Time Resolved Detection

There are two approaches to investigate the temporal progress of a detected signal: the spectrally resolved detection can be applied in a fixed position and monitored over time with measurement frequencies up to 100 Hz, thereby allowing to track the spectral evolvement of the signal over milliseconds up to several hours.

If the PL decays with decay constants below 1 ms are of interest, the spectral resolution is discarded in favor of efficient, spectrally integrated, signal detection. For this purpose, two time-correlated single photon counting (TCSPC) detectors can be attached via optical fibers: a photomultiplier, highly sensitive in the IR range, and a single photon avalanche diode (SPAD) sensitive in the visible range. With this detection mode, the transient decay of PL signals down to the nanosecond regime can be recorded.

3.2 Light Beam Induced Current

For samples capable of charge carrier separation, current can be tapped from the contacts upon charge carrier generation (cf. 2.2.1). The current density is strongly related to the local charge carrier extraction probability, which is a function of the diffusion length, the contact resistance and can by influenced by charge carrier

[14] By courtesy of Dr. Friedemann Heinz

annihilation e.g. due to recombination (cf. 2.2.2). Probing the electrical current upon local excitation therefore yields access to these properties. Using the microscopic setup introduced in the previous section, local excitation can be achieved using the focused laser light while the current can be detected via a low-noise lock-in amplifier as depicted in Figure 3.1 (D5). This optical excitation approach is well-established and commonly known as light beam induced current (LBIC) [172–174]. Since only a small part of the device is illuminated, the resulting current is in the range of pA-µA.

3.3 Lock-In Thermograpy

The detection of infrared (IR) black body radiation via thermography imaging is a non-destructive characterization technique for solar cells. A rigorous approach can be found in the book by Breitenstein, Warta and Langenkamp [175]. In this section, an introduction based on their work is given and the measurement setup used in this thesis is presented.

Locally dissipated power due to increased non-radiative recombination and shunts are detected using an IR sensitive camera, which integrated the emission spectrum over a defined spectral range. Planck's Law of Radiation gives the spectral specific irradiation $M_\omega(T)$ as a function of temperature (Equation (3.4)). For non-ideal emissivity $\epsilon \neq 1$ ("grey emitter" for wavelength-independent emissivity), the deviation needs to be taken into account. The spatially resolved emissivity can be derived by comparison of two thermography images at different temperatures (cf. [175]).

$$M_\omega(T) = \frac{\hbar\omega^3}{4\pi^3 c^2} \frac{1}{\exp\left(\frac{\hbar\omega}{kT}\right) - 1} \tag{3.4}$$

Sensitivity and spatial resolution can be increased several orders of magnitude compared to steady-state thermography by employing a lock-in based analysis: The black body radiation at constant temperature constitutes a non-negligible offset. By evaluating the difference between the large offset and the additional signal of interest, the lock-in principle is ideally suited for this analysis.

The correlation of the noisy, temporally modulated measurement signal $F(t)$ with a symmetric square-wave reference signal $K(t)$ yields the integrated product signal S:

$$S = \frac{1}{t_{int}} \int_0^{t_{int}} F(t)K(t)\,dt \text{ with } K(t) = \begin{cases} +1, & 0 \leq t < \frac{t_{int}}{2} \\ -1, & \frac{t_{int}}{2} \leq t \leq t_{int} \end{cases} \tag{3.5}$$

with t_{int} representing the chosen integration time. Reference and measurement function share the same periodicity, the lock-in frequency $f_{lock-in}$, thereby any DC component in the measurement signal is effectively suppressed. For physical measurements, the functions transition into discrete measurement values F_k and weighting factors K_k. The measurable output is the average up to the number of measured periods $N = t_{int} \times f_{lock-in}$:

$$S = \frac{1}{N}\sum_{k=1}^{N} F_k\, K_k \tag{3.6}$$

The harmonic functions, sine and cosine, are employed for these weighting factors, delivering a superior signal to noise ratio compared to the square wave function. Using both harmonic functions enables access to the phase of the signal: while the sine function is in phase with the applied bias modulation, the cosine is in phase with the temperature response. The total signal $F(t)$ can be described as a function of amplitude A and phase ϕ:

$$F(t) = A\sin(2\pi f_{lock-in}\mathrm{t})\cos(\phi) + A\cos(2\pi f_{lock-in}\mathrm{t})\sin(\phi) \tag{3.7}$$

Using the weighting factors

$$K^{0^\circ}(t) = 2\sin(2\pi f_{lock-in}\mathrm{t}) \tag{3.8}$$

$$K^{-90^\circ}(t) = 2\cos(2\pi f_{lock-in}\mathrm{t}) \tag{3.9}$$

in Equation (3.5), this yields the following correlations for amplitude and phase:

$$A = \sqrt{(S^{0^\circ})^2 + (S^{-90^\circ})^2} \tag{3.10}$$

$$\phi = \arctan\left(-\frac{S^{-90^\circ}}{S^{0^\circ}}\right) \tag{3.11}$$

$$S^{0^\circ} = A\sin(\phi) \tag{3.12}$$

$$S^{-90^\circ} = -A\cos(\phi) \tag{3.13}$$

$$S^{-45^\circ} = \frac{1}{\sqrt{2}}\left(S^{0^\circ} + S^{-90^\circ}\right) \tag{3.14}$$

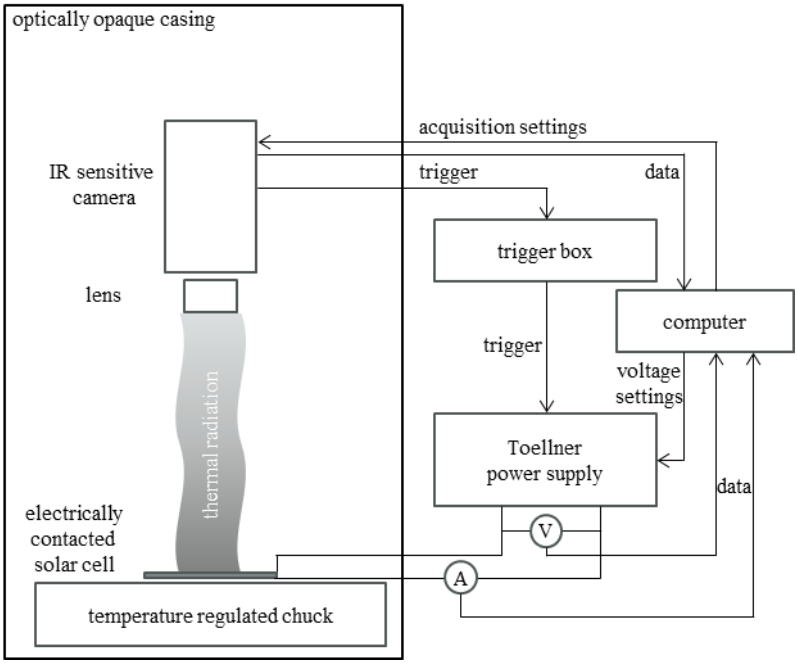

Figure 3.2 Schematic illustration of the experimental lock-in thermography setup. Periodic excitation can be induced by applying an external voltage or illumination via LED arrays (wavelengths: 470 nm, 655 nm, 950 nm).

The setup used for the characterization in this work is schematically depicted in Figure 3.2, it is a custom-made tool by the company IRCAM GmbH. The camera contains a InSb based midwave infrared focal plane array (MWIR FPA) detector, sensitive to IR radiation in the range of 1.5 to 5 µm and is actively cooled resulting in a low signal to noise ratio and a temperature resolution limit of < 20 mK. Available excitation sources include external bias voltage via a Toellner four-quadrant power supply. Current and voltage at a given excitation are monitored in steady-state conditions before and after the lock-in measurement via two multimeters. A water-cooled copper chuck can be used for electrical contacting solar cells with accessible back contacts.

3.3.1 Dark Lock-In Thermography

For quantitative interpretation of the local thermography signal, thermally thick and thermally thin samples have to be distinguished:

Generally, the distribution of heat in a 3-dimensional isotropic and homogeneous solid is given by the non-steady-state heat diffusion equation:

$$p = \lambda_{th}\Delta T - c_p \rho \frac{\partial T}{\partial t} \tag{3.15}$$

The dissipated power p is determined by the heat conductivity λ_{th}, the specific heat c_p and density ρ of the material and the change in temperature T over time t. This equation can be solved for given temporal and geometric boundary conditions. It can be found, that the heat distribution of a plane thermal wave is quantified by the thermal diffusion length Λ with the frequency $\omega = 2\pi f_{lock-in}$:

$$\Lambda = \sqrt{\frac{2\lambda_{th}}{c_p \rho \omega}} \tag{3.16}$$

This thermal diffusion length is also a measure for distinguishing thermally thin and thermally thick samples. If the sample thickness d is small in comparison $d < \Lambda$ the sample is considered thermally thin, for the case $d > \Lambda$ it is classified as thermally thick.

The quantitative interpretation of thermography images is based on the strong dampening of thermal waves within the sample. Therefore, the average thermal signal in an area is proportional to the averaged dissipated power density in the same area. Depending on the thermal thickness of the sample, the following relations can be derived based on the phase of the temperature modulation at the sample surface:

$$p_{loc}^{thin} = \frac{S_{loc}^{-90°}}{S_{whole}^{-90°}} \frac{P_{whole}}{A_{whole}} \tag{3.17}$$

$$p_{loc}^{thick} = \frac{S_{loc}^{-45°}}{S_{whole}^{-45°}} \frac{P_{whole}}{A_{whole}} \tag{3.18}$$

Where the global dissipated power density is calculated from the applied bias voltage V_{bias} and the corresponding global cell current density J. A_{whole} refers to the cell area.

3.3.2 Local Current-voltage Characteristics

Moving on from the local dissipated power density, the current density can be calculated taking into account the applied voltage including the voltage drop due to series resistance. Assuming either a global series resistance R_s or using a previously determined distribution of it e.g. by series resistance imaging [176, 177], the local voltage can be calculated and thus the local current density.

Given the current density distribution for a variation of bias voltages, the current-voltage characteristics can be evaluated for each pixel from the following equation:

$$p_{loc} = j_{loc} \times v_{loc} = j_{loc} \times (V_{bias} - R_s \times j_{loc}) \tag{3.19}$$

$$j_{loc} = \frac{V_{bias}}{2R_s} - \sqrt{\frac{V_{bias}^2}{4R_s^2} - \frac{p_{loc}}{R_s}} \tag{3.20}$$

The iterative fitting procedure of the 2-diode-model (cf. Section 2.3) to the local dark J-V curves was introduced by Breitenstein [178, 179].

Following the superposition principle, stating the illuminated J-V characteristics equal the dark characteristics shifted by the short-circuit current density at standard illumination conditions ($1000\ \mathrm{W/m^2}$, AM1.5g), the analysis further yields the light J-V curve with neglect of the series resistance.

$$\mathrm{J}_{illum}(V) = \mathrm{J}_{dark}(V) + \mathrm{J}_{sc} \tag{3.21}$$

The principle is based on the assumption that the photo-induced current is independent of the voltage. Apart from the parameters of the 2-diode-model, light J-V parameter such as the open-circuit voltage V_{oc} and the pseudo fill factor pFF (neglecting the influence of the series resistance) are obtained via this analysis.

4 Temporal Evolution of Perovskite Absorber Materials

The dynamic mechanisms in halide perovskite materials and solar cells exhibit a vast diversity of time scales. While molecular movements can be observed on a picosecond scale [180], the long-term stability of PSCs is tracked over months [26]. Monitoring these dynamics in real time is a convenient approach towards the creation of insight in the underlying mechanisms and in situ characterization techniques are widely used [180–194].

One major field of application for in situ studies is the analysis of various degradation mechanisms in halide PSCs. An examples is the bias-induced degradation study by Jeangros et al. using transmission electronic microscopy, revealing iodide migration from the $MAPbI_3$ active layer to the HTL [186]. Reversible and irreversible process due to moisture was monitored with spatially resolved LBIC mapping by Song et al. [54], highlighting the lateral heterogeneity of the degradation which was also shown by an UV degradation study in a joint investigation with the Korea University within this thesis [195].

Another equally important research topic concerns the formation of perovskite rather than its decomposition. Again, in situ techniques serve as powerful tools in the analysis of the crystallization mechanism and the influence of various processing parameters:

Influence of precursor solutions and intermediate crystalline solvates was explored during standard solution processing as well as during roll-to-roll and blade coating [181, 189, 196, 197]. Engineering the thermal treatment based on in situ analyses during the annealing enabled improvement of the photovoltaic performance and revealed changes in the crystal orientation along with expansion and contraction of the crystal lattice [183, 193, 198–200]. Optimizing the anneal temperature profile and the atmosphere is crucial, as exceeding the optimal annealing time or temperature can lead to degradation [183, 191, 199, 201]. Relating the obtained results from in situ characterization of the crystallization to solar cell performance is fundamentally hindered by the processing sequence of PSCs. As the counter electrode is usually deposited on top of the fully crystallized and annealed perovskite layer, probing the photovoltaic performance during the perovskite formation is not possible. Therefore, most studies were limited to stepwise and sequential processing of complete solar cells at different stages of the crystallization [191, 198, 199, 201–204]. After the study published by the author, only one more report of direct correlation between crystallization and photovoltaic performance was published [182]. Their experiment is based on an interdigitated back-contact (IBC) cell design, enabling J-V sweeps during

the thermal annealing, alternating with grazing incidence wide angle X-ray scattering (GI-WAXS) measurements.

The study presented in this chapter is focused on the correlation between electrical and optoelectronic properties of $MAPbI_3$ during the film formation as a demonstration of exploring the temporal evolvement in perovskites.

Furthermore, in situ techniques were used within this thesis to analyze the photo-stability of high bandgap perovskite absorber materials with mixed halide content and the recrystallization during post-deposition treatments. The latter was the topic of a master thesis supervised by the author [205].

This section is divided in an introduction of the graphite-based solar cell architecture and its most important properties, the absorber layer formation process and the experimental outline, followed by the main findings from the in situ characterization. Finally, a model for the crystallization process is proposed and discussed with regard to findings that are more recent. A detailed description of the manufacturing process and the materials used can be found in the appendix 7.1.2.

This study represents the result of a close collaboration within Fraunhofer ISE, including Lukas Wagner, Gayathri Mathiazhagan and Markus Mundus. While Markus Mundus was in charge of the EQE measurements, Gayathri Mathiazhagan kindly prepared the samples for this experiment. The author performed all PL related measurements, and together will Lukas Wagner, the author developed the proposed crystallization model, planned and supervised the overall project and additional characterization. This very close collaboration led to a shared first-authorship in the joint journal publication, which is the basis for this chapter [206].

4.1 In situ Characterization of Perovskite Crystallization

Whereas previous in situ studies were limited to perovskite film formations, as the charge selective layers usually are deposited subsequent to the absorber layer, the utilized cell structure in this study represents a complete device shell prior to the perovskite formation. Hence, the main novelty in this study is the direct correlation of optoelectronic properties with solar cell performance during the crystal formation, enabled by the choice of device architecture for this in situ characterization and finally closing the gap between crystallization and photovoltaic efficiency. The employed device structure is a graphite-based, monolithic PSC with porous contact layers, where the $MAPbI_3$ crystallization takes place within the PbI_2 filled scaffold upon immersion of the device in MAI solution. During the complete process, the spectrally resolved PL

emission was tracked and linked to the EQE for a fixed wavelength, representative for the overall EQE spectrum.

One major finding is the existence of a hitherto unknown stage during the cell manufacturing process, which mainly influences the charge extraction and therefore the cell current.

4.1.1 Graphite-Based Cell

The graphite-based cell architecture, which was employed for this investigation, yields the particular benefit of including both ETL and HTL before the absorber is formed [207–210]. Following the two-step deposition route [152], a porous layer filled with PbI_2 is sandwiched between TiO_2 and a permeable hole contact comprised of graphite flakes. The conversion of PbI_2 to $MAPbI_3$ takes place upon this shell's immersion into a precursor solution containing MAI. Thus, the crystallization can be analyzed in immediate correlation to the cell's photovoltaic performance. The layer stack of the monolithic graphite-based cell is depicted in Figure 4.1:

On top of a FTO coated glass substrate, the TCO was patterned by laser ablation. A $25-30\,\mathrm{nm}$ thick layer of compact TiO_2 combined with a $600\,\mathrm{nm}$ layer of mesoporous TiO_2, comprises the ETL. $800\,\mathrm{nm}$ of mesoporous ZrO_2 serves as space layer between the ETL and the $7\,\mu\mathrm{m}$ thick graphite HTL. Hence, the complete mesoporous layer, which is eventually filled with $MAPbI_3$, is 1.4 µm. Both the ZrO_2 and the TiO_2 porous layers were screen-printed, as was the graphite layer. The compact TiO_2 layer was deposited by spray-pyrolysis. The porous layers were filled with PbI_2 by dropping a DMF/PbI_2 solution on top of the permeable graphite and a short (10 s) spin coating step after a one minute waiting period during which the sample rested at 70 °C. The location of the drops in the active cell area could be identified in spatially resolved PL maps (cf. Figure 4.8) in the post-annealing phase of the cell process (cf. Figure 4.3). Electrical contact to the solar cell were established by soldering cables to the corresponding TCO patches and applying silver paste to contact the graphite electrode. Converting the PbI2 to MAPbI3 is done in two three steps, dipping the prepared cell precursor in MAI solution, taking it out and drying it in ambient air and annealing the cell on a hotplate at 70° C. Each of the three steps takes 30 minutes. The immersion of the device stack is done with the non-transparent but permeable hole contact, comprised of the graphite flakes, facing the MAI solution. Consequently, the transparent glass side faces upwards and allows for illumination and probing by PL spectroscopy.

More details on the manufacturing of the cell precursor and the used materials can be found in the corresponding publication's supplementary information [206].

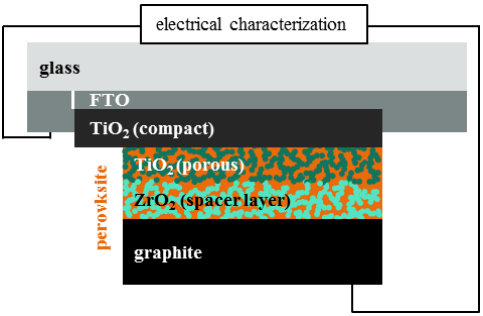

Figure 4.1 Schematic cell design for the graphite based PSC.

In Figure 4.2, an SEM image of the cell's cross section, prepared by focused ion beam treatment and after completing the perovskite formation, is depicted. The upper edge of the image shows part of the multiple micrometer thick graphite hole contact, which is also clearly recognizable in the alongside energy dispersive x-ray spectroscopy (EDX) map, showing a distinctive carbon fraction marked in red. On the low end, the TiO_2 layer is visible in cyan below the ZrO_2 layer, highlighted in magenta. Pb (yellow) is visible in all porous layers. Preparing the cross section was necessary as the edges of broken fragments showed no clean and even surfaces, stretches of the porous layer turned out to be ripped from both sides of the cut. Hence, obtaining informative results from the elemental analysis via EDX was only possible after careful preparation of the cross section with the focused ion beam.

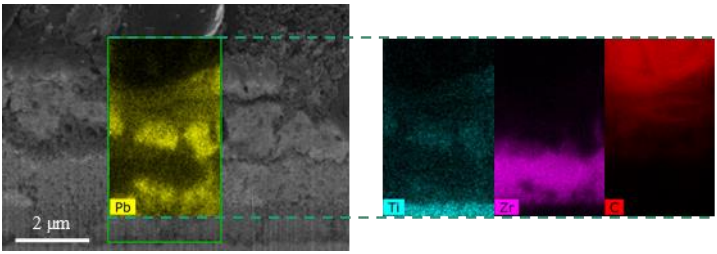

Figure 4.2 SEM image along the cross section a perovskite filled graphite cell and close-up images of EDX-maps for the elements Pb (indicating perovskite infiltration inside the porous scaffold), Ti (indicating the porous TiO_2 electron selective layer), Zr (indicating the porous ZrO_2 space layer) and C (indicating the porous graphite back electrode).

4.1.2 Measurement Protocol and Conditions

The aim of the overall experiment was to gain insight in the formation of perovskite crystal and the correlated photovoltaic behavior in the early stages of the cell formation. Therefore, the conversion process was tracked starting with the immersion of the precursor shell into the MAI solution, the "dipping" phase. Subsequently, the Petri dish, containing the solution, was removed and the solvent residues vaporized during the drying in ambient air ("drying" phase). Due to experimental restrictions, monitoring the parameter during the annealing phase was inhibited and, therefore, the measurements were continued after the annealing for another 10 minutes. This part will be referred to as "post-annealing" in the following.

Figure 4.3 shows the measurement protocol for this two-step process, indicating the four phases "dipping", "drying", "annealing" and "post-annealing" and the respective duration. During the first two and the last, multiple characterization techniques have been employed. Since the different techniques could not be performed simultaneously, each measurement was performed on a new cell. The overall count of samples analyzed in this study exceeds 50.

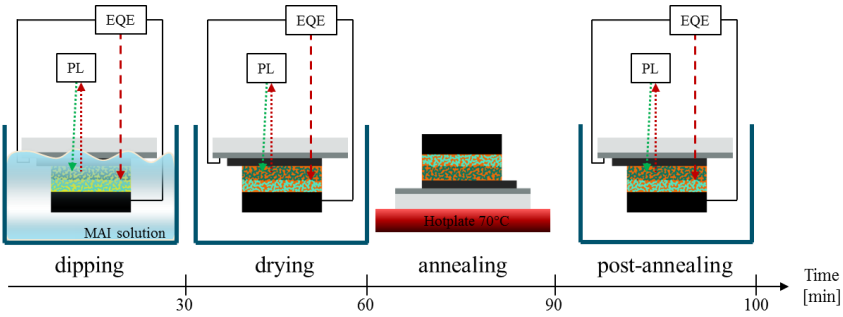

Figure 4.3 Experiment protocol for the two-step dipping in MAI solution.

- Optical inspection:
  Photographs were taken during the first 10 minutes of the dipping phase. The formation of perovskite is visible by eye as the color changes from yellow PbI_2 to the absorbing black phase of the $MAPbI_3$ perovskite. (cf. Figure 4.7)

- Photoluminescence:
  Two methods based on the perovskite's PL emission were employed: Spectrally resolved photoluminescence was tracked using the PLS setup as described in 3.1.1, without employing a lens to focus the laser excitation flux.

The illumination spot was $2.8 \times 10^{-2}\mathrm{cm}^2$ (calculated from the full width at half maximum (FWHM) of the laser illumination profile); hence it yields an average subset of the overall cell area. An excitation photon flux of $2.68 \times 10^{17}\mathrm{photons/s\,cm}^2$ (close real cell operation conditions) and an excitation wavelength of 532 nm was generated with the Nd:YAG solid-state laser. The emitted PL was continuously detected with an integration time of 0.1 s, equivalent to a repetition rate of 10 Hz. Spectral analysis was performed using a Gaussian fit, yielding a measure for the intensity (peak height) and the bandgap (peak position).

Additionally, PL imaging was performed, yielding the spatially resolved, spectrally integrated PL intensity. Homogeneous excitation was achieved via LED arrays and the emitted PL was detected in reflection mode via a Si-CCD camera. Yet, several experimental obstacles impeded comprehensive analyses: While the main emission was around 470 nm, unneglectable emission at higher wavelengths was detected when closer examining the excitation spectrum (cf. Figure 4.4). With the purpose of filtering spurious excitation light, a 750 nm long-pass filter was mounted in front of the camera. However, the LED emission coincides with the PL emission and even though it is multiple orders of magnitude lower than the main peak, it still influences the detected signal. The PL images shown in xy nevertheless support the justification of PL and EQE analyses with local probing of the device area.

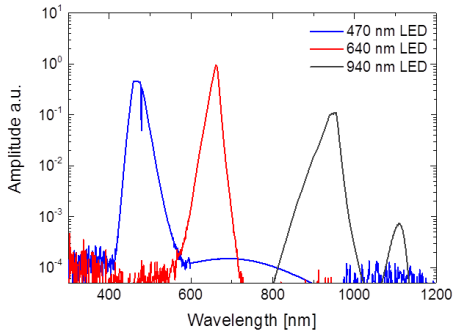

Figure 4.4 Emission spectra of LED excitation source employed for imaging the PL emission.

- External Quantum Efficiency:
  The spectral response was conducted with an in-house built, laser-based system at Fraunhofer ISE. A comprehensive description of the setup can be found in the PhD thesis by Markus Mundus [211], who built the setup and conducted the measurements in this study. Two types of illumination were used during the measurement [212]: a steady-state bias light from LEDs with emission peaks at $465\,\text{nm}$ and $660\,\text{nm}$ was employed at an illumination intensity of $1.1 \times 10^{16}\text{photons/s cm}^2$. For a complete device, this intensity equals a bias irradiance of approximately 0.1 suns. Additionally, the cell was probed with monochromatic, frequency-modulated light of $350\,\text{nm}$, $520\,\text{nm}$ or $700\,\text{nm}$. The modulation was realized via mechanical chopping wheels at frequencies between 70 and $90\,\text{Hz}$. Using a transimpedance amplifier, the cells were operated at short-circuit conditions. For the detection of the generated current, lock-in amplifiers were used to distinguish between the modulated current (AC signal) generated by the monochromatic illumination and the current generated by the continuous bias illumination (DC signal). Assuming linearity of the devices, their differential current response to the chopped monochromatic radiation is approximated as EQE [212]. As the illuminated area exceeded the cell are, a shadow mask of approximately $0.4\,\text{cm}^2$ was placed on top of the glass. The setup has been calibrated by a silicon reference solar cell and fluctuations of the monochromatic light were corrected by using a silicon monitor diode.

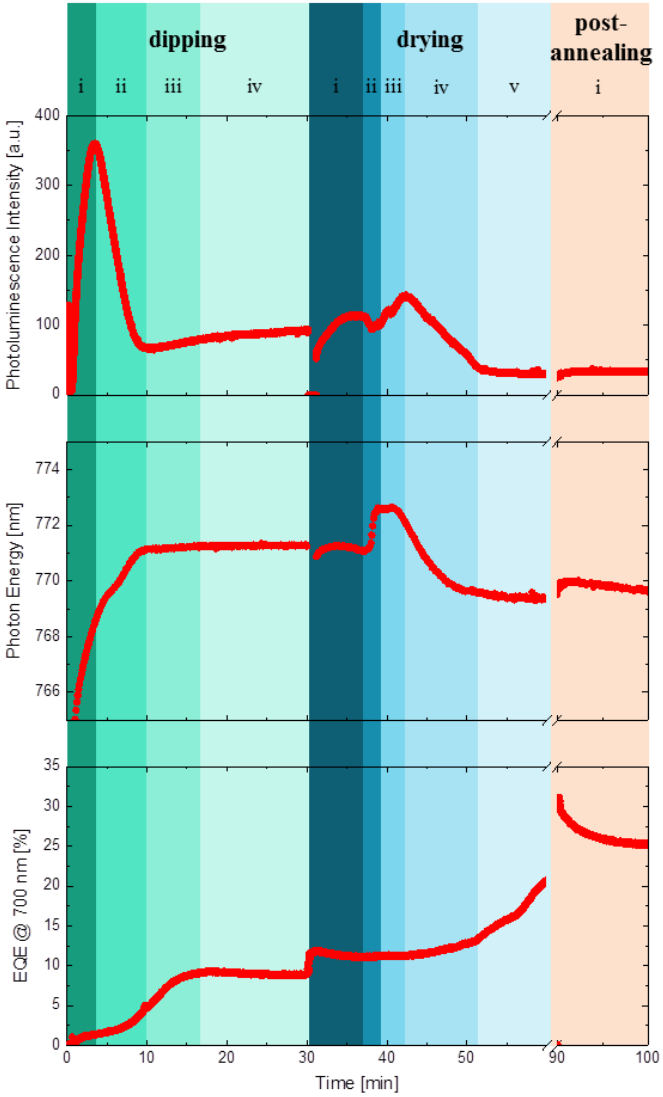

Figure 4.5 Summary of the in-situ characterization of graphite-based perovskite solar cells. The PL emission intensity and its peak position as well as the EQE at $700\,nm$ is shown as a function of time throughout the processing stages of dipping, drying and additional 10 minutes tracking after the thermal annealing.

Table 4.1 Categorization of evolution in PL emission properties and EQE during the crystallization

phase	stage	PL intensity	PL peak position	EQE (700nm)
dipping	(i)	steep rise	rise	rise
	(ii)	decrease	rise, reduced slope	rise, reduced slope
	(iii)	small increase	constant	very steep rise
	(iv)	small increase	constant	constant
drying	(i)	rise	slight arch	constant
	(ii)	dip	very steep rise	constant
	(iii)	rise	constant	constant
	(iv)	decrease	decrease	rise
	(v)	constant	constant	steep rise
post-annealing	(i)	constant	small increase	very steep decrease
	(ii)	constant	small decrease	decrease

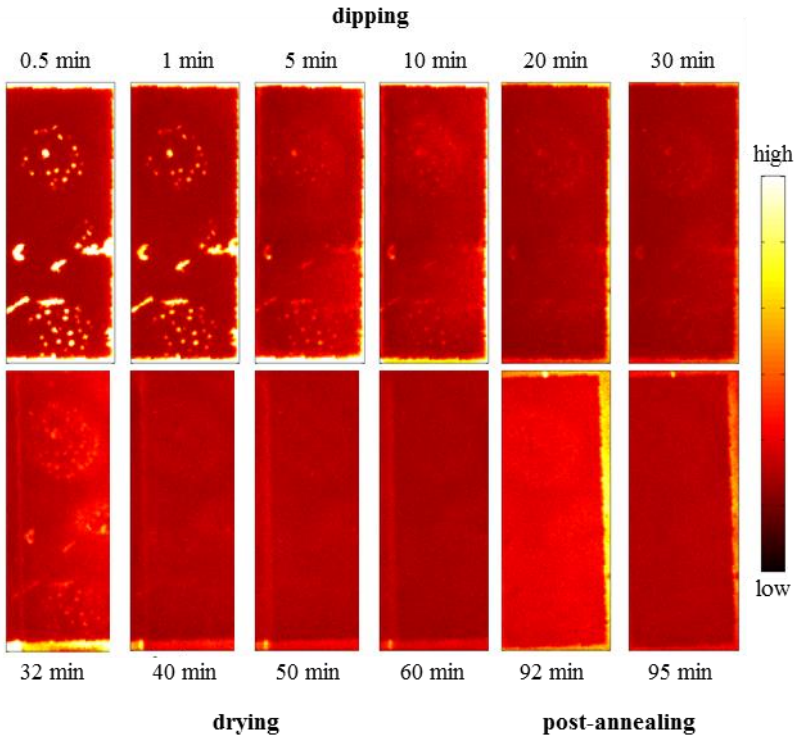

Figure 4.6 PL imaging of one cell throughout the dipping/ drying process and after the annealing. Initial heterogeneities fade out during the perovskite formation. Shown is the active cell area of 0.4 cm^2.

4.1.3 In Situ Results

The results obtained by the spectrally resolved PL measurements and the EQE at 700 nm throughout the dipping, drying and post-annealing phases are summarized in Table 4.1 and Figure 4.5. For the first phase, photographs of the film transformation were taken; the pictures are shown in Figure 4.7. The findings for the individual phases will be discussed in the following subsections:

4.1.3.1 Dipping Phase

Even by eye, the characteristic change from yellow (PbI_2) to the back perovskite phase can be seen. Photographs of a cell, its lower side immersed in MAI solution, are depicted in Figure 4.7. After 10 minutes, no more change is observed. In the image at

0 min, the active cell area of 0.4 cm^2 is highlighted by the dashed green rectangle. Already from the photographs, it can be seen that the conversion is not perfectly homogeneous. Looking at the results from the PL imaging in Figure 4.6, it can be seen that initial heterogeneities fade out, the contrast slowly attenuating in this first phase.

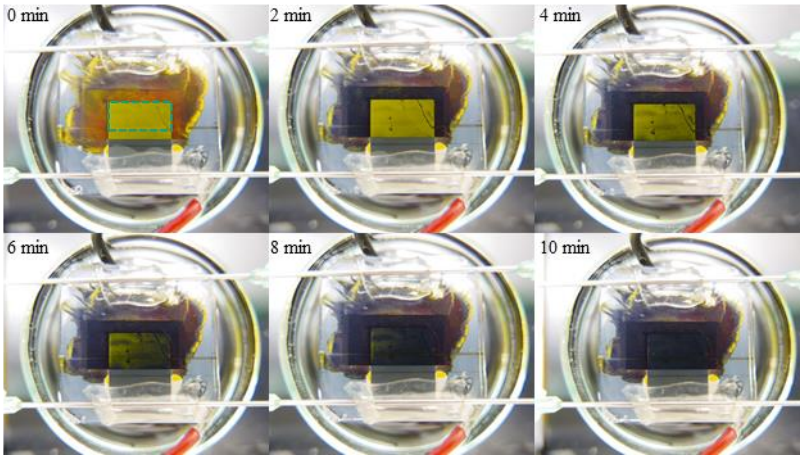

Figure 4.7 Optical inspection of the conversion of PbI_2 to the absorbing black phase of $MAPbI_3$ perovskite. Photographs were taken every two minutes during the dipping until no more changes were observed (>10 min). In the first image (0 min), the active cell area is highlighted by a green dashed rectangle. The size of the active are is 0.4 cm^2.

Figure 4.5 shows the PL intensity, the spectral position of the PL peak and the EQE at 700 nm during the reaction of PbI_2 and MAI within the first 30 minutes. From the change of dynamics in the PL and EQE signals, four different stages during perovskite crystallization in this dipping phase can be distinguished, as indicated by different shades of green in Figure 4.5. The onsets of the stages do not match completely between the PL and the EQE at 700 nm as they were recorded on different cells. Illumination with 700 nm wavelength was chosen from the flat region of the EQE spectral curve, which significantly contributes to the overall short-circuit current. Table 4.1 summarizes the evolution of the measured variables during the perovskite formation.

While the PL intensity shows a pronounced peak with its maximum after little over 3 min and mostly stabilizes after the end of stage (ii) after 10 min, the spectral position changes consequently, with two different slopes, until it reaches a constant value of

771 nm at the end of stage (ii). This value is well in agreement with the bandgap of $MAPbI_3$ of 1.6 eV. With a steady spectral position, major changes in the crystal lattices can be excluded. With the conversion of PbI2 to MAPbI3, the formed perovskite crystals start to absorb light and immediately charge carriers are extracted via the contacts, resulting in a measureable current. Remarkably, after the crystallization is assumed to be complete, the EQE shows a major increase before it stabilizes, introducing stage (iv). This suggests the existence of an additional stage in the perovskite formation within the mesoporous scaffold.

4.1.3.2 Drying Phase

For the next phase, the now complete solar cell is lifted out of the solution and placed in a new and empty Petri dish, in order to maintain the same height/position during the measurements. The heterogeneities dissolve themselves until the end of the drying phase, the contrast slowly subsiding.

Both the PL intensity and the spectral peak exhibit strong variation in their behavior during the drying. During recent in-situ studies of the crystallization during thermal annealing, changes in the grain orientation and lattice strain were detected [182, 188]. These analyses were based on GI-WAXS measurements, yet the PL spectrum is also very sensitive to changes in the crystal lattice. Despite the absence of thermal energy (drying at room temperature), the same mechanism is presumed to cause the change in the PL related parameter. Additionally, the evaporating solvent can affect the PL emission although the absorption of the excitation light is not influenced as the EQE rises with increasing slope during the drying period without reflecting the intermediate changes in the PL.

4.1.3.3 Post-Annealing Phase

Subsequent to the annealing at 70 °C, the only remarkable change in the measured parameter is the decrease in the EQE. After the initial drop, the EQE gradually approaches a stable value during the 10 min of tracking. Most likely, this degradation is due to the migration of ions in the electric field.

Neither the PL intensity nor the spectral peak position exhibit major variation during this phase. After the in-situ tracking was completed, the samples were mapped using the confocal microscope, which had already been used for the time dependent PL measurements. For the mapping, a lens with a numerical aperture of 0.26 was used. Maps of the intensity and the spectral peak position are depicted in Figure 4.8, following the identical fitting procedure. Largely, the lateral distribution is homogeneous, yet the two PbI_2 dropping spots are still perceptible as indicated by the white dashed circles. The green dashed circle indicates the illumination spot during the

in situ measurement. Most important was the finding that the measurement area appears not to be influenced by the illumination. Subsequent to this study, reports of the impact of illumination on the crystallization process were published by Ummadisingu et al. [194].

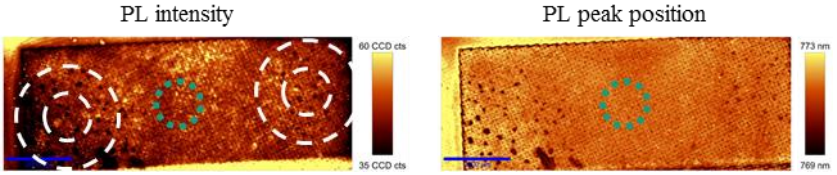

Figure 4.8 Maps of the PL intensity and spectral peak position of a complete device processed by the two-step immersion protocol with simultaneous PL characterization. White dashed circles indicate the PbI_2 dropping area, the green dashed circle the spot of the laser excitation, indicating that the illumination has no traceable effect on the sample. The blue scale bar corresponds to 2 mm.

4.1.4 Perovskite Crystallization

In the next section, a model is suggested for the crystallization of this two-step reaction process from solution during the initial crystal formation in the dipping phase. From the observation that a major contribution of the photocurrent is generated after the crystallization is assumed to be complete, judging from the early peak in PL intensity and the stabilization of the spectral position of the emitted PL, it is concluded that an important step towards efficient charge extraction is the formation of electrical pathways. The suggested model is illustrated in Figure 4.9:

In the first stage (i), the MAI solution infiltrates the mesoporous scaffold immediately after the lower part of the cell (graphite electrode facing down) is immersed in the solution. This initiates the nucleation of the $MAPbI_3$ perovskite crystals on the PbI_2 gain surface, which results in a strong initial increase in the PL emission intensity (cf. Figure 4.5) as the perovskite crystals start absorbing the excitation light and charge carriers recombine via radiative emission [190, 191, 202, 203, 213, 214].

As the emitted PL is sensitive probe of the material's bandgap, the photon energy gives indications about the crystal lattice. The correlation between crystal size and the strain on the lattice, therefore also the bandgap, has been revealed by multiple groups. With increasing crystal size, the lattice strain is released, resulting in a smaller bandgap and consequently a red shift of the PL spectrum [81, 84, 85, 116, 215–219]. Consequently, the time-dependent red shift in the spectral position can be interpreted

as crystal growth during this first stage until the end of the second stage. The assumed increase in the crystal size is well in agreement with previous findings on the crystallization process of $MAPbI_3$ in a two-step deposition [203, 213]. Were the change in the spectral position accompanied by a change in shape that is getting more narrow, it could also be influenced by reabsorption [220], yet such a narrowing was not observed in this experiment.

This was the first in situ measurement of the EQE during the perovskite crystallization, and the EQE at the chosen excitation wavelength of 770 nm is interpreted as a measure for the generated photocurrent. Therefore it was surprising to find that current is generated almost immediately after the perovskite nucleation commences in stage (i). This suggests that even though the crystals mainly formed on the PbI_2 crystals' surface, few electrical pathways are already established rather than persisting electrical isolation of the individual crystals, enabling the extraction of generated charge carriers. Observing the changes in slope for the EQE and the PL peak position for the stages (i) and (ii), a variation in the crystallization kinetics is presumed. In agreement with previous reports [190], the second stage is governed by a diffusion-limited transport of the MAI solution through the emerged shell of perovskite crystals, which have initially been formed at the PbI_2 crystal's surface.

As the strong decrease in the PL intensity is not reflected in a very strong increase in the charge extraction efficiency during the second stage (ii), this is likely to be caused by increased non-radiative recombination. Some extend of remnant PbI_2 was shown to have beneficial effects [221–224], hence complete conversion might have a detrimental influence on the defect density.

Judging from the end of changes in the optical appearance of the active layer as well as the PL emission properties, the crystallization process is complete after the end of stage (ii). This conclusion is in accordance with reports of in situ XRD data from one-step processes on pristine perovskite films [75, 76].

The existence of stage (iii) is the most significant finding and novelty of this study: after the crystal formation is complete, the extracted photocurrent, probed by the EQE, shows a strong increase. Hence, another mechanism induces more efficient charge extraction. If these changes were caused by reorientation or other changes in the perovskite crystals, the shape of the PL emission spectrum would reflect this. Much more likely is the improvement of the interfaces between absorber layer and the charge selective contacts and the establishing of electrical pathways.

After approximately 16 minutes, no more changes are observed in either one of the measurement parameters, which defines the final stage (iv) in the proposed model. Hence, it can be concluded that this initial crystallization during the dipping phase in

the two-step formation process is complete. This finding suggests that the dipping time can be shortened significantly in future cell manufacturing.

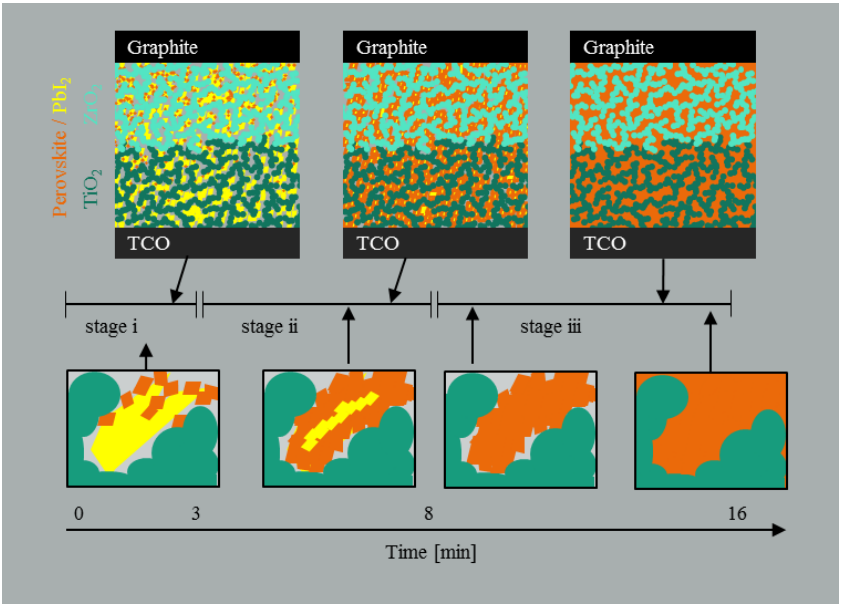

Figure 4.9 Proposed model of the crystal formation during the dipping phase. Starting with nucleation at the PbI_2 surface in stage (i), the crystallization is assumed complete after stage (ii) with consequent improvement of the absorber/contact interface in stage (iii).

4.1.5 Conclusion

Closing the gap between crystallization and the photovoltaic performance, a novel in situ characterization of optoelectronic properties and the electrical solar cell parameters during perovskite crystal formation in complete graphite-based monolithic perovskite solar cells is presented. The correlation is drawn between the optoelectronic properties, probed by PL measurements, and the electrical performance, probed by EQE measurements at a fixed wavelength of 700 nm. The introduced measurement procedure exploited the exceptional cell architecture of a graphite-based perovskite solar cell where both electrical contacts are established prior to the formation of the cell's absorber. The technique was demonstrated on the two-step conversion process of PbI_2 to $MAPbI_3$ within a mesoporous scaffold consisting of TiO_2 and ZrO_2.

Hitherto, the majority of in situ analyses of the crystallization process of $MAPbI_3$ perovskite, both of one and two-step deposition routes, were restricted to comparing the cell performance at intermediate stages of the crystallization. Reports of in situ measurements of the current-voltage characteristic and X-ray diffraction were published after this study [182]. Their protocol varies significantly from the one used in this case as they investigated IBC cell structure and a one-step process during the thermal annealing.

Enabled by the introduced technique, a prior unknown stage in the perovskite formation within a mesoporous scaffold was detected. After the crystallization process is judged to be complete, as suggested by stabilized PL emission properties, the EQE rises significantly. Therefore, efficient charge extraction is enabled by the establishment of electrical pathways at the interface between the perovskite absorber and the charge selective contacts.

This techniques provides access to the crystallization dynamics and photovoltaic performance, hence it is a valuable tool towards finding optimized processing parameters and eventually fostering the solar cell efficiency.

5 Impact of Heterogeneities

Leading questions in this chapter are which heterogeneities, chemical and/or structural, correlate to local variations in optoelectronic properties? How do heterogeneities affect the cell performance with increasing cell area? Can we find both benign and detrimental defects and how can we distinguish those and how we can control their relative occurrence?

To date, lateral heterogeneities in perovskite materials and solar cells have been observed on multiple length scales ranging from few nanometers to centimeter scale [44–59, 149, 225–227]. On the one hand, there are material intrinsic properties such as grain boundaries [57, 59], grain to grain variation [44, 48, 219] or anomalous morphologies [16, 46]; on the other hand a large number of process-related irregularities such as comet shapes in spin coted layers are commonly observed [51, 52, 56, 219, 228]. Regarding modules and tandem devices, heterogeneities can occur in and vary between the different (sub-) cells [52, 226]. Despite multiple observations of non-uniformities, a conclusive correlation between local chemical or structural variations and macroscopic properties is still lacking. In this chapter, the merit of spatially resolved analyses of perovskite absorbers from single crystals to complete devices is demonstrated with regard to the generation of in-depth understanding of material and cell parameters as well as the quality assessment of the variety of materials and fabrication processes, ultimately fostering the final photovoltaic device performance.

Throughout this thesis, multiple technological processes were supported by spatially resolved characterization performed by the author, which lead to joint publications. A brief overview is given:

In the development of a low temperature process for a combination of compact and mesoporous TiO_2 layer as electron transport layer, the homogeneity of PL emission and charge carrier extraction efficiency was analyzed by means of PL spectroscopy and LBIC mapping and compared to the standard-reference process [228]. The necessity of an alternative to the established sintering process at temperatures $> 450°C$ is owed to the desire for compatibility to the incorporation into monolithic tandem devices on silicon heterojunction solar cell substrates, since these cells require a process temperature limit of $200°C$.

Similar analyses supported the development of hybrid deposition route for the perovskite absorber, a combination of evaporated PbI_2 and spin coated MAI. Here, the particular interest was in the lateral distribution of the bandgap, assessed by the PL peak position. The optimization of process parameters was accompanied by spatially

and time resolved PL analyses, the latter yielding favorable recombination parameter for an optimized spin speed, eventually resulting in a device efficiency of > 18 % [229].

Since PSCs are prone to degradation upon light, moisture and oxygen exposure, understanding the underlying mechanisms is crucial for the development of stable devices. An investigation over 1000 hours of isolated UV exposure was conducted and the degradation as well as temporary recovery upon full-spectrum illumination analyzed. This recovery effect was attributed to partly beneficial effect of decomposition products of the perovskite absorber. The strong non-uniformity of the degradation across the cells was tracked via PL and LBIC mapping during multiple breaks in the UV exposure suggesting that the initial degradation mechanism is not related to the perovskite absorber but rather the interfaces to the hole and electron contacts [195].

This chapter is divided into two sections:

The first one presents work that was done in close collaboration with the Helmholtz-Center Berlin. Steffen Braunger from the Helmholtz-Center Berlin assessed the influence of process parameters on the formation of wrinkled textures and the corresponding solar cell characteristics, global PL measurements were performed by Christian Wolff from the University of Potsdam. The author was in charge of all spatially resolved analysis of the morphology and its optoelectronic properties, including micro-PLS mapping, SEM and EDX analyses.

The second section presents a comprehensive study, which was planned, conducted and analyzed by the author. For this study, samples were provided by Markus Kohlstädt from the Fraunhofer Institute for Solar Energy Systems.

5.1 Influence of Perovskite Morphology

In high-efficiency PSCs, the current state of the art absorber composition is a triple cation, mixed halide alloy. As introduced in Section 2.5.3, the incorporation of FA and Cs leads to a more suitable Goldschmidt tolerance factor and consequently to an increased intrinsic phase stability. Balancing the Br/I ratio as well as the FA/Cs ratio allows to fine-tune the bandgap, which is crucial especially for tandem applications. These alloys have been successfully employed in perovskite silicon and all-perovskite tandem solar cells in the recent past [13, 15–18, 157, 159, 160, 162]. Amongst these compositions, $Cs_{0.17}FA_{0.83}Pb(I_{0.83}Br_{0.17})_3$ perovskites with a 1.63 eV bandgap have been employed in the highest efficient monolithic perovskite/silicon tandem solar cells at the time of the study [16].

For these and related $MA_xFA_{(1-x)}Pb(I_yBr_{(1-y)})_3$ compositions, unusual, highly ordered microscopic textures have been observed by several groups [8, 16, 230, 231]. While the origin of this microstructure is subject of current discussion [231, 232], the potentially beneficial effect on light scattering and enhanced light in-coupling of micro- and nanostructures in thin films recently received great interest for this can improve the short-circuit current. This has been widely demonstrated for textured silicon [233–240] as well as in PSCs [241, 242]. Yet, the uniform deposition of thin charge selective contacts on textured films is challenging particularly for solution processes, and often results in performance loss from shunts and poor charge extraction [16]. As found in the presented study, the film morphology significantly affects the solar cell performance [44, 241, 243–245].

One major goal of the study of these microscopically patterned films therefore is to determine the influence of precursor composition and process parameters on the formation of microstructures (which in the following will be referred to as “wrinkled” structure, adapting the expression from [231]), hence, revealing the origin of the wrinkles. The second goal is to assess the influence of the morphology with regard to the photovoltaic performance and to determine the microscopic cause for the variation in solar cell characteristics. For this part, a high-resolution analysis of the local morphology is indispensable.

In order to achieve the first goal, alloys with varying cation and halide ratio were studied for their influence on the formation and distinctness of textured morphologies. For the investigation of the impact on solar cell performance of wrinkled textures, one fixed perovskite composition was chosen for its relevance to high-efficiency PSCs and its application in tandem devices [16]. Via manipulating the deposition and crystallization process, flat and wrinkled perovskite films were deliberately generated from the same precursor composition. Devices were made from the different films and their photovoltaic performance with regard to short-circuit current, open-circuit voltage, fill factor and overall efficiency compared. The discrepancy between the solar cells characteristics for the different absorber morphologies was accounted for by analyzing quantum efficiency and absorption spectra, global PL spectroscopy and transient PL was well as high-resolution PL spectroscopy mapping with direct comparison to SEM images.

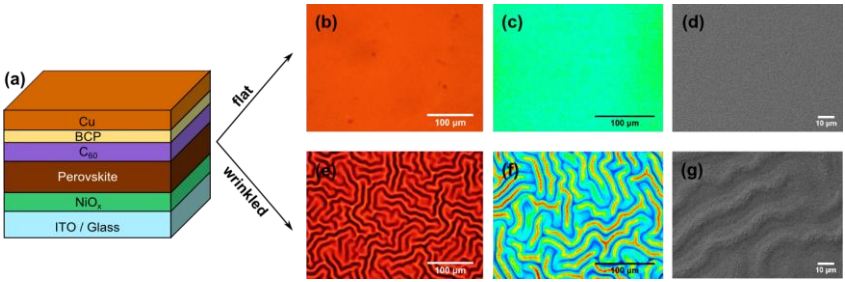

Figure 5.1 Schematic layer stack of the PSC used in this study (a). Images of flat and wrinkled $Cs_{0.17}FA_{0.83}Pb(I_{0.83}Br_{0.17})_3$ perovskite layers deposited under two different conditions (P1 and P2): Optical microscope images in transmission mode (b, e), confocal microscope images (c, f), and SEM images of perovskite layers (d, g) [46][15].

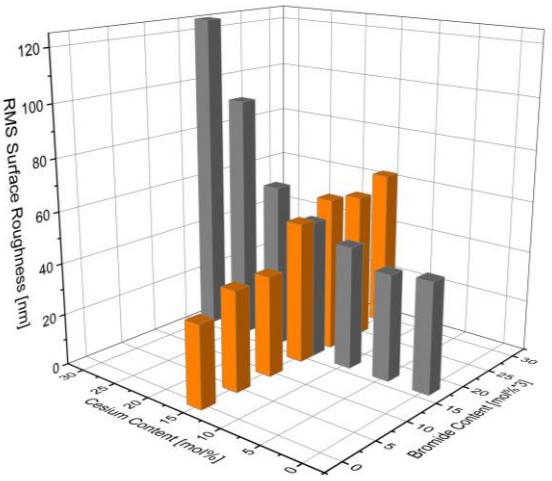

Figure 5.2 Surface roughness of perovskite films as a function of bromide and cesium content [46][15].

[15] Reprinted with permission from The Journal of Physical Chemistry C, "*$Cs_xFA_{1-x}Pb(I_{1-y}Br_y)_3$ Perovskite Compositions: the Appearance of Wrinkled Morphology and its Impact on Solar Cell Performance*", S. Braunger, L.E. Mundt, C.M. Wolff, M. Mews, C. Rehermann, M. Jošt, A. Tejada, D. Eisenhauer, C. Becker, J.A. Guerra, E. Unger, L.Korte, D. Neher, M.C. Schubert, B. Rech, S.Albrecht, Copyright 2018 American Chemical Society.

5.1.1 Influence of Processing Parameter

A thorough analysis of the influence of the perovskite precursor composition on the formation of wrinkled pattern in the absorber layer was conducted within this study. Details about the processing and the materials can be found in the appendix (7.1.1) and the corresponding journal publication [46]. The main findings are that wrinkles developed only if both two cations (Cs and FA) and two anions (I and Br) were present in the perovskite, the combination of Cs and Br in $FAPbI_3$-based perovskite appear to induce the formation of wrinkled structures. Both high content of Br and Cs favor the formation of wrinkles as can be seen in Figure 5.2 where the surface roughness is plotted as a function of Br and Cs content (obtained from atomic force microscopy (AFM) measurements on areas larger than the length scale of the wrinkles). It is striking that especially the Cs content causes a dramatic increase in surface roughness, which indicates the presence of wrinkles. Since one major application for $Cs_xFA_{1-x}Pb(I_{1-y}Br_y)_3$ alloys is incorporation in tandem solar cells, this finding is particularly relevant as higher bandgaps are currently acquired with high Cs and Br ratio.

However, even with a fixed composition, process routes could be found to suppress or allow the formation of wrinkles. $Cs_{0.17}FA_{0.83}Pb(I_{0.83}Br_{0.17})_3$ was chosen as base composition within this study of the solar cell characteristics and optoelectronic properties because of its successful application in high-efficiency perovskite silicon tandem solar cells. Whilst the perovskite composition is unaltered, the main difference between the two processing routes is the solvent atmosphere during the film formation: P1 is characterized by a solvent-poor atmosphere (open spin coater lid) and quick acceleration (4000 rpm, ramp 1 s), which resulted in the flat morphology. P2 generates the wrinkled structure via a solvent-rich atmosphere (closed spin coater lid) and slow acceleration (two-step, 1000 rpm, then 6000 rpm). Microscopic images of the corresponding films are depicted in Figure 5.1.

For the detailed microscopic analysis, a third category was investigated: more heavily pronounced wrinkles with regard to their height and width were formed for a higher precursor concentration compared to P1 and P2. The spin coating and annealing conditions are identical to P2. This process will in the following be referred to as P3. More details regarding the processing are given in Section 7.1.1.

5.1.2 Solar Cell Characteristics

In order to evaluate the impact of the microscopic structure on cell efficiency, the different perovskite morphologies were employed in p-i-n solar cells:

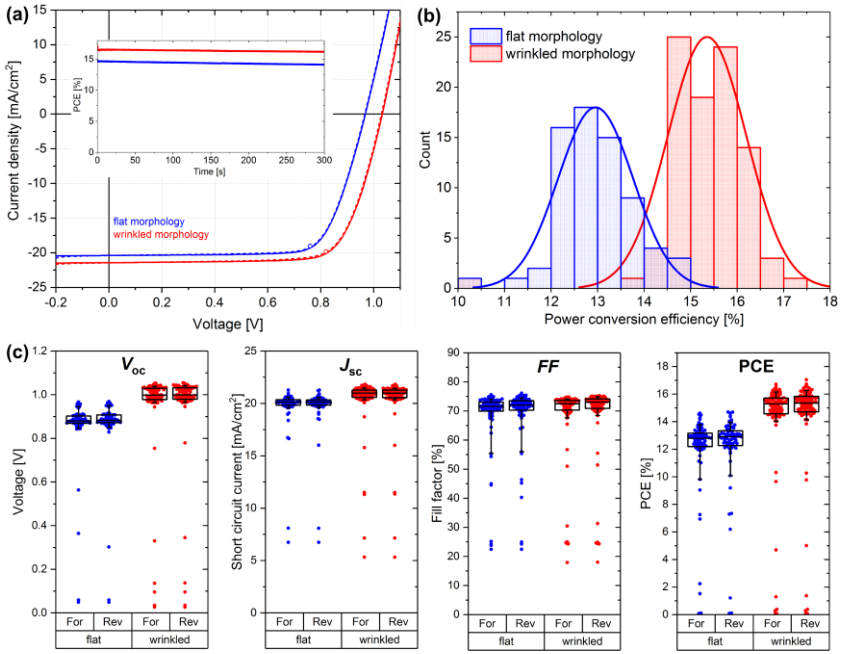

Figure 5.3 J-V characteristics of the champion devices in forward (dashed lines) and backward (solid lines) scan direction. Open circles in the respective color mark the MPP after 60 *s* of MPP tracking measurements (see inset) (b). Histogram of the PCE of devices with flat and wrinkled perovskite morphology obtained from J-V measurements in reverse scan direction. Solid lines represent Gaussian fits of the respectively colored data (a). Statistical analysis of photovoltaic parameters from J-V measurements, boxes show range of 25– 75% probability with median line, whiskers represent range of 10– 90% probability (c). For all graphs, red colored data represents results for the winkled morphology while blue corresponds to the flat morphology [46] [15]. .

The planar inverted cell architecture (schematic device structure in Figure 5.1 a, also cf. 2.7.3) was chosen for its eligibility in monolithic tandem solar cells [13, 15–18, 159]. Additionally, planar cells in both n-i-p and the p-i-n structure tend to show less pronounced hysteresis [123, 246–250]. Important for a fair comparison between the different surface topographies is a conformally grown electron contact, to avoid the rough wrinkled surface causing shunt pathways through it. Here, a thermally evaporated layer stack of fullerene-C_{60} (25 nm), bathocuproine (BCP) (6 nm), and Cu (100 nm) forms the electron contact on top of the perovskite absorber. The hole

contact consists of an approximately 15 nm thin layer of NiO_x deposited by the sol-gel method following the approach from You et al [251].

Within this section, two types of perovskite morphology will be compared: flat and moderately wrinkled films (corresponding to a root mean square (RMS) roughness of 250 nm) obtained by processing route P1 or P2, respectively, as described in the fabrication section (cf. Section 7.1.1). The summary of the electrical characterization of multiple batches of solar cells for both morphologies is given in Figure 5.3. Throughout the experiment, 76 cells featuring a flat and 99 cells featuring a moderately wrinkled morphology were analyzed. The statistical distribution in Figure 5.3 b, together with a Gaussian fit, clearly demonstrates the superior PV performance of cells with the wrinkled perovskite layer. The blue columns and line correspond to the flat morphology and show an average efficiency around 13%, the red columns represent the wrinkled morphology and surpass the flat counterpart's mean efficiency by almost $3\%_{abs}$. Breaking the results down to open-circuit voltage, short-circuit current and fill factor as shown in Figure 5.3 a, the superiority is majorly due to higher open-circuit voltages. Comparing the median average, the voltage increases from 0.88 to 1.00 V from flat (blue) to wrinkled (red) morphology. Smaller contributions come from the short-circuit current, rising from 20.1 to 21.0 mA/cm², and the fill factor, slightly enhanced from 71.7 to 72.8 %. The current-voltage characteristics (obtained under $1000\ W/m^2$, AM1.5g illumination, -0.2 to 1.2 V scan range, 0.2 V/s scan speed) of the champion devices are shown in Figure 5.3 c. The graph shows forward as well as reverse scan, yet no noticeable hysteresis is observed. For scan rates between 10 mV/s and 10 V/s, both device types displayed negligible hysteresis and stabilized power outputs very close to the respective J-V scans, as can be seen by maximum power point (MPP) tracking over five minutes (inset in Figure 5.3 c).

EQE spectra of multiple cells of both morphology types are shown in Figure 5.4. Averaging over 5 devices each, the integrated J_{sc} yields $20.2 \pm 0.3\ mA/cm^2$ for flat perovskite layers and a slightly higher value of $21.1 \pm 0.1\ mA/cm^2$. Considering the difference in layer thickness as can be seen in the SEM images of the film's cross section in Figure 5.6 -Figure 5.8. Thus, it is reasonable that the higher J_{sc} for the wrinkled solar cells can be attributed to higher absorption in the perovskite films. Comparing EQE spectra and corresponding absorption spectra in Figure 5.4, it can be seen that the increase in EQE for the wrinkled morphology is directly related to higher absorption in the long wavelength range > 500 nm up to the respective band edge. The absorbance was calculated from reflection and transmission spectra recorded on flat

and wrinkled perovskite layers on ITO-coated glass. Hence, the higher current is a purely optical feature of higher absorption. Calculating the attainable photocurrent yields an average enhancement of the J_{sc} by approximately 1 mA/cm^2, which is well reflected in the J-V results.

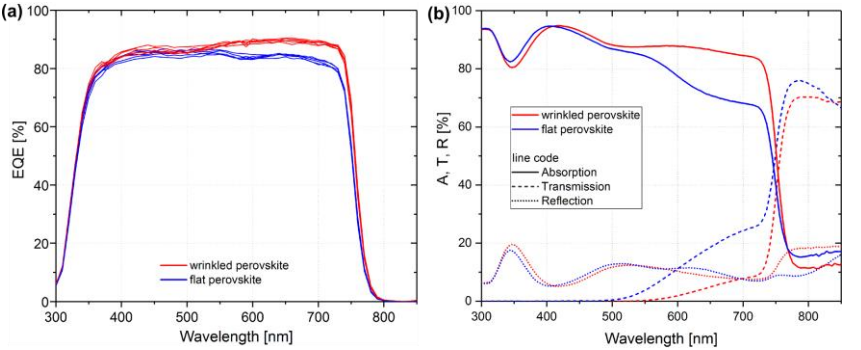

Figure 5.4 EQE spectra of solar cells with flat (5 devices, average integrated $J_{sc} = 20.2 \pm 0.3\ mA/cm^2$) and wrinkled (5 devices, average integrated $J_{sc} = 21.1 \pm 0.1\ mA/cm^2$) perovskite morphology (a). UV/vis/NIR absorption, transmission and reflection spectra of perovskite layers with flat and wrinkled morphology (b). Red curves correspond to wrinkled, blue to flat morphology [46] [15]. Samples with flat morphology were processed via P1, sample with wrinkled morphology via process P2.

The most significant impact on the overall efficiency, however, is due to the higher V_{oc}: on average, cells with wrinkled perovskite layer yield 100 mV more than comparable cells with flat absorber layer. Reduced recombination in either one of the interfaces or the perovskite bulk can cause a discrepancy in V_{oc}. Recently, it was shown that inserting insulating layers in between the perovskite and fullerene-C_{60} enables a much higher open-circuit voltage due to suppression of non-radiative recombination at the interface. However, the voltage here appears to be mainly limited from the NiO_x/perovskite interface [30]. Typical voltages with organic p-type polymer such as PTAA as the hole transport layer enabled open-circuit voltages above 1.1 V [30]. Changes in valence band energy at the NiO_x/perovskite interface have been reported for differently synthesized NiO_x [252–254]or surface modified NiO_x [255, 256], therefore the exact band alignment and surface recombination at this interface might affect the V_{oc} enhancement for the wrinkled over the flat films here.

5.1.3 Global Photoluminescence Analysis

The change in optoelectronic properties were analyzed with regard to the voltage change. In a first step, transient and static PL measurements were performed on a global level, characterized by averaging over the entire illumination area of 100 μm^2.

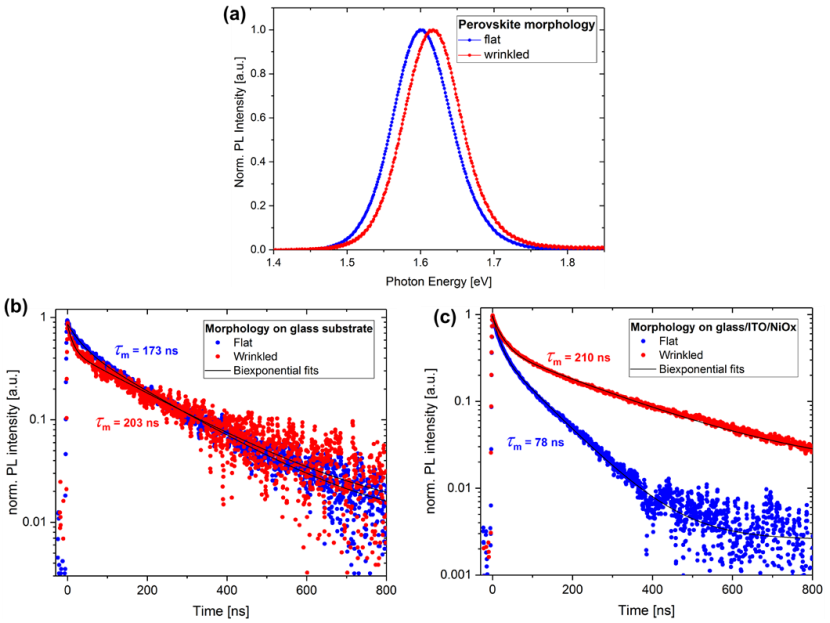

Figure 5.5 Global PL measurements of flat (blue) and wrinkled (red) perovskite films. Normalized PL spectra (a), transient PL measurements of perovskite films on glass (b) and glass/ITO/NiO_x substrates (c) at an excitation flux of 330 nJ/cm^2 [46] [15].

Global PL measurements were performed on encapsulated perovskite layers deposited on soda lime glass substrate or ITO-coated glass substrate with NiO_x layer. For the excitation, a 455 nm cw-laser and a 470 nm pulsed laser was used for the static and transient PL measurements, respectively. The excitation intensity for the transient PL measurements was 330 nJ/cm^2. Further experimental details can be found in the corresponding journal publication [46].

In Figure 5.5 a, the steady-state PL spectra are depicted for both morphologies, revealing a blue shift in the peak photon energy by 2 meV comparing flat (blue) and wrinkled (red) films, indicating a slight difference in the bandgap. A more detailed analysis of the absorption edge by variable angle ellipsometry in a related study

revealed slightly higher Urbach energies for flat $Cs_xFA_{1-x}Pb(I_{1-y}Br_y)_3$ perovskite layers indicative of somewhat higher lattice disorder [257].

A difference in recombination kinetics can be found from transient PL measurements: Whereas the transient PL do not deviate for the flat and wrinkled films on glass (cf. Figure 5.5 b), the influence of the interface recombination becomes evident when the NiO_x HTL layer is included in the film stack. While the PL decay for the wrinkled perovskite is negligibly influenced, the trPL signal decays significantly faster for the flat perovskite (cf. Figure 5.5 c), indicating a large contribution of surface recombination as it has been reported before [258, 259]. The influence of detrimental interface recombination is therefore at least partly accountable for the limited open-circuit voltage of cells with flat absorber layer.

5.1.4 Microscopic Analysis

In order to investigate the influence of the morphology on a microscopic scale, samples with varying levels of wrinkling were mapped using high-resolution PLS and SEM. The PL was mapped by the fiber-coupled confocal setup introduced in Section 3.1.2. For maximum resolution, the excitation beam at 635 nm was focused to 1 μm^2 spot size using a high NA lens (0.9) and a $\emptyset$ 25 µm pinhole. SEM images of both top view and cross section yield information about the crystal size distribution in the films as well as the film thickness depending on the location relative to the wrinkled pattern. Carefully choosing and marking the location of the SEM images, enabled mapping the PL in the identical regions for the wrinkled films, as the distinct pattern allows orientation within the film. Thus, it was possible to overlay SEM images and spectral properties of the emitted PL such as the photon energy of the peak position, enabling a direct and unambiguous correlation between optoelectronic properties and the corresponding morphology.

The main focus of the comparative analysis in the overall study lies on the comparison between flat and moderate wrinkled films obtained from process route P1 and P2, which correspond to the solar cell data shown in the previous section. For the purpose of facilitating the detection of lateral heterogeneities, their correlation and impact, a third category of test samples with highly pronounced wrinkles were produced with shorter spin time and higher precursor solution concentration (P3). A layer of polymethylmethacrylat (PMMA) was deposited on top of all samples for microscopic analysis. For all three cases, SEM images show the film thickness and crystal size distribution. In the case of an existing wrinkle pattern, the superposition of SEM image and PL peak photon energy is given alongside pristine maps of the PL spectral properties.

Starting with the flat perovskite structure, it can be seen from the SEM images in Figure 5.6 a,b and c that the film yields a uniform distribution of small apparent grains in the range of $50 - 400$ nm and a film thickness of $290 - 380$ nm, with a determined mean surface roughness (RMS) of 43 nm. The spectral distribution of the photon energy is uniform over the analyzed area (cf. Figure 5.6 d), the latter being around 1.66 eV.

The second sample type corresponds to process P2 (cf. Figure 5.7) and is superior in its photovoltaic performance compared to the flat structure, as described in the previous section. Highly ordered patterns are visible in the SEM images, areas of elevated layer thickness appear, following equidistant lines. The distance between two wrinkles is in the order of 20 µm, the film thickness ranges between 500 nm and 1500 nm, with RMS roughness of 250 nm.

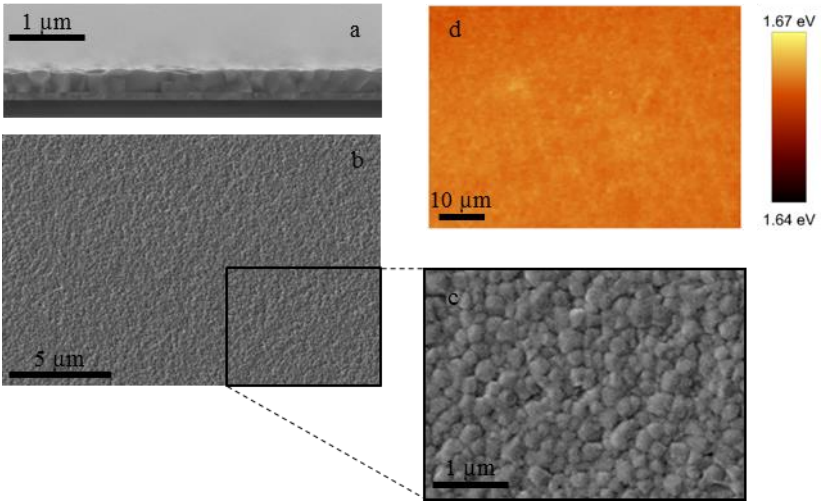

Figure 5.6 Cross section (a) and top view (b) SEM image with enlarged section (c). Photon energy of the emitted PL (d) for a flat perovskite structure following process route P1.

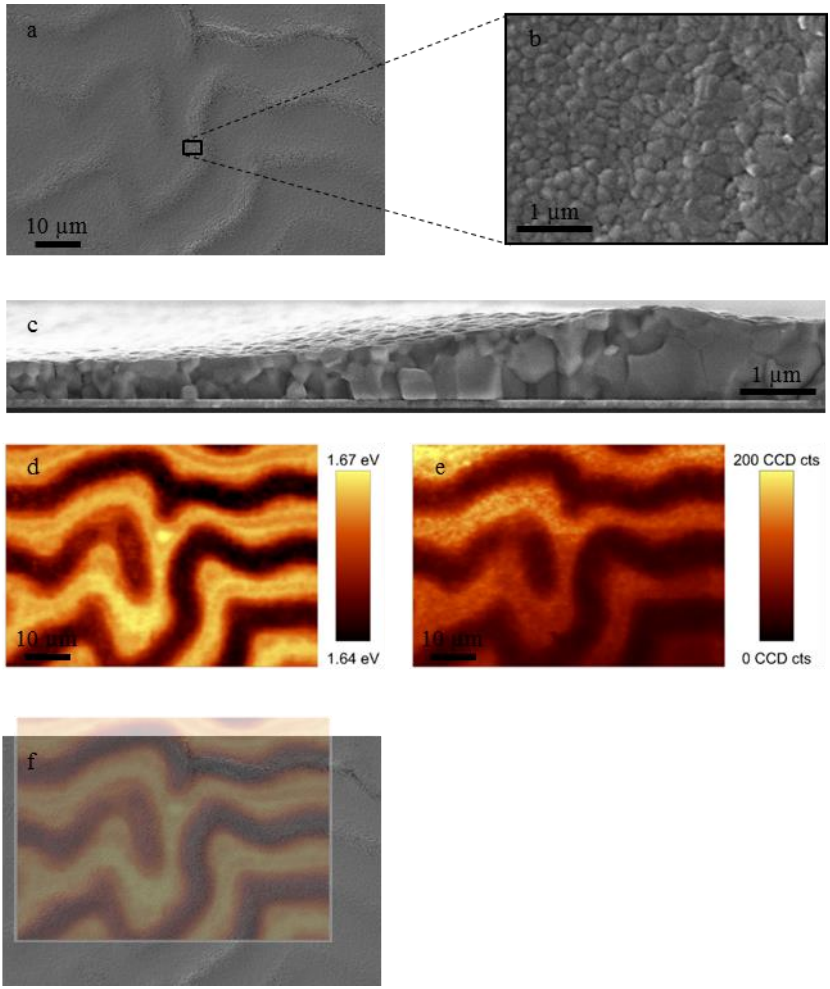

Figure 5.7 Top view (a) with enlarged area (b) and cross section (c) SEM image. Photon energy (d) and intensity (e) of the emitted PL for a moderate wrinkled perovskite structure, obtained from process route P2. Superposition of top view SEM and PL peak position (f).

Grain sizes are comparable to the ones found for the flat structure, with one systematic difference: areas of elevated thickness tend to feature larger crystals. Maps of the emitted PL reveal distinct variation in intensity and the spectral position of the PL peak, which unambiguously correlates to the wrinkle pattern. Whereas the measured PL intensity is likely to be influenced by the change of elevation, the spectral distribution will not be affected by this lack of exact optical focus. Confocal microscopy allows for the high resolution that is required for this detailed analysis of the microstructure, yet its small detection volume depends strongly on the chosen focal plane and is not capable of following the change in elevation within these small structures. Therefore, while a quantitative interpretation of the PL intensity has to be treated with keeping the influence of elevation variation in mind, the dependence of the photon energy of the emitted PL with the wrinkled pattern is undeniable. Interestingly, the peak energy in the flat regions is slightly higher than for the flat sample (1.67 eV). In the elevated areas, a distinct red shift by 3 meV compared to the neighboring flat regions can be observed, resulting in a photon energy of 1.64 eV.

The third category has not been included in the comparison of photovoltaic properties but yet will be used in this section, for it yields some insight in the correlation of optoelectronic properties with the perovskite morphology beyond the results for the moderately wrinkled structure (P2). The latter was chosen for the comparison due to its superior photovoltaic performance. In Figure 5.8, the results for a strongly pronounced structure are shown: both the cross section and the top view show systematically larger crystals in the elevated regions compared to the flat areas. Elevated areas reach layer thicknesses up to 3 µm including individual crystals with up to 3 µm in diameter, while the valleys are still comparable in thickness and crystal size to the flat film from process route P1. The distance between two elevated areas is in the same range as for the moderate wrinkled films.

Again, the direct correlation between morphology and PL emission properties can be observed. While the low regions between the wrinkles feature a photon energy of approximately 1.66 eV, the elevated areas display a distinct red shift of 3 meV, comparable to the red shift observed for the moderate wrinkled morphology. Taking a closer look at the ridge, individual crystal domains with slightly varying PL peak shift within this area can be perceived. The overall correlation between crystal size and PL peak shift is that larger crystals in the elevated areas show the red shifted PL emission compared to small crystals in the valleys. Three possible explanations will be discussed in the following: reabsorption, compositional variation and a deviation in lattice strain:

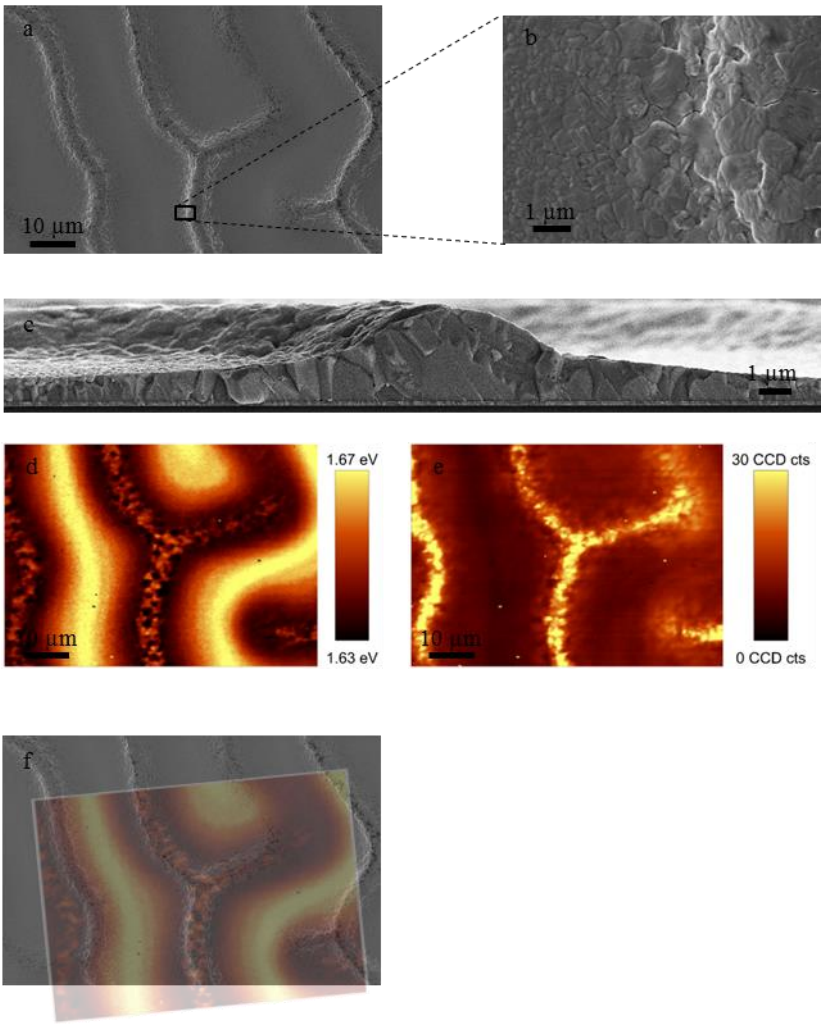

Figure 5.8 Top view (a) with enlarged area (b) and cross section (c) SEM image. Photon energy (d) and intensity (e) of the emitted PL for a heavily wrinkled perovskite structure, obtained from process route P3. Superposition of top view SEM and PL peak position (f).

Being influenced by reabsorption, the heterogeneous PL peak position could be merely a function of layer thickness. The probability of reabsorbing emitted PL radiation is higher for large film thicknesses as charge carriers can recombine radiatively at the far side of the film and the generated photon has to be transmitted through the film before it can escape, be collected and subsequently detected. Hence, with increasing travel distance, the chance of being reabsorbed in the lattice is rising simultaneously. As the absorption is a function of photon energy and decreases on approaching the band edge, high-energy photons are more likely reabsorbed, hence the PL spectrum would exhibit a red shift accompanied with a reduction in peak width [220, 260]. The latter has not been observed as the PL spectra in Figure 4.7 a show. Additional evidence against this theory was found in the early stages of the study of wrinkled perovskite films. Before optimizing the processing parameters, films with highly pronounced wrinkles were manufactured and analyzed. The main difference in processing was a different precursor concentration (1.1 M) and an excess of PbI_2 (110%), the spin coating and annealing procedure are comparable to P2 (cf. Section 7.1.1).

For these films, one very remarkable feature was found: in the upper left corner of Figure 5.9 is a flat region with large crystals. Looking at the PL peak position, this area shows the same red shift as the neighboring elevated areas. These flat areas with increased crystal size have not been observed for moderate wrinkled films, however the correlation between crystal size and photon energy of the emitted photoluminescence separated from the variation in layer thickness is another argument against the influence of reabsorption.

The second investigated explanation of the red shift would be a compositional variation across the film. Halide segregation is a possibility, if the bromide and iodide content varies with the morphology, this would result in a deviation in the crystal lattice and thus the bandgap [7, 8, 41]. To test this hypothesis, EDX measurements were performed on the films and their cross sections. The latter gave a more reliable result, as the beam damages the film and when probing thin layers from the top, the underlying substrate was eventually detected judging from its strong Indium signal originating from the ITO layer (cf. Figure 5.10). The results of the cross section probing is depicted in Figure 5.11: the point probes of the valley/elevated regions, respectively, gave no indication of a compositional variation. Hence, a homogeneous lateral distribution of the perovskite composition can be assumed and its influence on the inhomogeneous PL emission discarded.

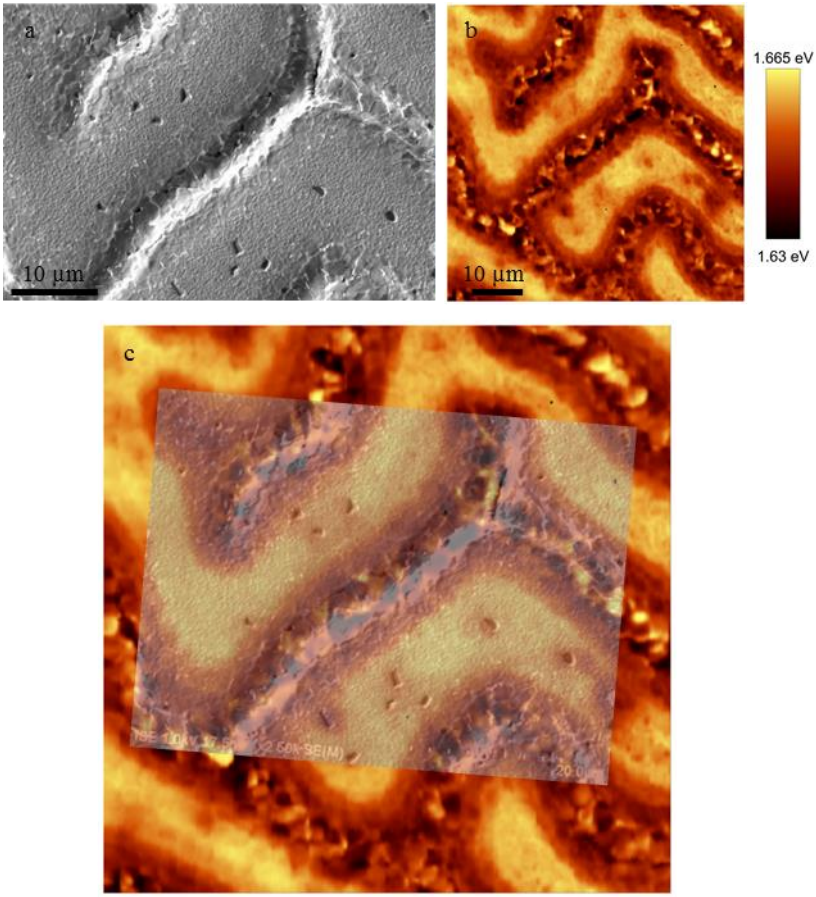

Figure 5.9 SEM image (a) and PL peak position map (b) and their superposition (c) for a heavily wrinkled perovskite layer as demonstration example for the correlation between crystal size and PL peak position independent from the film thickness.

The last and most likely accurate cause of the red shift towards the wrinkles is a difference in lattice strain across the substrate. As reported in literature, the PL peak position can be a function of crystal size [215–217, 219]. It has been observed both for films with changing average crystal size and for single crystals. Computational studies have proposed the correlation between lattice strain in the Pb-I bond and PL emission [84, 85], which is related to crystal size as confirmed by experimental studies including Raman spectroscopy and XRD [116, 216–218]. Only recently, Tsai et al. published a thorough study of the light-induced lattice expansion [81]. They rationalize that upon illumination with light of greater energy than the bandgap, generated electron hole pairs can weaken covalent bonds by occupying bonding states in the conduction band and vacating anti-bonding states in the valance band. This in turn can lead an increased Pb-I-Pb bond angle, hence causing a bandgap narrowing and consequently a red shift in the PL emission spectrum. They observe a $5\,\mathrm{meV}$ red shift within 2-3 hours of illumination ($100\,\mathrm{mW/cm^2}$) for the PL.

A comparable analysis of the temporal evolvement of the PL peak photon energy under continuous illumination for different local spots on the flat and wrinkled films is shown in Figure 5.12 b. Since the focused illumination in the confocal setup exceeds the standard $100\,\mathrm{mW/cm^2}$ conditions, an accelerated development can be expected.

While the PL peak position changes significantly by almost $3\,\mathrm{meV}$ for both the flat film and the valley regions in the wrinkled films over a time range of few minutes (filled symbols), the change for the elevated areas is negligible for the heavily pronounced (open green symbols) and only slightly noticeable for the moderate wrinkled areas (open red symbols). According to Tsai et al., the observations could be accounted for if the change in PL emission is correlated to a bandgap narrowing due to lattice relaxation upon illumination. The variation in average rate of change for the different locations is then most likely related to the initial strain in the lattice, which, as we can assume, is larger for the small crystals in the flat/valley regions. Additionally, as the weakening of the covalent bond appears to be dependent on the charge carrier density, it could be argued that this quantity is higher for the smaller volume in flat areas, assuming that a comparable amount of photons from the laser flux have been absorbed in comparison to the larger volume in the elevated areas.

The temporal evolvement also accounts for the difference in PL peak energy found for the global measurements compared to local values: while the PL maps represent the initial state, the globally obtained spectra already allowed for some strain relaxation in the lattice and therefore yield lower photon energies.

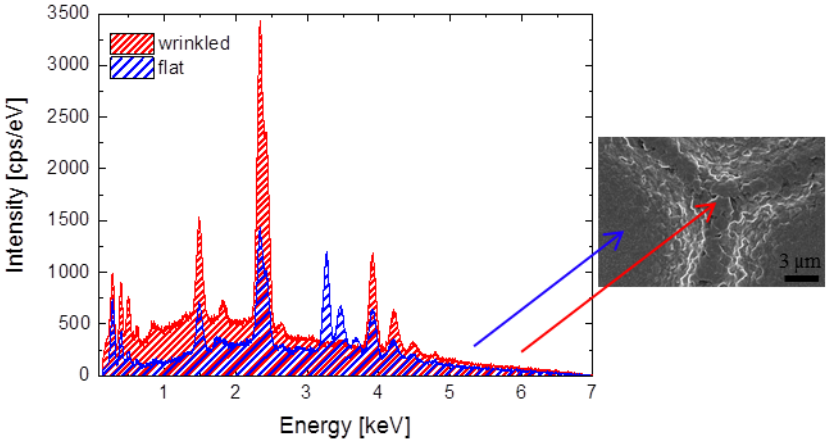

Figure 5.10 EDX results for top view probing of sample type P3 in an elevated and a valley area. The strong Indium signal for the valley measurement indicates damage in the absorber layer and an effective probing of the underlying ITO covered glass substrate.

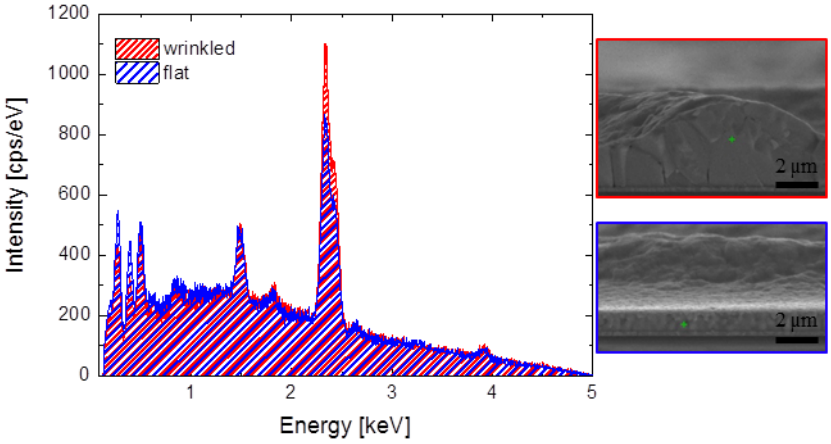

Figure 5.11 EDX results for cross sectional probing of sample type P3 in an elevated and a valley area. No indication for compositional changes in the different regions can be found.

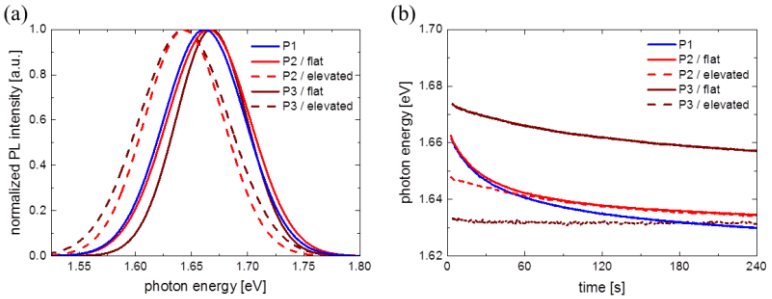

Figure 5.12 Initial local PL spectra obtained from the flat (blue), moderate wrinkled (red) and heavily wrinkled (green) perovskite layers, open symbols correspond to elevated areas, filled symbols correspond to flat regions (a). Time evolvement of the PL peak position for the different samples and spots under constant illumination over several minutes (b), color and symbol code are equivalent in both graphs.

5.1.5 Conclusion

In the beginning of the investigation, two major questions were leading the experiments: under which circumstances are wrinkled structures formed and in which manner do they influence the photovoltaic performance.

Compositions containing both Cs and Br, besides FA and I, were found to form a wrinkled morphology under various processing conditions, in particular, if a high content of Cs was present. Since both high Cs and high Br content appear to favor the formation of the wrinkled pattern, this phenomenon needs to be taken into account for the development of high-bandgap absorber materials for tandem application.

The comparative analysis of inverted, planar PSCs with either flat or moderately wrinkled absorber layer, showed superior performance of the wrinkled morphology both in short-circuit but even more pronounced in open-circuit voltage. While the higher current was accounted for by increased absorption in the thicker layer, the significant change in voltage appears to have various sources:

On the one hand, an unfavorable surface recombination at the NiO_x/perovskite interface could be concluded from the transient PL measurements with and without HTL present. On the other hand, the difference in crystal size and especially the inhomogeneous distribution of the PL peak position and its unambiguous correlation to the wrinkled structure, corroborated by superposing PL maps and SEM images,

indicates the influence of strain as reabsorption and compositional variation could be ruled out.

Overall the author proposes, based on the observations on $Cs_xFA_{1-x}Pb(I_{1-y}Br_y)_3$ film formation and the local optoelectronic properties, that wrinkles result from the release of compressive strain within the perovskite layer. Taking a close look at the spatial correlation between optoelectronic properties and the morphology demonstrated to be crucial in finding an answer the leading questions in the presented study. Hence, it confirmed once more that identifying and interpreting lateral heterogeneities is indispensable in understanding perovskites.

5.2 Quantitative Local Loss Analysis

In this chapter, approaches to quantify loss mechanisms across the complete solar cell are introduced. Spatially resolved maps of the open circuit voltage and the short circuit current are derived from DLIT and LBIC measurements. Consequently, the local efficiency will be estimated from these two maps. The techniques introduced in this chapter will be demonstrated on planar, inverted PSCs with blade coated absorber (cf. Figure 5.13). Being compatible with roll-to-roll processing, blade coating is a feasible technique for upscaling. This cell type was chosen because increasing the active cell area from few square millimeters to full wafer size while maintaining a reasonable efficiency level is a key challenge for PSCs. The scaling factor, efficiency as a function of cell area, is significantly lower than for other materials with similar lab scale efficiencies (Si, CdTe, CIGS) [29]. The main goal of the quantitative loss analysis is to determine the extent of the detrimental influence of non-uniformities with regard to the upscaling of PSCs.

The cells were processed by colleagues in Uli Würfel's group at the Freiburger Materialforschungszentrum (FMF). All measurements and analyses were performed by the author. The following chapter partly goes along the lines of the corresponding journal publication [261].

In the first section of this chapter the samples, used for the development and demonstration of the local loss analysis, are introduced. Subsequently, the application of DLIT and the local JV analysis to PSCs is discussed and maps of the open-circuit voltage are determined. In the next step the local short-circuit current is estimated based on LBIC and corresponding EQE measurements. Finally, efficiency maps are calculated and different loss mechanisms are discussed.

5.2.1 Blade Coated Perovskite Solar Cells

The main difference compared to standard PSC processing techniques is the deposition of the absorber material. The perovskite precursor, a 3M solution of lead(II) acetate trihydrate and MAI in DMF, is blade casted on top of the HTL in nitrogen atmosphere instead of spin casting the solution. The cells used in this study were processed with a gap size of $50\,\mu m$ at a coating speed of $5\,mm/s$, the substrate was kept at a temperature of $40°C$ during the coating process. To complete the conversion of the precursor to $MAPbI_3$, the substrates were thermally annealed at $100°C$ for 30 minutes. The cell architecture is a planar inverted (p-i-n) structure as depicted in Figure 5.13: the functional layers were deposited on top of pre-patterned ITO substrates of $5 \times 5\,cm^2$. Two different cell types are investigated in this study, featuring different hole contact materials: either a $35\,nm$ thick layer of PEDOT:PSS or NiO_x serve as

HTL. In case of PEDOT:PSS, the layer was deposited by spin coating, followed by a temperature treatment at 130°C in dry nitrogen atmosphere. The NiO_x was sputter deposited and thermally annealed in air at 300°C for one hour. The electron contact is identical for both cell types and consists of a combination of PCBM and AZO. First, a PCBM solution (10 mg/mL in $CHCl_3$) was spin cast followed by AZO nanoparticles. In a final step, the 100 nm aluminum back electrode was thermally evaporated. The back electrode defines the active cell area, a $22 \times 5\ mm^2$ rectangle. More details about the blade coated PSCs can be found in the publication by Kohlstädt et al. [262].

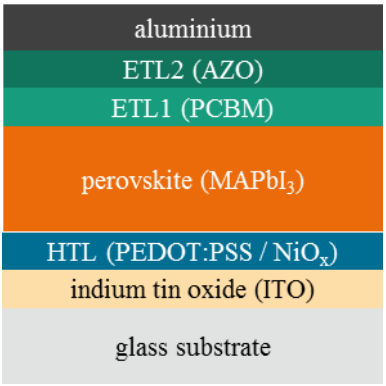

Figure 5.13 Schematic structure of inverted planar PSC. HTL and ETL denote electron and hole transport layers, respectively.

The development of the methods and the conclusive loss analysis will be demonstrated by comparing two blade coated PSCs. In the following section, the samples are introduced by discussing their global J-V parameter:

The chosen samples represent a non-optimized cell process from early experiments and a well working sample representing the improved process. Besides the optimization of the drying process subsequent to the blade coating [262], one major difference between the two samples is the hole transport layer, PEDOT:PSS or NiO_x, respectively, resulting in a significant difference in the open-circuit voltage. This is partly due to the interface between PEDOT:PSS and perovskite, which has been shown to limit the open-circuit voltage and thus performance of PSCs by increased interface recombination [18]. A summary of the investigated cells' parameters is given in Table 5.1.

Table 5.1 Summary of cell parameters for both forward and reverse scan direction for one representative cell of each HTL sample.

HTL	Sweep	J_{sc} [mA/cm²]	V_{oc} [V]	FF	η [%]
PEDOT:PSS	forward	15.1	0.877	0.66	8.67
	reverse	14.9	0.876	0.71	9.25
NiO_x	forward	17.8	1.07	0.63	11.9
	reverse	18.0	1.07	0.61	11.7

Global J-V curves were measured in dark and illuminated conditions in both scan directions with a scan rate of 185 mV/s: from -0.1 V to 1.2 V (forward) and subsequently from 1.2 V to -0.1 V (reverse). Illumination intensity was calibrated using a silicon reference cell and is equivalent to $1000\ W/m^2$, AM1.5g.

Comparison of forward and reverse scan directions reveal minor hysteresis effects (cf. Figure 5.14), even less for the well working device with NiO_x as HTL. While this cell shows an overall superior performance, mainly due to the higher open-circuit voltage, its fill factor is lower compared to the non-optimized sample. On small scale, having an active area of $0.0925\ cm^2$, devices with the presented architecture but a spin-coated absorber layer yield a conversion efficiency of up to 16.8 % , when NiO_x is employed as HTL [262]. The samples investigated in this work have an active area of $1.1\ cm^2$, and show conversion efficiencies approaching 12% (cf. Table 5.1).

Looking at the current-voltage characteristics under dark conditions in Figure 5.15, we observe significant dark current for voltages below 0.8 V for the PEDOT:PSS cell, which indicates insufficient shunt resistivity and/or increased recombination. For voltages approaching 1.0 V the bending of the dark J-V curves reveals limitations due to a high series resistance. The cell features a global shunt resistance of approximately $2\ k\Omega\ cm^2$ and a series resistance of approximately $2\ \Omega\ cm^2$. The dark current for the NiO_x cell is almost one order of magnitude lower than for the PEDOT:PSS sample.

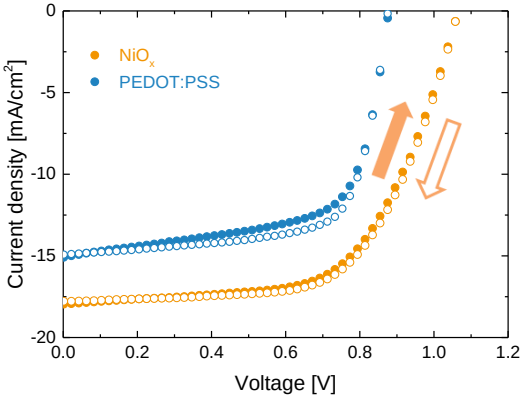

Figure 5.14 Illuminated current-voltage characteristics for two blade coated PSCs with NiOx (orange) and PEDOT:PSS (blue symbols) as HTL. Shown are both forward (filled symbols) and reverse (open symbols) scan directions.

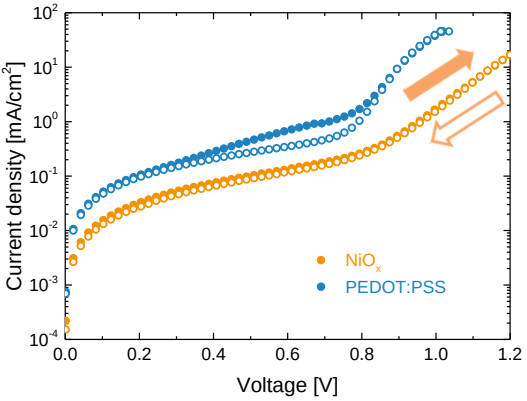

Figure 5.15 Dark current-voltage characteristics for two blade coated PSCs with NiOx (orange) and PEDOT:PSS (blue symbols) as HTL. Shown are both forward (filled symbols) and reverse (open symbols) scan directions.

5.2.2 V_{oc} Image from Local J-V

In this section, the derivation of open-circuit voltage maps from DLIT measurements is introduced. In a first step, the general applicability of DLIT to PSCs and specific considerations are evaluated. All spatially resolved results for the PEDOT:PSS/NiO_x cells from Table 5.1 will be discussed as demonstration of the characterization techniques, subsequent to their introduction.

5.2.2.1 Lock-In Thermography on Perovskite Solar Cells

The fundamentals of DLIT are introduced in Section 3.1.2.3. As this technique, initially developed for the investigation of silicon solar cells, has not been used for perovskite characterization before, it was at first necessary to evaluate assumptions about thermal thickness of PSCs as it directly influences the quantitative analysis of DLIT measurements.

Perovskites show a very low thermal conductivity compared to silicon, leading to a shorter thermal diffusion length:

The thermal conductivity of $MAPbI_3$ is $\lambda_{MAPbI_3} \approx 0.3 - 0.5 \frac{\mathrm{W}}{\mathrm{Km}}$ [263] ($\lambda_{Si} \approx 150 \frac{\mathrm{W}}{\mathrm{Km}}$), with the specific heat of $c_p \approx 190 \frac{\mathrm{J}}{\mathrm{Kmol}}$ and density $\rho \approx 4 \frac{\mathrm{g}}{\mathrm{mol}}$, this results in a thermal diffusion length as a function of the lock-in frequency:

$$\lambda_{MAPbI_3} = \sqrt{\frac{2\lambda_{th}}{c_p \rho \omega}} \approx 1.15\ \mathrm{mm}/\sqrt{\mathrm{s}} \times \frac{1}{\sqrt{f_{lock-in}}} \tag{5.1}$$

For a typical lock-in frequency of 30 Hz, this results in a diffusion length of $\Lambda_{MAPbI_3} \approx 200\ \mu\mathrm{m}$ which is in the same range as glass $\Lambda_{glass} \approx 330\ \mu\mathrm{m}$. For quantitative interpretation of the thermography signal, it is crucial to determine whether a PSC behaves as a thermally thick or thermally thin sample. In the case of a thermally thick system, the dissipated power is proportional to the S^{-45° image and for a thermally thin system, it is proportional to the S^{-90° image.

The perovskite absorber layer itself can be regarded as thermally thin, since the thermal diffusion length for lock-in frequencies between 10^{-1} Hz and 10^{2} Hz is approximately three orders of magnitude higher than the layer thickness $\Lambda_{MAPbI_3} \gg d_{MAPbI_3}$. Of the adjunct layers, the metal contact is the sole strong thermal conductor and yet its thickness is small compared to the thermal diffusion length. In a perovskite solar cell, the glass substrate features by far the largest layer thickness and therefore, for an accurate description, the thermal thickness of the substrate needs to be taken into account:

Whereas its thermal diffusion length is equally short as the perovskite's, it is around three orders of magnitudes lower than the layer thickness $\Lambda_{glass} \ll d_{glass}$, hence representing a thermally thick system.

According to the theoretical analysis of thermal wave propagation in thin films on substrates by Straube et al. [264],a system consisting of a thermally thin layer on a glass substrate can be described as thermally thick. However, due to the very low thermal conductivity of both the perovskite and the glass substrate, it can also be argued to view the system as thermally thin and an unambiguous assignment concerning the thermal thickness of a perovskite solar cell on a glass substrate cannot be given.

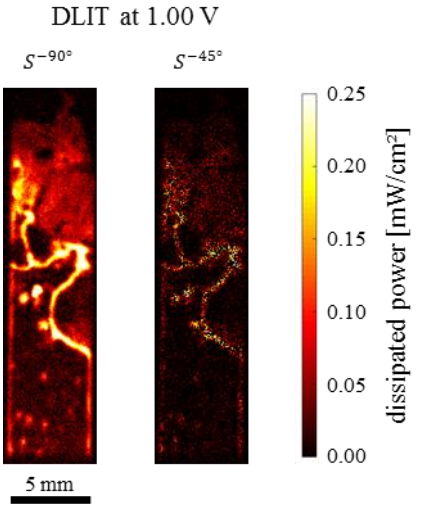

Figure 5.16 Comparison of the dissipated power images based on the evaluation of either the $S^{-90°}$(left image) or $S^{-45°}$(right image).

As the classification is not unequivocal, an evaluation of both the $S^{-45°}$ and $S^{-90°}$ image has been performed for comparison, the results for a blade coated PSC with PEDOT:PSS as HTL are shown in Figure 5.16. The $S^{-90°}$ image (left image) reveals the dissipated power at a bias voltage of 1 V significantly better with regard to the signal-to-noise-ratio. Therefore, the following analyses are based on the evaluation of the $S^{-90°}$ images, assuming proportionality to the dissipated power.

All thermography measurements on single junction PSCs were performed with the glass side facing the camera and the opaque back electrode facing the water-cooled

chuck. Lock-in thermography measurements through glass, comparable to measurements of encapsulated modules, are feasible for lock-in frequencies above 0.5 Hz [265].

5.2.2.2 Local J-V Analysis

The application of the local J-V analysis (cf. Section 3.3.2) is generally applicable to solar cells whose J-V characteristics do not deviate notably from a standard diode's curve. This is the case for most PSCs without pronounced hysteresis, which is a requirement for a reliable and comprehensive analysis. An explicit physical interpretation of the two-diode model's (cf. Section 2.3.2) parameters such as J_{01} and J_{02} is not conclusive for PSCs, yet this is also not the case for silicon solar cells and the analysis still yields valuable information. While it is widely acknowledged that J_{01} is a measure for the base recombination in classical pn-junction silicon solar cells, the physical interpretation of J_{02} is still highly controversial, the parameter was primarily necessary to enable eligible fitting of the J-V curves.

In PSCs, effects such as hysteresis, instability during the measurements and unknown injection dependence can influence the quality of the fit and therefore the conclusiveness of the analysis but will not fundamentally alter the measurement approach.

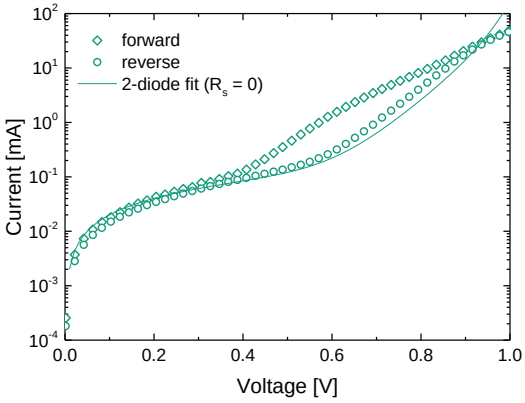

Figure 5.17 Dark current-voltage characteristics for a blade coated PSC with manually fitted J-V curve according to the two-diode model.

In Figure 5.17, an exemplary fit of the two-diode model to a dark J-V curve of a blade coated PSC is depicted. Whereas the negligence of the series resistance leads to a deviation for high injection conditions at bias voltages approaching 1 V, the curve describes the J-V data well. Hysteresis effects will fatally corrupt the analysis, if the modelling of the J-V curve significantly misinterprets the V_{oc}. Given that the hysteresis affects merely the voltage range around the maximum power point, as it is the case for the PEDOT:PSS cell (cf. Figure 5.14 and Figure 5.15), it will not substantially alter the result for the local voltage. The pseudo-fill factor depends stronger on the hysteresis, in the given global dark JV curves for the PEDOT:PSS cell, the deviation is $5\%_{abs}$. Cell stability throughout the measurement is essential to the analysis' outcome. The measurement time for a single DLIT measurement ranges between 20 and 60 minutes, depending on the signal intensity. Longer integration times will improve the signal-to-noise ratio.

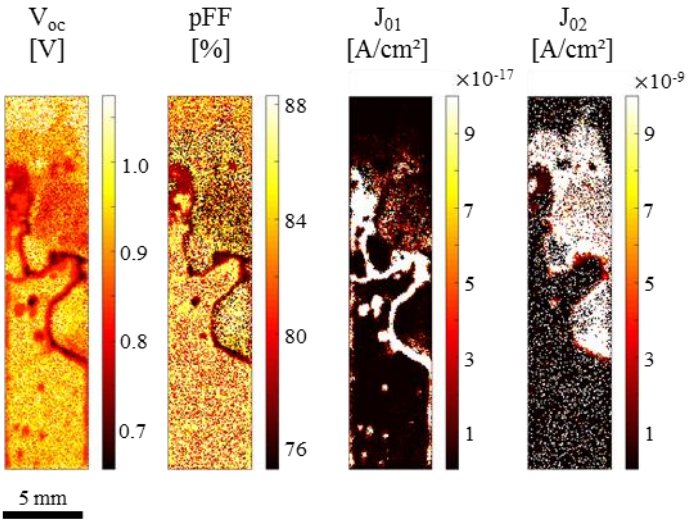

Figure 5.18 Results of local J-V analysis for blade coated PSC with locally injection-dependent dark current characteristics.

In the analysis proposed by Breitenstein, three images in forward bias direction are taken into account and additional one image in moderate reverse bias direction, yielding information about the shunt resistance. Unfortunately, the latter could not be accessed for the PSCs investigated within this thesis since the cells could not withstand even moderate reverse bias without suffering severe degradation. Hence, the analysis

was restricted to forward bias and no conclusive evidence can be given for the shunt resistance (or alternatively shunt conductance) represented by the parameter G_p. However, the influence of this parameter on the estimated efficiency distribution, which will be shown later on, is small provided that its value is relatively low and the J-V curve in the low bias range can be well described by the J_{02} contribution.

Employing the complete local J-V analysis based on multiple DLIT images, lateral heterogeneities can be revealed and their impact on the cell performance quantified. In Figure 5.18, an example for injection-dependent feature is presented. Although the dark current densities J_{01} and J_{02} do not necessarily yield definite interpretation, they represent the different regimes of low and high injection. While J_{01} describes the diode behavior at high bias voltages, the second diode represents the behavior for low bias voltages. The presented cells were located on one substrate for which the uniform deposition of the absorber layer was not successful and resulted in majorly pronounced drying lines of the layer. While the V_{oc} reflects both areas of increased dark current in voltage losses, the injection-dependence is solely revealed by the comparison of J_{01} and J_{02}.

5.2.3 J_{sc} Image from Light Beam-Induced Current Mapping

Microscopic LBIC mapping (cf. Section 3.2) is an appropriate probe for the cell homogeneity and due to its high resolution allow the attribution of features and defects to individual process steps. The charge collection probability, given by the LBIC signal, directly correlates to the cell performance. In order to estimate the local short-circuit current density, the LBIC distribution is scaled in order to match the globally determined short-circuit current. This is done by determining the arithmetic average of the LBIC map and setting it to the J_{sc} from the previous J-V measurement, which in the case of the PEDOT:PSS cell was $15.0\ \mathrm{mA/cm^2}$, the average between forward and reverse scan. For a more sophisticated approach, taking into account the spectral dependence, maps obtained by multiple excitation wavelengths are weighted according to their contributions to the cell's external quantum efficiency [266]. The calculation of the J_{sc} map in this case was performed via a weighted average based on the respective contribution in the overall external quantum efficiency (EQE).

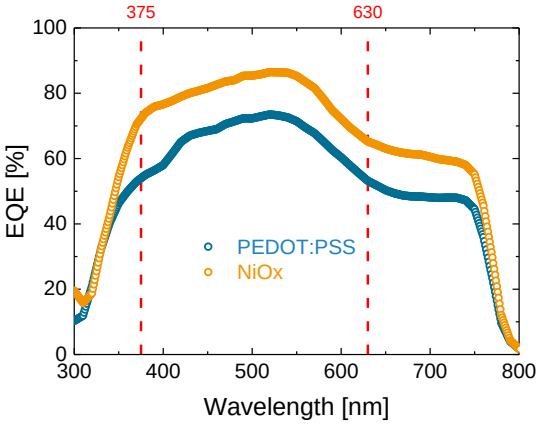

Figure 5.19 External quantum efficiency of spin-coated reference samples featuring the same architecture on a small cell area with a spin coated perovskite layer. The absolute height was calibrated to the blade coated cell's J_{sc} determined by light J-V measurements. Two lines at $375\,nm$ and $630\,nm$ indicate the splitting of the spectrum in a short, middle and long wavelength part.

The EQE was obtained on a comparable spin-coated reference cell featuring the identical cell architecture but a small cell area of 0.0925 cm². To get the weighting factors, the EQE was divided into three spectral ranges corresponding to the three excitation wavelengths, as depicted in Figure 5.19. The individual contributions to the overall short-circuit current density are as follows: $J_{sc}^{short} = 0.5\,\mathrm{mA/cm^2}$, $J_{sc}^{mid} = 11.5\,\mathrm{mA/cm^2}$, $J_{sc}^{long} = 6.0\,\mathrm{mA/cm^2}$. The spectral integration was performed within the limits as indicated in Figure 5.19. This estimation of the short-circuit current relies on the stability of the device performance during the time-consuming investigation. Severe degradation between the J-V measurements and the LBIC measurements can lead to overestimation of local current values. The deviation from global standard illumination conditions ($1000\,\mathrm{W/m^2}$, AM1.5g) can influence the validity of the estimation due to an incomplete comprehension of the injection dependence. Hence, spot size and illumination intensity were chosen with regard to minimize effects such as charge carrier diffusion from the excited region to dark areas.

LBIC and PL maps, as presented in the following section, were simultaneously obtained by a confocal microscopy setup described in Section 3.1.1. For optical excitation multiple wavelengths were used in continuous wave mode with a power

density in the range of 150 mW/cm^2, with an excitation spot size of approximately 20 µm FWHM. All measurements were conducted in ambient air at room temperature. The mapping started in the top left corner and ended in the bottom right corner, the scan direction was the same for all measurements. In case of the PEDOT:PSS cell only one excitation wavelength was used (635 nm) but in order to account for the wavelength dependency, LBIC maps were obtained at three different wavelengths for the NiO_x sample for an improved estimation of the cell's J_{sc} distribution.

5.2.4 Local Loss Analysis

In this section, all spatially resolved results are presented and discussed for their local features in relation to the processing procedure. Only by the combination of multiple spatially resolved characterization techniques such as PL spectroscopy mapping, LBIC and DLIT, a comprehensive analysis can be conducted, local loss mechanisms identified and related to the fabrication process.

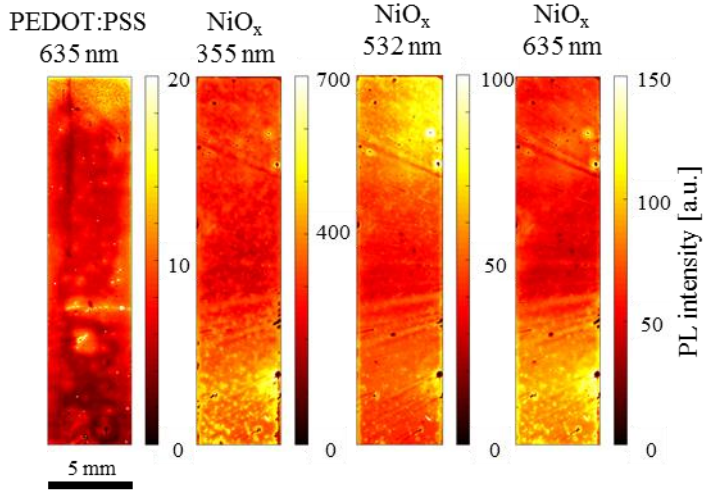

Figure 5.20 Results of the PL spectroscopy mapping for both cells, showing the PL intensity in arbitrary units. The NiO_x sample was analyzed using three different excitation wavelengths.

First, all mapping results are shown in Figure 5.20 – Figure 5.22. Due to the development of the technique in the early stage of the experiments which coincided with the early efforts to process blade coated PSCs, only one wavelength (635 nm)

was used for probing the samples. Due to a lack of long-term stability, it was not possible to conduct further measurements on this cell later on. For the PEDOT:PSS cell therefore only one LBIC map is used to estimate the local J_{sc}, whereas for the NiO_x cell LBIC maps obtained from measurements using three wavelengths support the J_{sc} estimation. Nevertheless, for the purpose of demonstrating the technique's value in improving the cell efficiency, the comparison of an early stage processed cell with a cell from the improved process was chosen.

The PL intensity, integrated in a spectral range of 1.56 eV to 1.68 eV, is shown in Figure 5.20 and the photon energy of the PL peak position in Figure 5.21, also indicating the coating direction. The LBIC maps are shown in Figure 5.22 and in case of the NiO_x cell, they reveal a different current distribution for the 532 nm map compared to the 355 nm and 635 nm maps. Both the LBIC map and the one of the integrated PL intensity reveal lateral inhomogeneities consistent with [6–9] (cf. Figure 5.20 and Figure 5.22). As discussed by Eperon et al., there is a clear anti-correlation between the LBIC and the PL intensity: insufficient carrier extraction due to deficient electrical contact results in decreased current collection and increased radiative recombination [8].

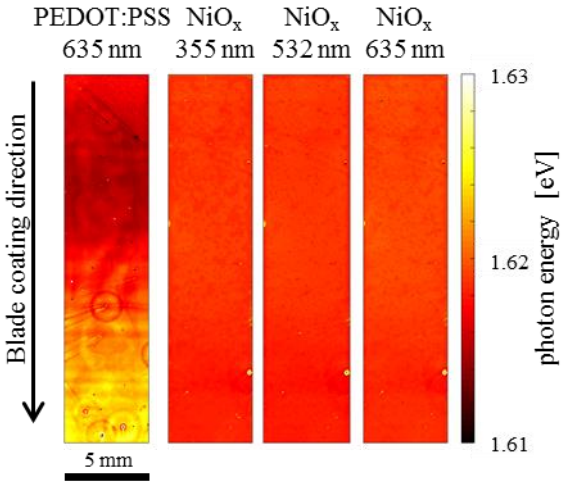

Figure 5.21 Results of the PL spectroscopy mapping for both cells, showing the photon energy of the PL peak position. The NiO_x sample was analyzed using three different excitation wavelengths.

For both cells, DLIT measurements at multiple bias voltages were conducted between 0.6 V and 1.1 V. The power-calibrated results are shown in Figure 5.23 and Figure 5.24. They confirm the conclusion indicated by the striking difference in the open-circuit voltage: The PEDOT:PSS sample from the early development process reveals multiple areas of increased dissipated power whereas for the NiO_x sample almost no features of significance were detected. Note that the scale bar is more than one order of magnitude lower, which corresponds directly to the lower dark current in the global dark J-V curve. The single visible point-shaped spot causes a power loss corresponding to an absolute efficiency loss of $0.03\%_{abs}$.

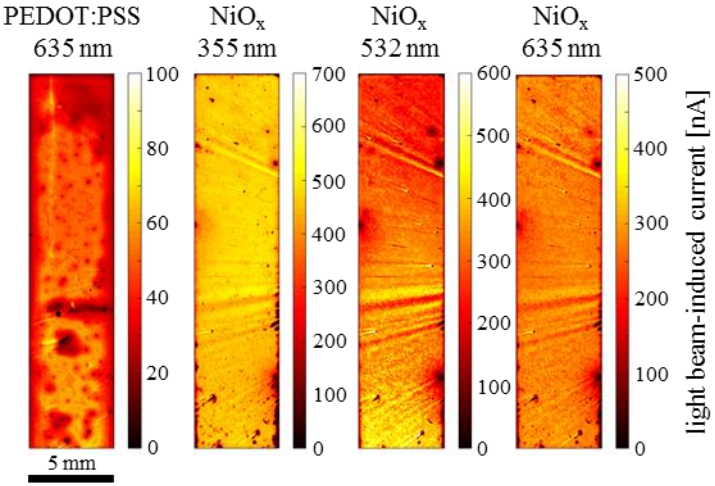

Figure 5.22 Results of the LBIC mapping for both cells. The NiO_x sample was analyzed using three different excitation wavelengths.

The DLIT maps clearly show that there are no major local recombination losses in the NiO_x cell, therefore the local J-V analysis is only demonstrated for the PEDOT:PSS cell. Increasing the measurement time can improve the sensitivity of the method and yield a higher signal-to-noise ratio, however this demands a level of stability that the PSCs under investigation did not show.

Maps of the open-circuit voltage, the pseudo fill factor and the dark saturation current of both diodes in the 2-diode-model are shown in Figure 5.25. V_{oc} values are within the range of expectable values, as does the pseudo-fill factor when compared to Suns-V_{oc} measurements where values > 0.85 had been determined (data not shown).

The average V_{oc} value is $0.91\,V$ and therefore slightly higher than the globally determined value from the light J-V curve but still in reasonable agreement.

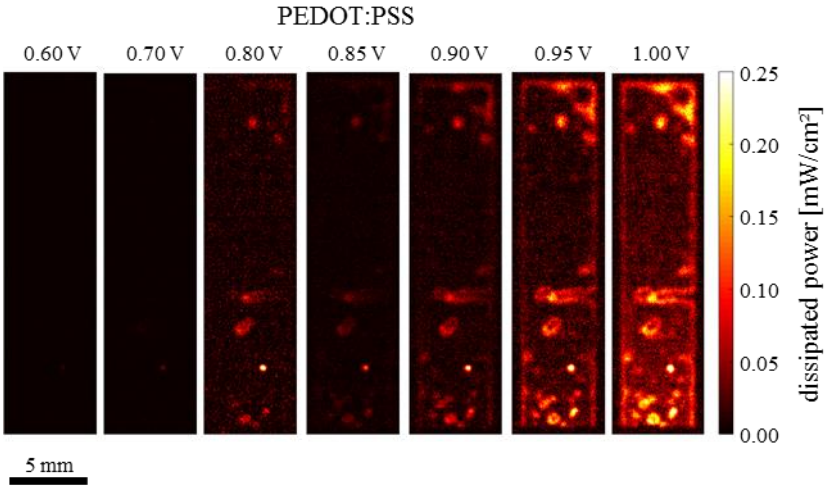

Figure 5.23 Images of the dissipated power at different bias voltages for the PEDOT:PSS sample from DLIT measurements. An increased recombination loss is revealed at the edges as well as for multiple local spots and a structure in the middle of the sample which is tentatively attributed to a scratch.

For all images of the PEDOT:PSS cell, a gradient from top to bottom is visible. Towards the bottom edge, we observe a slightly higher current for this cell (cf. Figure 5.22). As isolated observation, this could be explained by a slope in the layer thickness and consequent stronger absorption. Considering the gradient in the PL intensity in Figure 5.21, we observe a decrease of the radiative recombination towards the lower edge. This can be either due to efficient charge extraction – which would be in agreement with the observation for the LBIC signal – or due to enhanced non-radiative recombination, suggesting a higher defect density. The elevated heat dissipation towards the lower edge, as detected by the DLIT measurements (cf. Figure 5.23) points towards the increase in non-radiative recombination.

The same gradient is observed for the PL peak position (c.f. Figure 5.21) for the non-optimized process. An assumed variation in layer thickness along the coating direction, as indicated in Figure 5.21, could influence the PL emission spectrum by

reabsorption of high-energy photons. However, this would lead to a red-shift of the PL peak and does not comply with the observations.

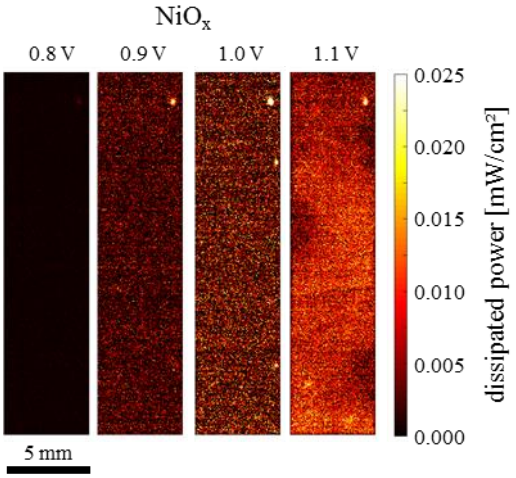

Figure 5.24 Images of the dissipated power at different bias voltages for the NiO_x sample from DLIT measurements. As expected from the cell's high V_{oc}, no significant recombination loss was detected. Note that the scale bars differ by one order of magnitude compared to Figure 5.23.

Assuming the non-radiative recombination has a significant thermal impact on the lattice, it would lead to a wider bandgap and a blue shift of the PL peak, accordingly. The influence of temperature on the bandgap and PL spectrum of $MAPbI_3$ is well known from literature [267–269]. Changes in the crystallization along the coating direction could also lead to a variation in crystal size and lattice stress which in turn affects the bandgap [5, 116, 216–219]. Based on the existing data set, no unambiguous conclusion can be derived. As this gradient did not occur in samples made from the improved process, no further investigations were conducted.

In the next section, the multiple local features are discussed and correlated to individual processing steps:

1) Edge region: Most distinct are the edge losses in the LBIC map, although they are also visible in the V_{oc}, pFF and J_{01} maps. These effects can be caused by physical damage by the shadow masks or a variation of

temperature during the thermal evaporation of the contacts. The "dark" edges in Figure 5.23 correspond to areas outside the evaporated back electrode and thus the active area of the cell, where no current can be collected.

2) Scratch: Slightly below the middle of the PEDOT:PSS cell there is an extended linear defect that shows as a thin dark line in the LBIC map and correspondingly a thin bright line in the PL intensity map (cf. Figure 5.20). Most clearly visible is its effect on the local J-V parameter in the V_{oc} and J_{01} maps: the voltage drop and the increase of the dark saturation current, respectively, due to this defect surround it: the scratch disrupts the electrical connection of the defected area; hence any recombination currents only flow in an area directly adjacent to the defect. Similar current patterns have been observed on silicon solar cells with disrupted front-side metallization [19].

3) Comet-shapes: Caused by particles on the substrate during spin coating processes (cell position on substrate: left of the center). Since the perovskite layer was blade coated these effects can only be caused by the application of the AZO, PCBM or PEDOT layer. This is confirmed by the observation that these effects are most prominently visible in the LBIC map and only partly in the PL map, as defects in the contact layers primarily affect the extraction quality. Remnant particles in the solutions are deposited on the sample surface and prohibit homogeneous distribution of the solution also for the following solution-based deposited layers. These particles, as revealed by the high-resolution LBIC maps, hinder efficient charge carrier extraction or increase the reflectance and thus decrease local current flow. Also the subsequently generated comet-shaped features are caused by these particles and are most likely due to variation in the layer thickness, hence a variation in absorbance.

4) Blade coating effects: comparable to the comet-shapes, particles on the surface can cause inhomogeneities during blade coating. The coating direction in the displayed maps is top to bottom. Close to the lower edge there are multiple spots visible, some exhibiting comet-shapes, others solely blade coating stripes. This proves that particles get to the substrate surface after the PEDOT:PSS process and also that the initial comet-shapes originate from that spin coating step.

5) Drying effects: An overlaying pattern formed during the drying of the perovskite layer is visible in the PL and even more pronounced in the LBIC map. The most sensible explanation is the layer thickness variation that causes higher absorption and therefore a higher photocurrent generation.

By using multiple characterization techniques, the influence of individual processing steps can be revealed and therefore the approach presents a valuable tool for identifying potential process improvements.

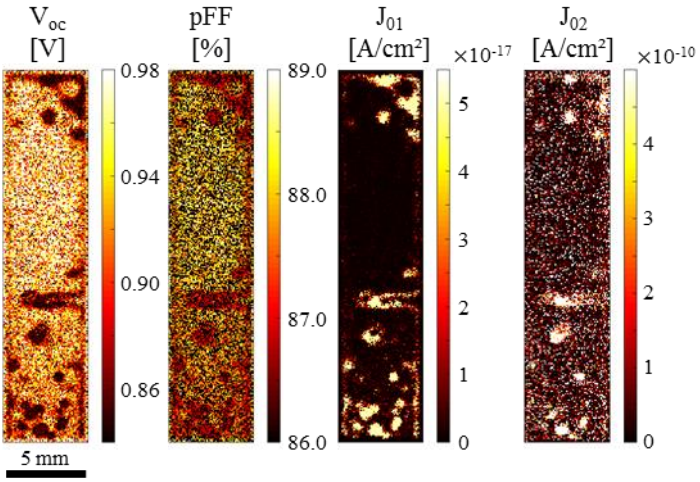

Figure 5.25 Results of the DLIT-based local J-V analysis for the PEDOT:PSS sample. The average V_{oc} (0.91 V) is slightly higher than the V_{oc} determined in the illuminated J-V measurement.

5.2.5 Loss Analysis

In order to summarize and evaluate the lateral efficiency distribution, the maps of the open-circuit voltage and the short-circuit current are used to calculate an efficiency map. In PSC characterization, this is a novel and unique approach to quantify the local efficiency across the complete cell area.

In a second step, the efficiency maps are further analyzed by calculating the average efficiencies including and excluding specific local defects and their comparison in relation to the cell efficiency potential.

For the PEDOT:PSS cell, the local V_{oc} was determined by the local J-V analysis and the local J_{sc} estimated from a LBIC map obtained with the $635\,\mathrm{nm}$ laser. To calculate the local efficiency from these two maps, the global fill factor of 0.71 from the J-V measurement in reverse direction was used (cf. Table 5.1). Figure 5.26 shows the summary of the three maps showing V_{oc}, J_{sc} and η. The efficiency map is a clear superposition of the two underlying maps, allowing for a quantitative representation of the local features discussed in the previous section in absolute efficiency.

The average cell efficiency based on the η map is 9.6% and therefore only slightly higher than the globally determined value from the J-V measurement in reverse direction of 9.25%. This is due to the minor overestimation of the local V_{oc}. In the map depicted in Figure 5.26, it can clearly be seen that locally much higher efficiencies can be reached. Hence, the cell has a significantly higher efficiency potential that can be reached by processing homogeneous layers.

For the cell from the improved process with NiO_x as HTL, the local efficiency was calculated from the global V_{oc} and the J_{sc} estimation based on three LBIC maps: from the DLIT measurements it was found, that no significant local recombination losses have an impact on the cell's voltage, therefore the global value of $1.07\,\mathrm{V}$ was used for the efficiency calculation. For the local current distribution of the NiO_x cell, the spectral dependency was taken into account and the local J_{sc} was estimated from the EQE-weighted LBIC maps obtained by three different laser excitation wavelengths as described in Section 5.2.3. Using the global fill factor from the J-V measurement in reverse direction of 0.61, the local efficiency was calculated. The map is depicted in Figure 5.26. As the J_{sc} is scaled to match the global cell current and both FF and V_{oc} are taken from Table 5.1, the average efficiency equals the global efficiency of 11.7%. As the η map merely has different scale compared to the J_{sc} map, the features discussed earlier can now be matched with an absolute efficiency value.

In the next step, three different areas were defined and the average efficiency was calculated. The first area includes the complete cell, the second area excludes the edge region, that is the outer $1\,\mathrm{mm}$ of the overall dimensions. These two areas are identical for both the PEDOT:PSS and the NiO_x cell. The third region was chosen individually as is represents the best local efficiency. For this purpose, a $1-3\,\mathrm{mm}^2$ sized spot was selected in the best area of the η map in Figure 5.26.

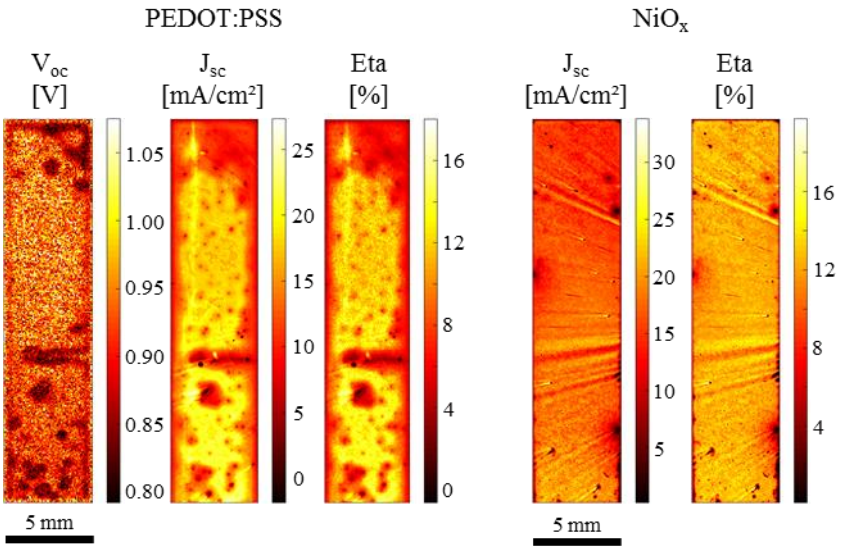

Figure 5.26 Results summary for a) the PEDOT:PSS cell: maps of the V_{oc}, J_{sc} and the calculated efficiency based on a global fill factor of 0.71 and b) for the NiO_x cell based on a global V_{oc} of 1.07 V and a global fill factor of 0.61.

These three average efficiency values are then put into relation with what is for now considered the cell's efficiency potential. This potential quantified by the highest efficiency achieved for the same architecture on small cell area ($0.0925\ cm^2$) in Uli Würfel's group at the FMF. In case of the PEDOT:PSS cell this is 14.2% and for the NiO_x cell it is 16.8%. These two values will be considered 0% efficiency loss for the loss analysis depicted in Figure 5.27.

Compared to this "efficiency limit", the three average values for the different regions are displayed as bars in negative y-direction, which gives the efficiency loss in absolute percent ("$\%_{abs}$").

The orange bar corresponds to the difference between the cell limits (as indicated in the graph) and the best local area. Here it can be seen, that the PEDOT:PSS cell is much closer to the achieved value on small cells with a loss of $0.2\%_{abs}$ compared to the NiO_x cell with a loss of $1.4\%_{abs}$. This is also reflected by the very low FF of the latter caused by high series resistance. Nevertheless this also means that these local values of 14.0% and 15.4% for the PEDOT:PSS and the NiO_x cell, respectively, are well within reach for the overall cell performance.

The checkered green bar indicates the loss due to distributed heterogeneities, the difference between the best local area and the larger cell area excluding the edge. This is by far the largest share of the efficiency loss and of comparable magnitude for both the PEDOT:PSS and the NiO_x cell, as high as $3.2\%_{abs}$. Hence it can be concluded that even in the improved process, the non-uniform deposition of the functional layers still have a significantly detrimental effect on the cells' performance.

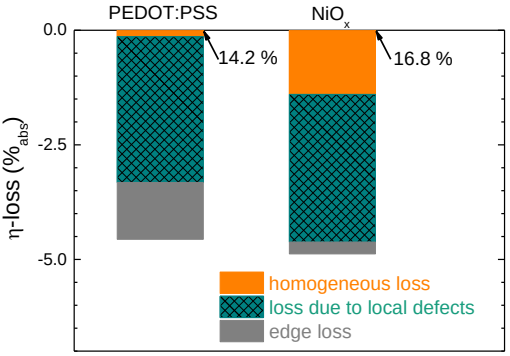

Figure 5.27 Efficiency loss analysis for both cells. The comparison (η-loss = 0 %) is the highest achieved efficiency (in our lab) for the respective architecture on small scale: 14.2 % for PEDOT:PSS cells and 16.8 % for NiO_x cells.

The last bar in grey corresponds to the loss in the edge region. This illustrates plainly the improvement due to the adaption of the cell process. The difference between including and excluding the outer 1 mm is $1.2\%_{abs}$ for the PEDOT:PSS cell and could be reduced down to $0.3\%_{abs}$ for the NiO_x cell.

From this quantitative loss analysis derived from the spatially resolved efficiency maps, it can clearly be concluded that an improvement of the layer uniformity is indispensable for improving the overall cell performance. Undissolved particles on the substrate during solution-based deposition processes are prone to cause heterogeneities. Also a careful and controlled drying is essential to improve the layer homogeneity.

The techniques that have been employed in this analysis yield a resolution of approximately 100 µm and are therefore mainly sensitive to process-related

heterogeneities on this length scale. Smaller non-uniformities such as grain boundaries or morphologies can still influence the overall performance but are not detected by this method.

Nevertheless, being able to quantify the impact of heterogeneities enables a direct feedback to the manufacturer. Also the demand for large area imaging techniques will rise along with growing efforts to scale-up PSCs to full wafer size areas.

5.2.6 Conclusion

In this chapter, a comprehensive analysis of the spatially resolved efficiency losses was introduced. Multiple mapping and imaging techniques were used to detect local heterogeneities and correlate them to individual processing steps. Maps of the estimated cell efficiency were derived from spectrally-weighted LBIC maps and a local J-V analysis based on DLIT measurements. This has been the first successful analysis including quantitative DLIT measurements of PSCs.

The overall technique was demonstrated on blade coated planar PSCs with inverted cell architecture. The cells featured an active cell area of $1.1\,\mathrm{cm}^2$ and conversion efficiencies approaching 12%. Two cells from different stage in the process development were chosen to highlight the method's value in identifying and quantifying process-related defects. The comparison between the two samples representing early stage research and an improved process with adjusted HTL shows which loss mechanisms have been decreased or even removed.

By employing this analysis, the improvement of the overall cell performance was supported: Guided by the knowledge about edge issues and impact of impurities during the processing, this analysis enabled the improvement of the deposition process and yielded efficiencies exceeding 11% with NiO_x as HTL. Furthermore, applying the gained knowledge, power conversion efficiency above 11% were achieved also for PEDOT:PSS-based devices with blade coated perovskite layers [262].

Despite the reduction of edge losses it was found that the impact of non-uniform layers persist to reduce the overall cell efficiency by more than $3\%_{abs}$ for both analyzed cells. The reachable efficiency potentials estimated from the best small areas in the η maps were found to be as high as 14% for the PEDOT:PSS cell and to exceed 15% for the NiO_x cell.

Therefore it can be definitely concluded that the improvement of the cell performance crucially depends on the improvement of layer uniformity. Removing all remnant particles in solutions and avoiding any dust particles during layer deposition will be one crucial step. Alongside with decreasing the resistive losses to achieve

higher fill factors, this is one of the main challenges that has to be addressed when working on upscaling of PSCs.

Going from lab-scale to full wafer size devices, controlling the layer homogeneity becomes a more and more challenging task but the presented quantitative local loss analysis will support and guide the path towards uniform and high-efficiency devices.

6 Accessing Monolithic Tandem Cells: Subcell-Selective Analysis

High-efficiency concepts based on multijunction solar cells enable record efficiencies of over 46% for III-V concentrator cells [4]. Also silicon-based cells exceed 33% in combination with III-V material and 25% in combination with perovskite materials [4].

The most feasible cell design for commercial application is a two-terminal configuration for it enables high voltages, has lower parasitic absorption and requires only one electrical converter. As discussed in Section 2.4.2, two-terminal devices where the subcells are connected in series. Consequently, the MJ solar cell is limited by the lowest cell current and a priori, most characterization reveal only parameters of the overall device. In a system consisting of two to four subcells and numerous layers, it is often challenging to identify loss mechanisms.

Approaches to access the individual subcells in MJ devices are commonly based on spectral selective excitation and/or detection. Selective excitations can be realized optically if the excitation light is only absorbed in one subcell. Selective detection of luminescence can be achieved by means of filtering the emitted photons or using spectrally resolved detection. If a measurement technique requires current extraction, charge carrier generation in all subcells is necessary to enable current flow through the complete device.

Luminescence based imaging techniques have been established for subcell-selective analysis of III-V MJ solar cells in recent years: from electroluminescence (EL) measurements, the internal voltages of individual subcells can be determined and local defects, such as shunts, can be detected. However, the series connection causes for these defects to also influence the current distribution in the adjunct subcells and this has to be considered carefully in the interpretation of EL imaging results [270, 271].

In MJ solar cells incorporating halide perovskites, only two studies of subcell-selective and spatially resolved analyses have been reported, including the investigation presented in this chapter. The second report is a degradation study on silicon perovskite tandem solar cells based on LBIC measurements [226]. In order to enable current flow in the probed subcell, this technique requires biasing the other subcell(s). Song et al. showed that the current generated in the perovskite cell decreases due to humidity-induced degradation while the current in the silicon cell increases simultaneously as the top cell transmits more light [226].

The presented PL-based analysis is easily transferable to various MJ solar cells including all-perovskite tandem solar cells and poses a valuable tool in the characterization of monolithic MJ solar cells.

6.1 Multi-Wavelength Photoluminescence Mapping

The results presented in this chapter have been published in the IEEE Journal of Photovoltaics [52] and partly go along the lines of the publication. This collaborative experiment was conducted in cooperation with researchers from Helmholtz Center Berlin (HZB) and École polytechnique fédérale de Lausanne (EPFL).

For this work, the tandem devices processed by HZB together with EPFL were used for the development and final demonstration of the method. All experimental work related to the characterization and analyses were conducted by the author.

The PL properties of both the individual subcells in a monolithic tandem device were investigated in order to evaluate the respective material qualities and to identify possible loss mechanisms. Using different excitation wavelengths, charge carriers were generated selectively in either the top or the bottom cell. The spectrally resolved detection of the PL signal additionally ensured the unambiguous separation of the two cells and allowed for precise determination of the perovskite bandgap. By analyzing the subcells incorporated in the monolithic device it was possible to determine the influence of the processing steps of the perovskite cell on the silicon bottom cell as well as the film quality of the perovskite when processed on a silicon substrate rather than TCO glass. The change of the substrate e.g. involves an effective change in temperature during the process due to different thermal conductivity.

With this method, important and easy-to-use tool to accompany the growing field of perovskite/silicon tandem research was introduced.

6.1.1 Tandem Solar Cell

At the time the author implemented this characterization technique, state of the art 2-terminal silicon perovskite tandem solar cells were approaching 20% efficiency. For the demonstration of its beneficial yield, a state of the art processed yet underperforming device was chosen, which the collaborators from HZB and EPFL kindly provided. The processing details and – at that time – record solar cell of certified 18 % efficiency were published in [13]. The device featured a monolithic tandem structure with a planar, Cesium-containing, triple cation perovskite top cell and a SHJ bottom cell. The cell's architecture is depicted in Figure 6.1 a with arrows to indicate the optical excitation via different wavelengths that are absorbed in the different absorber layers. The recombination layer is formed by SnO_2 and ITO, deposited via atomic layer deposition (ALD) and sputtering through shadow masks, respectively. Both the perovskite absorber layer and the hole contact material spiro-OMeTAD was spin coated on top and the stack is completed by thermally evaporated MoO_3, sputtered ITO and thermally evaporated LiF for reduced reflection.

The silicon substrate ($25 \times 25\ mm^2$) contains multiple, electrically isolated tandem solar cells, defined by the intermediate and top ITO layer: One with a large active area of $10 \times 10\ mm^2$ and five smaller cells, each with an active area of $4 \times 4\ mm^2$. Figure 6.1 b shows the schematic arrangement of these individual cells on the silicon substrate and the respective length scales.

The multi-wavelength PL measurements were subsequently performed under steady state conditions using the following excitation intensities: $7.03\ W/m^2$ for the 905 nm laser, $0.11 W/m^2$ for the 635 nm laser and $0.13\ W/m^2$ for the 532 nm laser. Due to the low PL efficiency, significantly higher excitation intensity has to be used for the silicon PL measurement.

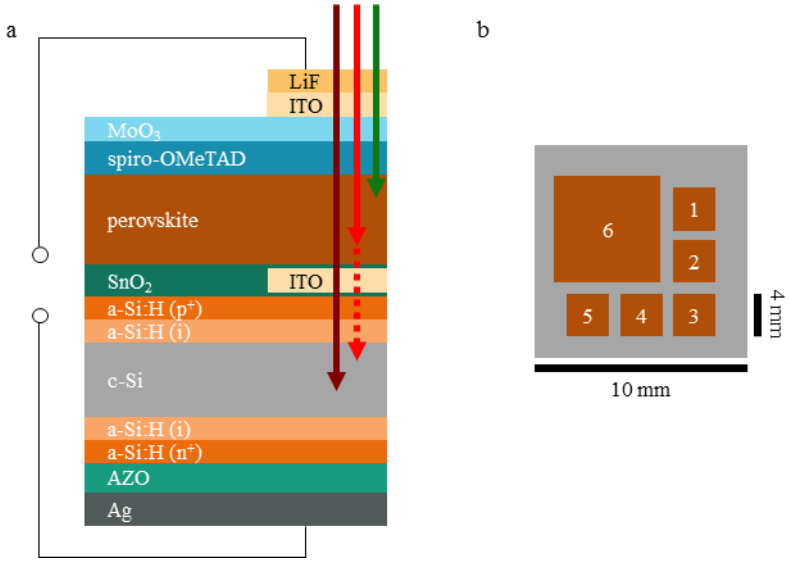

Figure 6.1 Device architecture for silicon perovskite tandem solar cell (a) arrows indicate the approximate penetration depths of the different excitation wavelengths. Schematic arrangement of cells on the silicon substrate (b).

Table 6.1 Initial current-voltage parameters of tandem cells used in the multi-wavelength PL analysis. Hysteresis effects mainly influence the fill factor.

Cell #	Scan Direction	J_{sc} [mA/cm²]	V_{oc} [V]	FF [%]	η [%]
1	forward	13.16	1.79	66.9	15.79
1	reverse	13.16	1.81	71.8	17.07
2	forward	13.32	1.80	67.4	16.13
2	reverse	13.32	1.81	72.2	17.41
3	forward	13.33	1.79	68.2	16.30
3	reverse	13.34	1.81	73.2	17.66
4	forward	13.19	1.79	66.9	15.79
4	reverse	13.19	1.80	70.7	16.81
5	forward	13.25	1.80	68.4	16.34
5	reverse	13.26	1.81	72.3	17.38
6	forward	13.72	1.81	54.0	13.39
6	reverse	13.71	1.83	57.9	14.48

Table 6.2 Results of re-measured current-voltage parameters of the analyzed tandem cells, three months after the initial measurements.

Cell #	Scan Direction	J_{sc} [mA/cm²]	V_{oc} [V]	FF [%]	η [%]
1	forward	12.26	1.77	63.9	13.86
2	forward	13.73	1.81	66.7	16.58
3	forward	13.76	1.81	68.0	16.96
4	forward	12.64	1.72	63.8	13.90
5	forward	13.22	1.81	68.7	16.47
6	forward	13.53	1.83	54.9	13.61

The penetration depth of light into the tandem cell structure depends on its wavelength: while the 532 nm laser probes the perovskite cell closer to the surface, the red laser penetrates deeper into the material and can also generate charge carriers in the silicon bottom cell (depending on the absorption properties and thicknesses of the overlying layers). The perovskite top cell is almost completely transparent for the infrared laser, except for parasitic absorption especially in the hole transport layer consisting of spiro-OMETAD. Thus, the charge carrier generation under IR excitation occurs exclusively in the silicon bottom cell.

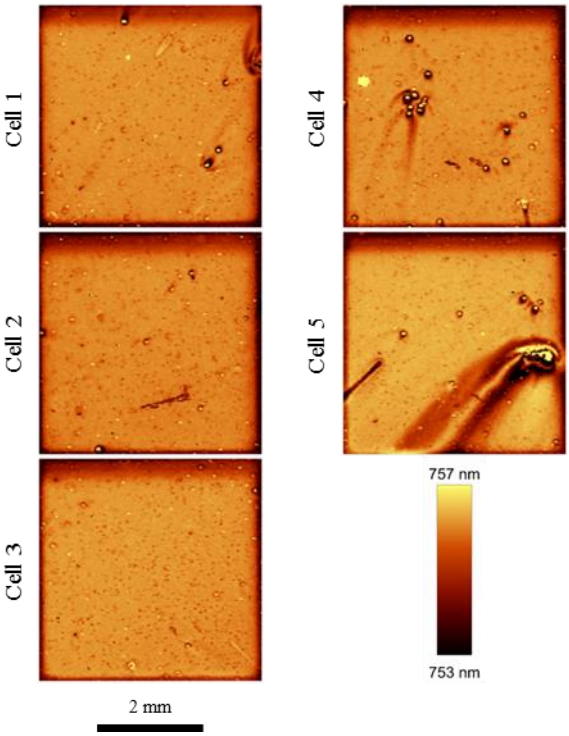

Figure 6.2 Lateral distribution of the PL peak position for the perovskite absorber, obtained from the 635 *nm* measurement.

Laser filters are applied for the different excitation lasers, respectively, in order to attenuate residual laser light on the detector. Details about the confocal microscopy setup used for the PL spectroscopy mapping are given in Section 3.1.1.

Electrical parameters of the tandem devices are summarized in Table 6.1: it shows the cells' initial performance after processing. Since the PL analyses were performed some time afterwards, the J-V curves were re-measured to account for possible degradation. The new set of parameters measured prior to the experiment can be found in Table 6.2. The initial measurements include both scan directions from short-circuit to open-circuit conditions (forward) and from open-circuit to short-circuit conditions (reverse), obtained with a scan speed of 500 mV/s. Slight hysteresis was observed, mainly affecting the fill factor. Since the motive for re-measuring the cells was to exclude severe degradation, only forward scans from short-circuit to open-circuit were performed.

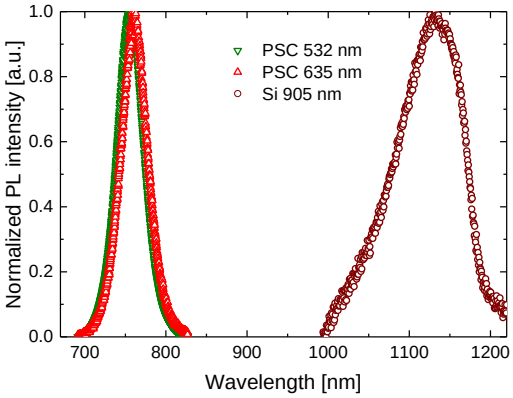

Figure 6.3 Normalized photoluminescence spectra measured on a tandem device using three different excitation wavelengths. The spectra are comparable to luminescence spectra in the literature of isolated perovskite or silicon samples.

6.1.2 Photoluminescence Spectrum

Representative spectra for the different wavelengths corresponding to the emitted PL by either the silicon or the perovskite absorber are depicted in Figure 6.3. The luminescence spectra obtained on the tandem device are well comparable to isolated perovskite or silicon devices. The perovskite bandgap can be determined from the spectrum, its average peak position is centered at 756 nm, corresponding to a peak-PL derived bandgap of 1.64 eV. This is well within agreement for values achieved by the triple cation based mixed perovskite absorber and close to the ideal bandgap for silicon

based tandem solar cells. The lateral distribution, calculated from Gaussian peak fits to the PL spectra obtained in the 635 nm measurements, is depicted in Figure 6.2.

6.1.3 Local Photoluminescence Intensity

Spatially resolved PLS measurements of all small cells on the substrate (cell area $4 \times 4\ \mathrm{mm}^2$) were conducted subsequently for excitation with the three different laser wavelengths. A vast variety of features and differences in the PL intensity were observed within the single pixels as well as between the pixels on the silicon substrate. This extended also to the results for the different excitation wavelengths. An overview for the spatially resolved PL results is given in Figure 6.4. For the three different wavelengths 532 nm, 635 nm and 905 nm the qualitative PL intensity is shown in the pixel maps, scaled equally for each wavelength. Multiple features that arouse attention were apparent:

a) In all maps, the edge regions show distinct contrast to the inner cell area.
b) Comet-like stripes originating from the center of the silicon substrate are visible in most PL and all reflectance maps.
c) Two distinct dark spots appear repeatedly in the lower left region both in the 532 nm and in the 635 nm measurement for all cells, which correspond to layer damage due to contacting the top ITO layer with metal pins in order to perform electrical measurements. Additional and more distinct marks of two pins in cells 2-5 originate from contacting tests, for cell number 2 these marks smeared to one scratch.
d) The maps measured with the 635 nm laser in Figure 6.4 exhibit additional substructures: firstly small dark spots with extensions of $10 - 30\ \mu\mathrm{m}$ can be observed and secondly, a distinct mottled pattern is visible all over the cells in the range of hundreds of micrometers.
e) Lastly, the silicon cell measured with the 905 nm laser excitation displays the point like spots as well as some stripes. Additionally, extended areas with lower PL intensities appear on all cells, some are clearly connected beyond single cell areas.

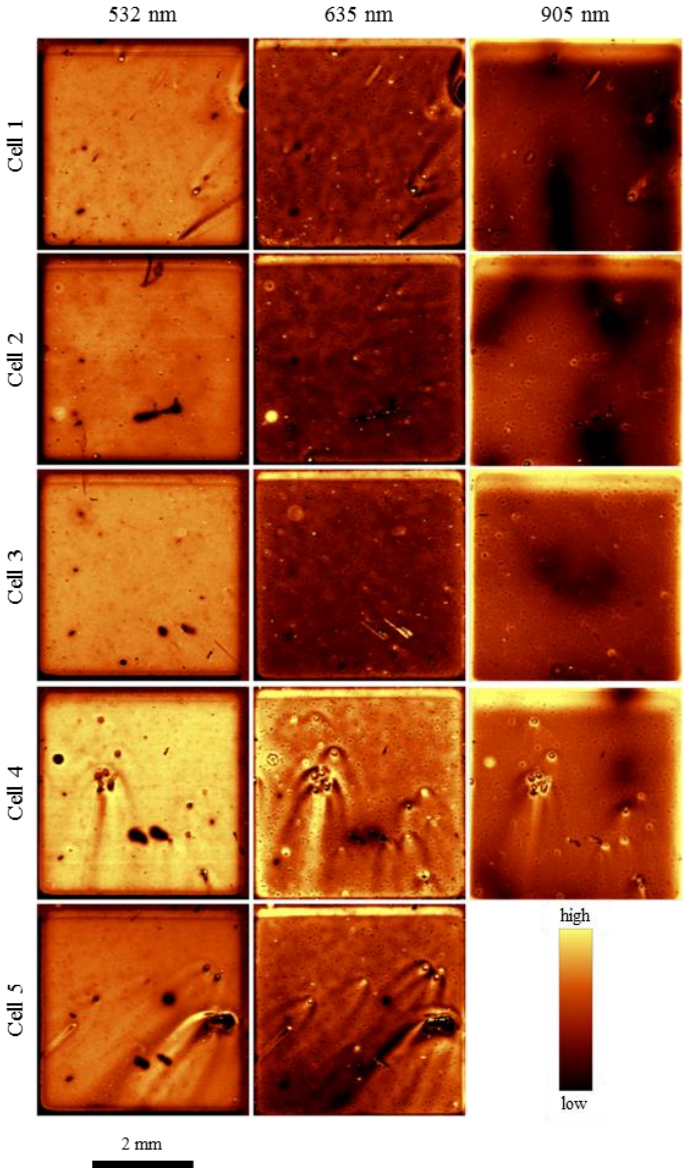

Figure 6.4 Spatially resolved PL intensity maps for ascending excitation wavelengths, scaled equally within one excitation wavelength.

6.1.4 Local Reflectance

In order to put the observations into context and to facilitate correlating the individual features with cell properties, absolute reflectance was measured for the complete substrate and several wavelengths using an integrating sphere. The maps in Figure 6.5 clearly show a radially symmetric pattern originating from the substrate center.

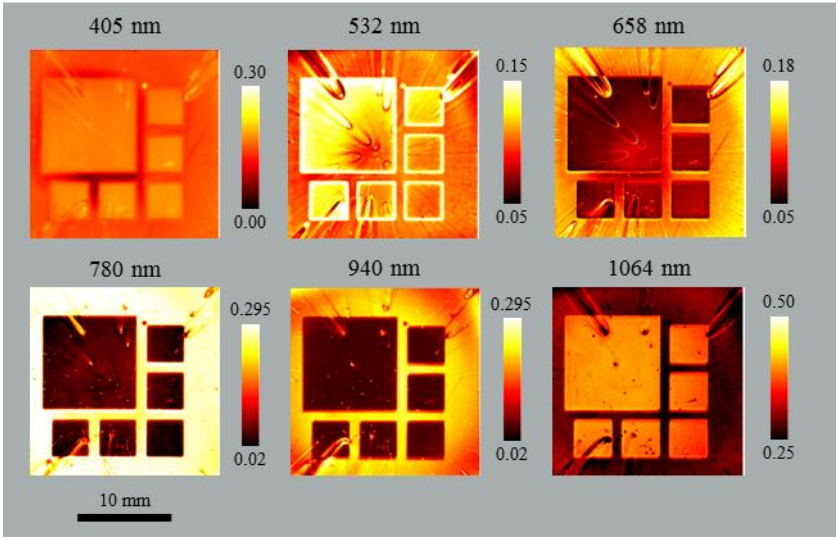

Figure 6.5 Absolute reflectance maps of the complete silicon substrate incorporating the five small pixels and the bigger, 10x10 mm² pixel in the upper left corner. Maps were obtained consecutively for different wavelengths ranging from UV to IR.

The highest resolution for this method is 25 µm/pixel, thus much lower than the resolution of the PL map. In order to obtain a higher spatial resolution, the confocal setup was used to record the reflected excitation light at 532, 635 and 905 nm wavelength for cells 1 and 3. Special attention has to be paid concerning the origin of the reflected light. Compared to a measurement of the PL emission all interfaces and intermediate layers in the range of the penetration depth contribute to the measurable reflectance signal. Neither the sponge-like pattern nor the extended dark features appear in the 635 nm or the 905 nm map (cf. Figure 6.6), respectively. Hence, it can be concluded that these features are not caused by heterogeneous reflectance.

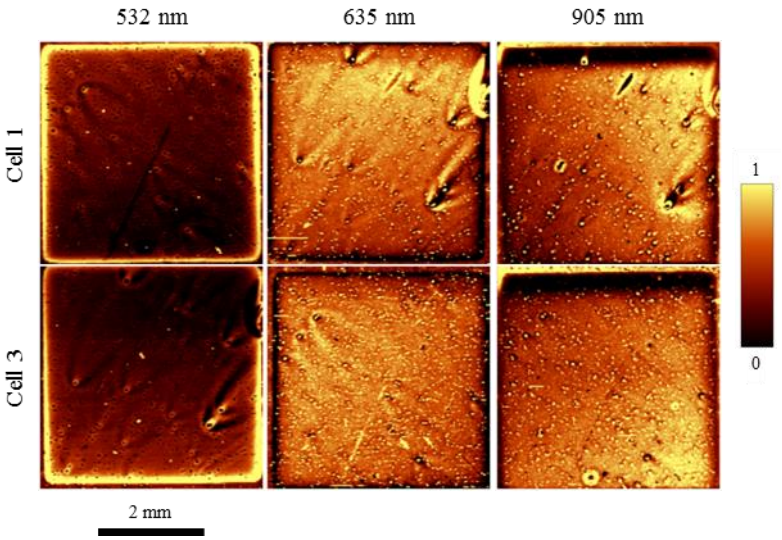

Figure 6.6 High-resolution confocal reflectance maps of cells 1 and 3 for the applied excitation wavelengths in the PL analyses, normalized values.

6.1.5 Discussion

Due to the two additional ITO layers, there is a distinct divergence between active cell area and the rest of the substrate. The strongly pronounced frames of the individual cells indicate a minor misalignment of the shadow mask used for the ITO deposition. Regarding the reflectance maps for multiple wavelengths (cf. Figure 6.5) conveys this conjecture. Comparing PL and reflectance maps, these frames appear in reversed intensity: higher reflectance indicates lower absorbance, which, in turn, leads to lower PL due to the decreased charge carrier density and vice versa.

The radially symmetric patterns in the PL maps can be attributed to process-related heterogeneities: A thickness variation is the expected underlying cause of these patterns, which is most likely caused by particles/agglomerates on the substrate impairing the spin coating process and therefore causing an unevenly deposited layer with comet-like features, this effect has been observed before [51, 56, 219]. The manufacturing process of the analyzed device includes two spin coating steps: depositing the triple cation perovskite in the one-step approach using solvent quenching [13, 29] and the hole transport layer spiro-OMETAD. The unambiguous identification of the point-like structure was impeded as such structures have not been observed in comparable samples but exclusively occurred in these cells.

The mottled pattern in the 635 nm map in Figure 6.4 can be caused by either interference due to a heterogeneously deposited perovskite layer or varying surface recombination. Since the 635 nm laser penetrates the material deeper than the shorter wavelength laser and they do not appear in any of the reflectance maps, it is assumed that these larger substructures originate from within the perovskite layer.

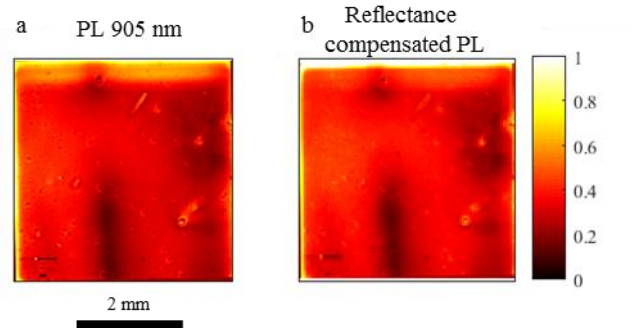

Figure 6.7 Original (a) and reflectance compensated (b) PL map for the silicon bottom cell 1.

The micrometer sized features in the 905 nm maps in Figure 6.4 that have also been observed in the perovskite PL maps appear to originate from the perovskite top cell. In order to analyze the origin of the unexpected features that are untypical for silicon PL maps, the spatially resolved reflectance for several wavelengths was measured. The observed pattern in the 905 nm reflectance maps support the hypothesis that these features are optical effects and do not originate in the silicon crystal volume. Thus, a compensation of the reflectance artifacts in the 905 nm PL map may be done: A higher reflectance means a lower excitation density in silicon. To first order the PL intensity is linearly proportional to the injection density at moderate injection conditions. Figure 6.7 b shows the reflectance compensated PL map for cell 1: $PL' = PL/(1 - A \times R)$, both maps ($PL$,$R$) were obtained with the confocal setup. A scaling factor A is introduced since the reflectance map is not calibrated to absolute values. It can be seen that different features in the PL image Figure 6.7 a (e.g. bright area at the top as well as different localized spots) are attenuated and can thus be attributed to optical effects.

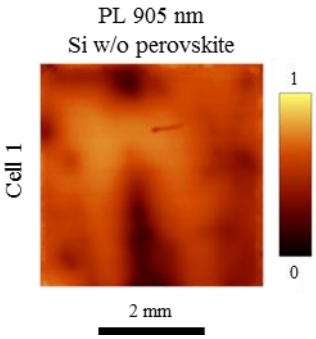

Figure 6.8 Normalized PL map of the silicon bottom cell after the removal of the perovskite top cell.

In order to cross-check our interpretation of the 905 nm excitation PL maps, we removed the perovskite top cell including the top ITO layer using ethanol and hydrochloric acid (HCl) and repeated the PL measurement on the silicon bottom cell. The corresponding PL map with 905 nm excitation does not display any micro feature (cf. Figure 6.8). This confirms the hypothesis that the micro features, which also appeared in the reflectance maps before etching, are optical effects in the top cell. The bare silicon cells exhibit the same larger area features with lower PL intensity that were also apparent in the measurement of the silicon cells still incorporated in the complete tandem device. Such extended defects are common in silicon, as several detrimental impurities in silicon feature a macroscopic diffusion length (e.g. transition metals such as cupper at room temperature or iron at elevated processing temperatures [272]).

6.1.6 Conclusion

In this work, a technique to separately analyze both subcells in a monolithic perovskite silicon tandem solar cell in a non-destructive way was demonstrated. Using variable laser excitation wavelength, the photoluminescence emission and light reflection in different layers could be probed with micrometer resolution. In particular, the direct access of the silicon bottom cell included in the device was enabled by using infrared excitation light for which the perovskite top cell is transparent. Optical effects in the silicon PL map could be distinguished from extended silicon bulk defects by comparison to reflectance maps. This technique yields a unique approach to characterize monolithic perovskite silicon tandem cells in different stages of processing, and hence the influence of succeeding processing steps on the silicon base

materials, therefore excluding discrepancies due to film forming variations on different substrates when changing from TCO glass to silicon substrates. In conclusion, a non-destructive, straightforward method to characterize silicon perovskite tandems layer by layer and thus provide valuable feedback throughout the processing was introduced.

7 Appendix

7.1 Solar Cell Fabrication Details

In this section, additional details about the fabrication of samples investigated in this thesis are given if there is no separate and explicit journal publication about the processing details. Such a publication exists for both the blade coated solar cells used in the quantitative local loss analysis and the silicon perovskite tandem solar cells used for demonstrating the multi-wavelength PL approach. In these two cases, the reader is directly referred to the publication.

7.1.1 Wrinkled Perovskite Morphology

This description is partly along the lines from the corresponding journal publication [46]:

Planar p–i–n perovskite solar cells were fabricated as a layered stack of glass/ITO/NiO_x/$Cs_{0.17}FA_{0.83}Pb(I_{0.83}Br_{0.17})_3$/$C_{60}$/BCP/Cu. Patterned ITO-coated glass substrates were cleaned in acetone, detergent (Mucasol 2 vol% in water), water and isopropanol in an ultrasonic bath for 15 min, respectively. Before layer deposition the substrates were dried in a N_2 stream and treated in an UV ozone cleaner (FHR Anlagenbau GmbH, UVOH 150 LAB) for 15 min. The NiO_x layer was deposited by a sol-gel method, closely following the procedure from You et al. [251]. A 1 M solution of nickel(II) nitrate hexahydrate in ethylene glycol with an equimolar amount of ethylene diamine was prepared and stirred for 10 min. After filtration through a 0.45 µm PVDF filter, the solution was spin coated onto ITO-coated glass at 8000 rpm for 60 s with an acceleration time of 3 s in air. The wet film was dried at 100°C for 10 min followed by oxidation at 300 °C for 1 h in ambient conditions. The substrates were left to cool down and quickly transferred into a glovebox for deposition of all following layers under dinitrogen atmosphere. $Cs_{0.17}FA_{0.83}Pb(I_{0.83}Br_{0.17})_3$ layers were deposited in close analogy to previously reported procedure for this perovskite composition [16, 273].

A 0.9 M $Cs_{0.17}FA_{0.83}Pb(I_{0.83}Br_{0.17})_3$ precursor solution was prepared by dissolving cesium bromide (57.9 mg, 0.153 mmol, 0.17 equiv.), formamidinium iodide (128.5 mg, 0.747 mmol, 0.83 equiv.), lead(II) bromide (56.2 mg, 0.17 equiv.) and lead(II) iodide (344.4 mg, 0.747 mmol, 0.83 equiv.) in a mixture of dimethylformamide and dimethyl sulfoxide (4:1 volume ratio, 880 µL). The precursor solution was shaken at 60 °C for 30 min and left to cool down to ambient temperature before use. Higher or lower concentrated perovskite precursor solutions were prepared in the same way by adjusting the volume of solvent mixture added. Different deposition procedures were used to obtain perovskite layers with flat surface

morphology (Procedure 1, P1), moderately wrinkled surface morphology (Procedure 2, P2) and heavily wrinkled surface (Procedure 3, P3).

- P1: Perovskite precursor solution (100 µL) was spread on the substrate and spun at a single-step process with open spin coater lid, 4000 rpm for 30 s with an acceleration time of 1 s; during this process chlorobenzene (150 µL) was dripped from 1 cm distance on the center of the spinning substrate after 25 s. The perovskite layer was directly transferred on a hot plate for annealing at 100°C for 20 min.
- P2: Perovskite precursor solution (100 µL) was spread on the substrate and spun at a two-step process with closed spin coater lid, 1000 rpm for 10 s with an acceleration time of 1 s followed by 6000 rpm for 30 s with an acceleration time of 3 s; during this process chlorobenzene (150 µL) was dripped from 1 cm distance on the center of the spinning substrate after 42 s. The spin coating time is 40 s plus 4 s acceleration; in total 44 s. Antisolvent quenching was done 2 s before the end of spin coating, hence after 42 s. The perovskite layer was directly transferred on a hot plate for annealing at 50 °C for 1 min, then on a second hot plate at 100°C for 20 min.
- P3: A 1.6 M $Cs_{0.17}FA_{0.83}Pb(I_{0.83}Br_{0.17})_3$ precursor solution was prepared based on cesium bromide (57.9 mg), formamidinium iodide (228.4 mg), lead(II) bromide (99.8 mg) and lead(II) iodide (612.2 mg) in a mixture of DMF and DMSO (4:1 volume ratio). Spin coating conditions identical to process P2.

After cooling to ambient temperature, the electron selective layer (fullerene-C_{60}), hole blocking layer (bathocuproine) and back electrode (Cu) were deposited in a thermal evaporator (M. BRAUN GmbH, MB-EcoVap) at a base pressure of $< 10^{-6}$ mbar. First, 25 nm fullerene-C_{60} was vacuum deposited at a source temperature of 370 °C and rate of 0.3 Å/s, then 6 nm BCP was deposited at a source temperature of 125 °C and rate of 0.5 Å/s, finally, 100 nm copper was deposited through a shadow mask, to define six active areas of 16 mm^2 on each substrate, at a rate of 0.1 to 1.0 Å/s.

7.1.2 Graphite Based Perovskite Solar Cells

This description of the manufacturing process for the device structure used in Section 4.1 is partly along the lines of the corresponding journal publication [206]:

FTO coated glass plates of dimension $100 \times 100\ \mathrm{mm}^2$ were used initially. The TCO was patterned by laser ablation. The plates were cleaned in an ultrasonic bath for 2 min at 50°C in Mucasol detergent and for 1 min at 50°C in deionized water. Finally, the plates were rinsed in isopropanol and blow dried with nitrogen. A $25 - 30$ nm thick compact TiO_2 was deposited by spray pyrolysis on the cleaned glasses. For this purpose, a solution containing 0.05M of titanium disisopropoxy (bis) acetyl acetone (Sigma Aldrich) diluted in ethanol ($\geq$ 99.5% from Carl Roth) was used. A layer of approximately 600 nm of mesoporous TiO_2 was then screen printed with a paste prepared by mixing Dyesol DSL 18NRT with terpineol in 1:0.5 weight ratio. The film was sintered at 500°C for 30 min. Approximately 800 nm of porous ZrO_2 space layer was screen printed (Solaronix Zr-Nanoxide ZT/SP) and sintered at 500°C for 30 min. The stack was finished by screen-printing an approximately 7 µm thick graphite counter electrode on top (Solaronix Elcocarb B/SP). This stack resulted in an active area of 0.4 cm^2. The plates were finally sintered at 400°C for 30 min. The plates were then cut to substrates of $25 \times 25\ \mathrm{mm}^2$ dimensions and copper cables were soldered on the corresponding TCO patches. Electrical contact between the graphite patch and the wires was established with silver paste (G3692 Acheson silver DAG 1415). The cells were transported inside a nitrogen-filled glove box where they were heated to 120°C for 15 minutes to remove moisture. The PbI_2 layer was formed by dropping 7 µl of a 1.2M solution of PbI_2 (TCI, 99.99%) in N,N-dimethylformamide (DMF) (Sigma-Aldrich, 99.8%) at 70 °C close to the active area. After waiting for 1 min, the film was spin cast 2500 rpm for 10 s and annealed at 70°C for 30 min. The MAI solution for dipping consisted of 0.062M of MAI (Dyesol) in dried isopropanol (Merck, $\geq$ 99.9%).

8 Summary and Outlook

The focus of this thesis was the analysis of hybrid organic-inorganic halide perovskite absorbers from single crystals to complete devices: to generate in-depth understanding of material and cell parameters as well as the quality assessment of the variety of materials and fabrication processes, ultimately fostering the final photovoltaic device performance. This was achieved by means of multiple advanced characterization techniques focused on high temporal and spatial resolution. Generally, internal and external collaborations facilitated access to test samples for all investigations.

In a close collaboration across multiple research groups within Fraunhofer ISE, an in situ study of the perovskite crystal formation was conducted. Serving as a reference system for perovskites in photovoltaic applications, methyl ammonium lead iodide was chosen as absorber material for the investigation. Enabled by a graphite-based cell structure, the photovoltaic performance was accessed during the crystallization process:

The device architecture included both electron and hole transport layer before the absorber layer was formed. Between the contacts, the mesoporous scaffold comprised of TiO_2 and ZrO_2 was filled with PbI_2. The immersion in methyl ammonium solution therefore resulted in an immediate initiation of perovskite crystal formation and consequently to a operational solar cell. The kinetics of this crystallization were analyzed by real-time measurements of the external quantum efficiency as well as the photoluminescence emission spectrum. One major result was the identification of an additional stage during the perovskite formation, which had been overlooked by previous studies of the perovskite crystallization. In this stage, the photocurrent rises significantly after the crystal formation itself is assumed to be complete. This increase is attributed to the formation of electrical pathways between the electron and hole contact layers, thus enabling efficient charge carrier extraction.

Being highly relevant for tandem solar cell application, a high bandgap absorber material featuring an anomalous wrinkle-patterned morphology was investigated. The presented work was part of an extensive collaborative study together with researchers from the Helmholtz-Center Berlin regarding the influence of perovskite composition and processing parameters on the wrinkle formation and the optoelectronic properties. The author's contribution to the study was the spatially resolved analysis of the morphology and the optoelectronic properties of the $Cs_xFA_{1-x}Pb(I_{1-y}Br_y)_3$ perovskite absorber layer. Using a confocal microscopy approach, the spatial resolution was increased to the refraction limit. Thus, a superposition of scanning electron microscope

images and maps of spectral properties from the emitted photoluminescence revealed unambiguous correlation between the morphology and the photoluminescence emission properties. It was found that wrinkled areas exhibit larger crystals compared to the flat areas and a slightly red-shifted photoluminescence spectrum, which was attributed to lower lattice strain in the larger crystals. This theory was supported by energy dispersive X-ray spectroscopy measurements across the film's cross section. Perovskite phase separation could be ruled out for the elemental distribution across the morphology gave no indication for compositional de-mixing.

One major achievement of this thesis in the area of spatially resolved analyses was the introduction of a quantitative local loss analysis based on dark lock-in thermography imaging and light beam-induced current measurements at multiple excitation wavelengths. Hereby the step from merely detecting heterogeneities towards a quantitative loss analysis of open-circuit voltage, short-circuit current and resulting conversion efficiency was successfully achieved. The open-circuit voltage was determined by applying the local current-voltage analysis, an established method in silicon solar cell characterization. An estimate of the lateral distribution of the short-circuit current was acquired by external quantum efficiency weighted averaging the individual light beam-induced maps. The technique was demonstrated on perovskite solar cells with blade coted absorber layer and an active cell area of 1.1 cm^2. Two cells representing different levels of process optimization were selected. The cells' architecture was a planar inverted (p-i-n) structure featuring different hole transport materials: PEDOT:PSS or NiO_x. Upon revealing an edge loss of around 1% in absolute cell efficiency for the PEDOT:PSS cell from an early stage of the process optimization, the processing could be adapted resulting in a significantly reduced edge loss. Nevertheless, for both cells it was found that the non-uniformities decrease the overall cell efficiency by approximately 3% in absolute cell efficiency. It was therefore concluded that the optimization of the cell performance crucially depends on improving the layer homogeneity.

Regarding the spatially resolved analysis of multi junction solar cells, it was the main goal to add depth resolution via layer selective excitation. A photoluminescence based analysis of state-of-the-art monolithic tandem solar cells provided by the Helmholtz-Center Berlin was conducted. The cell was composed of a planar perovskite solar cell and a silicon heterojunction solar cell. The lateral distribution of heterogeneities could be attributed unambiguously to the individual subcells and furthermore related to manufacturing steps. The approach of depth-selective probing of

the silicon bottom was verified via a comparison of a reflection-attenuated image and for a final proof-of-principle, a measurement of the silicon cell after removing the perovskite top cell.

In conclusion, the selected studies yield valuable insights for the targeted optimization of organic-inorganic halide perovskite solar cells.

The introduced techniques are valuable tools for the characterization of various solar cell architectures. The subcell-selective probing by multi-wavelength excitation is a suitable probe for silicon based tandem solar cells as well as all perovskite solar cells, both of which are heavily investigated areas of research. This approach can be extended to other imaging techniques such as light beam-induced current and illuminated lock-in thermography.

As another key challenge in perovskite-related research, scaling the active cell area from lab-scale to wafer size is still impeded by heterogeneity losses. Increasing the scaling factor, that is the ratio of cell efficiency and cell area, will be supported by identifying and quantifying local efficiency losses.

Therefore, comprehensive and spatially resolved analyzes will be indispensable in future perovskite research.

9 Bibliography

References

[1] H. J. Queisser and E. E. Haller, “Defects in Semiconductors: Some Fatal, Some Vital,” *Science*, vol. 281, no. 5379, pp. 945–950, 1998.

[2] Fraunhofer-Institut für Solare Energiesysteme ISE, *Energy Charts.* [Online] Available: www.energy-charts.de/ren_share.htm. Accessed on: Aug. 02 2018.

[3] NREL, *Best Research-Cell Efficiencies.* [Online] Available: https://www.nrel.gov/pv/assets/images/efficiency-chart-20180716.jpg. Accessed on: 02.08.18.

[4] M. A. Green, Y. Hishikawa, E. D. Dunlop, D. H. Levi, J. Hohl-Ebinger, and A. W.Y. Ho-Baillie, “Solar cell efficiency tables (version 52),” *Progress in Photovoltaics: Research and Applications*, vol. 26, no. 7, pp. 427–436, 2018.

[5] Q. A. Akkerman, V. D'Innocenzo, S. Accornero, A. Scarpellini, A. Petrozza, M. Prato, and L. Manna, “Tuning the Optical Properties of Cesium Lead Halide Perovskite Nanocrystals by Anion Exchange Reactions,” (eng), *Journal of the American Chemical Society*, vol. 137, no. 32, pp. 10276–10281, 2015.

[6] A. Amat, E. Mosconi, E. Ronca, C. Quarti, P. Umari, M. K. Nazeeruddin, M. Grätzel, and F. de Angelis, “Cation-induced band-gap tuning in organohalide perovskites: Interplay of spin-orbit coupling and octahedra tilting,” (eng), *Nano letters*, vol. 14, no. 6, pp. 3608–3616, 2014.

[7] G. E. Eperon, S. D. Stranks, C. Menelaou, M. B. Johnston, L. M. Herz, and H. J. Snaith, “Formamidinium lead trihalide: A broadly tunable perovskite for efficient planar heterojunction solar cells,” *Energy & Environmental Science*, vol. 7, no. 3, pp. 982–988, 2014.

[8] T. Jesper Jacobsson, J.-P. Correa-Baena, M. Pazoki, M. Saliba, K. Schenk, M. Grätzel, and A. Hagfeldt, “Exploration of the compositional space for mixed lead halogen perovskites for high efficiency solar cells,” *Energy & Environmental Science*, vol. 9, no. 5, pp. 1706–1724, 2016.

[9] D. P. McMeekin, G. Sadoughi, W. Rehman, G. E. Eperon, M. Saliba, M. T. Horantner, A. Haghighirad, N. Sakai, L. Korte, B. Rech, M. B. Johnston, L. M. Herz, and H. J. Snaith, “A mixed-cation lead mixed-halide perovskite absorber for tandem solar cells,” *Science*, vol. 351, no. 6269, pp. 151–155, 2016.

[10] J. H. Noh, S. H. Im, J. H. Heo, T. N. Mandal, and S. I. Seok, “Chemical management for colorful, efficient, and stable inorganic-organic hybrid nanostructured solar cells,” (eng), *Nano letters*, vol. 13, no. 4, pp. 1764–1769, 2013.

[11] R. Prasanna, A. Gold-Parker, T. Leijtens, B. Conings, A. Babayigit, H.-G. Boyen, M. F. Toney, and M. D. McGehee, "Band Gap Tuning via Lattice Contraction and Octahedral Tilting in Perovskite Materials for Photovoltaics," (eng), *Journal of the American Chemical Society*, vol. 139, no. 32, pp. 11117–11124, 2017.

[12] E. L. Unger, L. Kegelmann, K. Suchan, D. Sörell, L. Korte, and S. Albrecht, "Roadmap and roadblocks for the band gap tunability of metal halide perovskites," *Journal of Materials Chemistry A*, vol. 5, no. 23, pp. 11401–11409, 2017.

[13] S. Albrecht, M. Saliba, J. P. Correa Baena, F. Lang, L. Kegelmann, M. Mews, L. Steier, A. Abate, J. Rappich, L. Korte, R. Schlatmann, N. Mohammad K., A. Hagfeldt, M. Grätzel, and B. Rech, "Monolithic Perovskite/Silicon-Heterojunction Tandem Solar Cells Processed at Low Temperature," *Energy & Environmental Science*, vol. 9, no. 1, pp. 81–88, 2016.

[14] C. D. Bailie, M. G. Christoforo, J. P. Mailoa, A. R. Bowring, E. L. Unger, W. H. Nguyen, J. Burschka, N. Pellet, J. Z. Lee, M. Grätzel, R. Noufi, T. Buonassisi, A. Salleo, and M. D. McGehee, "Semi-transparent perovskite solar cells for tandems with silicon and CIGS," *Energy & Environmental Science*, vol. 8, no. 3, pp. 956–963, 2015.

[15] K. A. Bush, S. Manzoor, K. Frohna, Z. J. Yu, J. A. Raiford, A. F. Palmstrom, H.-P. Wang, R. Prasanna, S. F. Bent, Z. C. Holman, and M. D. McGehee, "Minimizing Current and Voltage Losses to Reach 25% Efficient Monolithic Two-Terminal Perovskite–Silicon Tandem Solar Cells," *ACS Energy Letters*, pp. 2173–2180, 2018.

[16] K. A. Bush, A. F. Palmstrom, Z. J. Yu, M. Boccard, R. Cheacharoen, J. P. Mailoa, D. P. McMeekin, R. L. Z. Hoye, C. D. Bailie, T. Leijtens, I. M. Peters, M. C. Minichetti, N. Rolston, R. Prasanna, S. Sofia, D. Harwood, W. Ma, F. Moghadam, H. J. Snaith, T. Buonassisi, Z. C. Holman, S. F. Bent, and M. D. McGehee, "23.6%-efficient monolithic perovskite/silicon tandem solar cells with improved stability," *Nature Energy*, vol. 2, no. 4, p. 17009, 2017.

[17] F. Sahli, J. Werner, B. A. Kamino, M. Bräuninger, R. Monnard, B. Paviet-Salomon, L. Barraud, L. Ding, J. J. Diaz Leon, D. Sacchetto, G. Cattaneo, M. Despeisse, M. Boccard, S. Nicolay, Q. Jeangros, B. Niesen, and C. Ballif, "Fully textured monolithic perovskite/silicon tandem solar cells with 25.2% power conversion efficiency," *Nature materials*, vol. 9, p. 1552, 2018.

[18] J. Werner, C.-H. Weng, A. Walter, L. Fesquet, J. P. Seif, S. de Wolf, B. Niesen, and C. Ballif, "Efficient Monolithic Perovskite/Silicon Tandem Solar Cell With

Cell Area 1 cm(2)," (ENG), *The Journal of Physical Chemistry Letters*, vol. 7, no. 1, pp. 161–166, 2016.

[19] ITRPV, *International Technology Roadmap for Photovoltaic: 2017 Results*, 2018.

[20] Oxford PV, "Oxford PV sets world record for perovskite solar cell," Jun. 2018. [Online] Available: https://www.oxfordpv.com/news/oxford-pv-sets-world-record-perovskite-solar-cell. Accessed on: Sep. 03 2018.

[21] M. C. Brennan, S. Draguta, P. V. Kamat, and M. Kuno, "Light-Induced Anion Phase Segregation in Mixed Halide Perovskites," *ACS Energy Letters*, vol. 3, no. 1, pp. 204–213, 2017.

[22] J. Huang, S. Tan, P. D. Lund, and H. Zhou, "Impact of H 2 O on organic–inorganic hybrid perovskite solar cells," *Energy & Environmental Science*, vol. 10, no. 11, pp. 2284–2311, 2017.

[23] C. Seth and D. Khushalani, "Degradation and regeneration of hybrid perovskites," *RSC Advances*, vol. 6, no. 104, pp. 101846–101852, 2016.

[24] X. Tang, M. Brandl, B. May, I. Levchuk, Y. Hou, M. Richter, H. Chen, S. Chen, S. Kahmann, A. Osvet, F. Maier, H.-P. Steinrück, R. Hock, G. J. Matt, and C. J. Brabec, "Photoinduced degradation of methylammonium lead triiodide perovskite semiconductors," *Journal of Materials Chemistry A*, 2016.

[25] Y. Yao, G. Wang, F. Wu, D. Liu, C. Lin, X. Rao, R. Wu, G. Zhou, and Q. Song, "The interface degradation of planar organic–inorganic perovskite solar cell traced by light beam induced current (LBIC)," *RSC Advances*, vol. 7, no. 68, pp. 42973–42978, 2017.

[26] J. A. Christians, P. Schulz, J. S. Tinkham, T. H. Schloemer, S. P. Harvey, B. J. Tremolet de Villers, A. Sellinger, J. J. Berry, and J. M. Luther, "Tailored interfaces of unencapsulated perovskite solar cells for >1,000 hour operational stability," *Nature Energy*, vol. 3, no. 1, pp. 68–74, 2018.

[27] J.-W. Lee, D.-H. Kim, H.-S. Kim, S.-W. Seo, S. M. Cho, and N.-G. Park, "Formamidinium and Cesium Hybridization for Photo- and Moisture-Stable Perovskite Solar Cell," *Advanced Energy Materials*, vol. 5, no. 20, p. 1501310, 2015.

[28] N. Li, C. Cheng, H. Wei, H. Liu, X. Li, W. Li, and L. Wang, "Enhanced efficiency and stability of inverted perovskite solar cells by interfacial engineering with alkyl bisphosphonic molecules," *RSC Advances*, vol. 7, no. 67, pp. 42105–42112, 2017.

[29] M. Saliba, T. Matsui, J.-Y. Seo, K. Domanski, J.-P. Correa-Baena, M. K. Nazeeruddin, S. M. Zakeeruddin, W. Tress, A. Abate, A. Hagfeldt, and M.

Gratzel, “Cesium-containing triple cation perovskite solar cells: improved stability, reproducibility and high efficiency,” (ENG), *Energy & Environmental Science*, vol. 9, no. 6, pp. 1989–1997, 2016.

[30] M. Stolterfoht, C. M. Wolff, Y. Amir, A. Paulke, L. Perdigón-Toro, P. Caprioglio, and D. Neher, “Approaching the fill factor Shockley–Queisser limit in stable, dopant-free triple cation perovskite solar cells,” *Energy & Environmental Science*, vol. 10, no. 6, pp. 1530–1539, 2017.

[31] Y. Sun, X. Fang, Z. Ma, L. Xu, Y. Lu, q. yu, N. Yuan, and J. Ding, “Enhanced UV-light stability of organometal halide perovskite solar cells with interface modification and a UV absorption layer,” *Journal of Materials Chemistry C*, vol. 5, no. 34, pp. 8682–8687, 2017.

[32] X. Zhang, X. Ren, B. Liu, R. Munir, X. Zhu, D. Yang, J. Li, Y. Liu, D.-M. Smilgies, R. Li, Z. Yang, T. Niu, X. Wang, A. Amassian, K. Zhao, and S. Liu, “Stable high efficiency two-dimensional perovskite solar cells via cesium doping,” *Energy & Environmental Science*, vol. 10, no. 10, pp. 2095–2102, 2017.

[33] Y. Zhang, P. Wang, X. Yu, J. Xie, X. Sun, H. Wang, J. Huang, L. Xu, C. Cui, M. Lei, and D. Yang, “Enhanced performance and light soaking stability of planar perovskite solar cells using an amine-based fullerene interfacial modifier,” *Journal of Materials Chemistry A*, vol. 4, no. 47, pp. 18509–18515, 2016.

[34] E. L. Unger, E. T. Hoke, C. D. Bailie, W. H. Nguyen, A. R. Bowring, T. Heumüller, M. G. Christoforo, and M. D. McGehee, “Hysteresis and transient behavior in current–voltage measurements of hybrid-perovskite absorber solar cells,” *Energy & Environmental Science*, vol. 7, no. 11, pp. 3690–3698, 2014.

[35] A. Pockett, G. E. Eperon, N. Sakai, H. J. Snaith, L. M. Peter, and P. J. Cameron, “Microseconds, milliseconds and seconds: deconvoluting the dynamic behaviour of planar perovskite solar cells,” (eng), *Physical Chemistry Chemical Physics*, vol. 19, no. 8, pp. 5959–5970, 2017.

[36] H. J. Snaith, A. Abate, J. M. Ball, G. E. Eperon, T. Leijtens, N. K. Noel, S. D. Stranks, J. T.-W. Wang, K. Wojciechowski, and W. Zhang, “Anomalous Hysteresis in Perovskite Solar Cells,” (eng), *The Journal of Physical Chemistry Letters*, vol. 5, no. 9, pp. 1511–1515, 2014.

[37] H.-S. Kim and N.-G. Park, “Parameters Affecting I-V Hysteresis of CH3NH3PbI3 Perovskite Solar Cells: Effects of Perovskite Crystal Size and Mesoporous TiO2 Layer,” (eng), *The Journal of Physical Chemistry Letters*, vol. 5, no. 17, pp. 2927–2934, 2014.

[38] D. A. Jacobs, Y. Wu, H. Shen, C. Barugkin, F. J. Beck, T. P. White, K. Weber, and K. R. Catchpole, "Hysteresis phenomena in perovskite solar cells: the many and varied effects of ionic accumulation," (eng), *Physical Chemistry Chemical Physics*, vol. 19, no. 4, pp. 3094–3103, 2017.

[39] R. A. Belisle, W. H. Nguyen, A. R. Bowring, P. Calado, X. Li, S. J. C. Irvine, M. D. McGehee, Barnes, Piers R. F., and B. C. O'Regan, "Interpretation of inverted photocurrent transients in organic lead halide perovskite solar cells: Proof of the field screening by mobile ions and determination of the space charge layer widths," *Energy & Environmental Science*, vol. 10, no. 1, pp. 192–204, 2017.

[40] K. Domanski, B. Roose, T. Matsui, M. Saliba, S.-H. Turren-Cruz, J.-P. Correa-Baena, C. R. Carmona, G. Richardson, J. M. Foster, F. de Angelis, J. M. Ball, A. Petrozza, N. Mine, M. K. Nazeeruddin, W. Tress, M. Grätzel, U. Steiner, A. Hagfeldt, and A. Abate, "Migration of cations induces reversible performance losses over day/night cycling in perovskite solar cells," *Energy & Environmental Science*, vol. 10, no. 2, pp. 604–613, 2017.

[41] E. T. Hoke, D. J. Slotcavage, E. R. Dohner, A. R. Bowring, H. I. Karunadasa, and M. D. McGehee, "Reversible photo-induced trap formation in mixed-halide hybrid perovskites for photovoltaics," *Chemical Science*, vol. 6, no. 1, pp. 613–617, 2015.

[42] T. Leijtens, G. E. Eperon, S. Pathak, A. Abate, M. M. Lee, and H. J. Snaith, "Overcoming ultraviolet light instability of sensitized TiO(2) with meso-superstructured organometal tri-halide perovskite solar cells," (eng), *Nature communications*, vol. 4, p. 2885, 2013.

[43] M. Saliba, M. Stolterfoht, C. M. Wolff, D. Neher, and A. Abate, "Measuring Aging Stability of Perovskite Solar Cells," *Joule*, vol. 2, no. 6, pp. 1019–1024, 2018.

[44] Dane W. deQuilettes, Sarah M. Vorpahl, Samuel D. Stranks, Hirokazu Nagaoka, Giles E. Eperon, Mark E. Ziffer, Henry J. Snaith, David S. Ginger, "Impact of microstructure on local carrier lifetime in perovskite solar cells," *Science*, vol. 348, no. 6235, pp. 683–686, 2015.

[45] G. E. Eperon, D. Moerman, and D. S. Ginger, "Anticorrelation between Local Photoluminescence and Photocurrent Suggests Variability in Contact to Active Layer in Perovskite Solar Cells," (eng), *ACS nano*, vol. 10, no. 11, pp. 10258–10266, 2016.

[46] S. Braunger, L. E. Mundt, C. M. Wolff, M. Mews, C. Rehermann, M. Jošt, A. Tejada, D. Eisenhauer, C. Becker, J. A. Guerra, E. Unger, L. Korte, D. Neher,

M. C. Schubert, B. Rech, and S. Albrecht, “Cs x FA 1– x Pb(I 1– y Br y) 3 Perovskite Compositions: The Appearance of Wrinkled Morphology and its Impact on Solar Cell Performance,” *Journal of Physical Chemistry C*, vol. 122, no. 30, pp. 17123–17135, 2018.

[47] D. W. deQuilettes, S. Koch, S. Burke, R. K. Paranji, A. J. Shropshire, M. E. Ziffer, and D. S. Ginger, “Photoluminescence Lifetimes Exceeding 8 μs and Quantum Yields Exceeding 30% in Hybrid Perovskite Thin Films by Ligand Passivation,” *ACS Energy Letters*, vol. 1, no. 2, pp. 438–444, 2016.

[48] D. W. deQuilettes, W. Zhang, V. M. Burlakov, D. J. Graham, T. Leijtens, A. Osherov, V. Bulovic, H. J. Snaith, D. S. Ginger, and S. D. Stranks, “Photo-induced halide redistribution in organic-inorganic perovskite films,” (eng), *Nature communications*, vol. 7, p. 11683, 2016.

[49] G. El-Hajje, C. Momblona, L. Gil-Escrig, J. Ávila, T. Guillemot, J.-F. Guillemoles, M. Sessolo, H. J. Bolink, and L. Lombez, “Quantification of spatial inhomogeneity in perovskite solar cells by hyperspectral luminescence imaging,” *Energy & Environmental Science*, vol. 9, no. 7, pp. 2286–2294, 2016.

[50] X. Fu, D. A. Jacobs, F. J. Beck, T. Duong, H. Shen, K. R. Catchpole, and T. P. White, “Photoluminescence study of time- and spatial-dependent light induced trap de-activation in CH3NH3PbI3 perovskite films,” (eng), *Physical Chemistry Chemical Physics*, vol. 18, no. 32, pp. 22557–22564, 2016.

[51] Z. Hameiri, A. Mahboubi Soufiani, M. K. Juhl, L. Jiang, F. Huang, Y.-B. Cheng, H. Kampwerth, J. W. Weber, M. A. Green, and T. Trupke, “Photoluminescence and electroluminescence imaging of perovskite solar cells,” *Progress in Photovoltaics*, vol. 23, no. 12, pp. 1697–1705, 2015.

[52] L. E. Mundt, F. D. Heinz, S. Albrecht, M. Mundus, M. Saliba, J. P. Correa-Baena, E. H. Anaraki, L. Korte, M. Gratzel, A. Hagfeldt, B. Rech, M. C. Schubert, and S. W. Glunz, “Nondestructive Probing of Perovskite Silicon Tandem Solar Cells Using Multiwavelength Photoluminescence Mapping,” *IEEE Journal of Photovoltaics*, vol. 7, no. 4, pp. 1081–1086, 2017.

[53] R. Sheng, X. Wen, S. Huang, X. Hao, S. Chen, Y. Jiang, X. Deng, M. A. Green, and Ho-Baillie, A. W. Y., “Photoluminescence characterisations of a dynamic aging process of organic–inorganic CH 3 NH 3 PbBr 3 perovskite,” *Nanoscale*, vol. 8, no. 4, pp. 1926–1931, 2016.

[54] Z. Song, A. Abate, S. C. Watthage, G. K. Liyanage, A. B. Phillips, U. Steiner, M. Graetzel, and M. J. Heben, “Perovskite Solar Cell Stability in Humid Air: Partially Reversible Phase Transitions in the PbI 2 -CH 3 NH 3 I-H 2 O System,” *Advanced Energy Materials*, vol. 6, no. 19, p. 1600846, 2016.

[55] A. M. Soufiani, Z. Hameiri, S. Meyer, S. Lim, M. J. Y. Tayebjee, J. S. Yun, A. Ho-Baillie, G. J. Conibeer, L. Spiccia, and M. A. Green, "Lessons Learnt from Spatially Resolved Electro- and Photoluminescence Imaging: Interfacial Delamination in CH 3 NH 3 PbI 3 Planar Perovskite Solar Cells upon Illumination," *Advanced Energy Materials*, vol. 49, p. 1602111, 2016.

[56] A. M. Soufiani, Tayebjee, Murad J. Y., S. Meyer, A. Ho-Baillie, J. Sung Yun, R. W. MacQueen, L. Spiccia, M. A. Green, and Z. Hameiri, "Electro- and photoluminescence imaging as fast screening technique of the layer uniformity and device degradation in planar perovskite solar cells," *Journal of applied physics*, vol. 120, no. 3, p. 35702, 2016.

[57] M. Vrućinić, C. Matthiesen, A. Sadhanala, G. Divitini, S. Cacovich, S. E. Dutton, C. Ducati, M. Atatüre, H. Snaith, R. H. Friend, H. Sirringhaus, and F. Deschler, "Local Versus Long-Range Diffusion Effects of Photoexcited States on Radiative Recombination in Organic-Inorganic Lead Halide Perovskites," *Advanced Science*, vol. 2, no. 9, p. 1500136, 2015.

[58] D. Walter, Y. Wu, T. Duong, J. Peng, L. Jiang, K. C. Fong, and K. Weber, "On the Use of Luminescence Intensity Images for Quantified Characterization of Perovskite Solar Cells: Spatial Distribution of Series Resistance," *Advanced Energy Materials*, vol. 8, no. 2, p. 1701522, 2018.

[59] M. Yang, Y. Zeng, Z. Li, D. H. Kim, C.-S. Jiang, J. van de Lagemaat, and K. Zhu, "Do grain boundaries dominate non-radiative recombination in CH3NH3PbI3 perovskite thin films?," (eng), *Physical Chemistry Chemical Physics*, vol. 19, no. 7, pp. 5043–5050, 2017.

[60] D. Yamashita, T. Handa, T. Ihara, H. Tahara, A. Shimazaki, A. Wakamiya, and Y. Kanemitsu, "Charge Injection at the Heterointerface in Perovskite CH3NH3PbI3 Solar Cells Studied by Simultaneous Microscopic Photoluminescence and Photocurrent Imaging Spectroscopy," (eng), *The Journal of Physical Chemistry Letters*, vol. 7, no. 16, pp. 3186–3191, 2016.

[61] P. Würfel, *Physics of solar cells - from basic principles to advanced concepts*, 2nd ed. Weinheim: Wiley-VCH Verlag GmbH & Co. KGaA, 2009.

[62] M. A. Green, A. Ho-Baillie, and H. J. Snaith, "The emergence of perovskite solar cells," *Nature Photonics*, vol. 8, no. 7, pp. 506–514, 2014.

[63] R. N. Hall, "Germanium rectifier characteristics," *Physical Review*, no. 83, p. 228, 1951.

[64] W. Shockley and Read, W. T. Jr., "Statistics of the recombinations of holes and electrons," *Physical Review*, vol. 87, no. 5, pp. 835–842, 1952.

[65] M. Jošt, E. Köhnen, A. Morales Vilches, B. Lipovšek, K. Jäger, B. Macco, A. Al-Ashouri, J. Krc, L. Korte, B. Rech, R. Schlatmann, M. Topic, B. Stannowski, and S. Albrecht, "Textured interfaces in monolithic perovskite/silicon tandem solar cells: Advanced light management for improved efficiency and energy yield," *Energy & Environmental Science*, 2019.

[66] M. A. Green, *Solar cells: operating principles, technology and system applications*. Kensington: The University of New South Wales, 1998.

[67] W. Shockley and H. J. Queisser, "Detailed Balance Limit of Efficiency of p-n Junction Solar Cells," *Journal of applied physics*, vol. 32, no. 3, p. 510, 1961.

[68] S. Schafer and R. Brendel, "Accurate Calculation of the Absorptance Enhances Efficiency Limit of Crystalline Silicon Solar Cells With Lambertian Light Trapping," *IEEE Journal of Photovoltaics*, vol. 8, no. 4, pp. 1156–1158, 2018.

[69] A. de Vos, "Detailed balance limit of the efficiency of tandem solar cells," *Journal of Physics D: Applied Physics*, vol. 13, no. 5, pp. 839–846, 1980.

[70] R. Cariou, J. Benick, F. Feldmann, O. Höhn, H. Hauser, P. Beutel, N. Razek, M. Wimplinger, B. Bläsi, D. Lackner, M. Hermle, G. Siefer, S. W. Glunz, A. W. Bett, and F. Dimroth, "III–V-on-silicon solar cells reaching 33% photoconversion efficiency in two-terminal configuration," *Nature Energy*, vol. 17, p. 183, 2018.

[71] *Count Lev Alekseyevich von Perovski.* [Online] Available: http://deduhova.ru/statesman/lev-alekseevich-perovskij/. Accessed on: Sep. 03 2018.

[72] Rob Lavinsky & irocks.com, *Perovskite : CaTiO3.* [Online] Available: https://www.mindat.org/photo-155026.html.

[73] Rudolph Hoffmann [Public domain], via Wikimedia Commons, *Gustav Rose Litho.* [Online] Available: https://commons.wikimedia.org/wiki/File:Gustav_Rose_Litho.jpg.

[74] A. Kojima, K. Teshima, Y. Shirai, and T. Miyasaka, "Organometal halide perovskites as visible-light sensitizers for photovoltaic cells," (eng), *Journal of the American Chemical Society*, vol. 131, no. 17, pp. 6050–6051, 2009.

[75] M. M. Lee, J. Teuscher, T. Miyasaka, T. N. Murakami, and H. J. Snaith, "Efficient hybrid solar cells based on meso-superstructured organometal halide perovskites," (eng), *Science*, vol. 338, no. 6107, pp. 643–647, 2012.

[76] H.-S. Kim, C.-R. Lee, J.-H. Im, K.-B. Lee, T. Moehl, A. Marchioro, S.-J. Moon, R. Humphry-Baker, J.-H. Yum, J. E. Moser, M. Gratzel, and N.-G. Park, "Lead iodide perovskite sensitized all-solid-state submicron thin film mesoscopic solar

cell with efficiency exceeding 9%," (eng), *Scientific Reports*, vol. 2, p. 591, 2012.

[77] N.-G. Park, M. Grätzel, and T. Miyasaka, *Organic-Inorganic Halide Perovskite Photovoltaics: From Fundamentals to Device Architectures*. Cham: Springer International Publishing, 2016.

[78] V. M. Goldschmidt, "Die Gesetze der Krystallochemie," *Die Naturwissenschaften*, vol. 14, no. 21, pp. 477–485, 1926.

[79] T. Sato, S. Takagi, S. Deledda, B. C. Hauback, and S.-i. Orimo, "Extending the applicability of the Goldschmidt tolerance factor to arbitrary ionic compounds," *Scientific Reports*, vol. 6, 23592 EP -, 2016.

[80] Z. Li, M. Yang, J.-S. Park, S.-H. Wei, J. J. Berry, and K. Zhu, "Stabilizing Perovskite Structures by Tuning Tolerance Factor: Formation of Formamidinium and Cesium Lead Iodide Solid-State Alloys," *Chemistry of Materials*, vol. 28, no. 1, pp. 284–292, 2016.

[81] H. Tsai, R. Asadpour, J.-C. Blancon, C. C. Stoumpos, O. Durand, J. W. Strzalka, B. Chen, R. Verduzco, P. M. Ajayan, S. Tretiak, J. Even, M. A. Alam, M. G. Kanatzidis, W. Nie, and A. D. Mohite, "Light-induced lattice expansion leads to high-efficiency perovskite solar cells," (eng), *Science*, vol. 360, no. 6384, pp. 67–70, 2018.

[82] S. Boyer-Richard, C. Katan, B. Traoré, R. Scholz, J.-M. Jancu, and J. Even, "Symmetry-Based Tight Binding Modeling of Halide Perovskite Semiconductors," (eng), *The Journal of Physical Chemistry Letters*, vol. 7, no. 19, pp. 3833–3840, 2016.

[83] S. X. Tao, X. Cao, and P. A. Bobbert, "Accurate and efficient band gap predictions of metal halide perovskites using the DFT-1/2 method: GW accuracy with DFT expense," *Scientific Reports*, vol. 7, no. 1, p. 14386, 2017.

[84] Le Zhang, W. Geng, C.-J. Tong, X. Chen, T. Cao, and M. Chen, "Strain induced electronic structure variation in methyl-ammonium lead iodide perovskite," *Scientific Reports*, vol. 8, no. 1, p. 7760, 2018.

[85] C. Grote and R. F. Berger, "Strain Tuning of Tin–Halide and Lead–Halide Perovskites: A First-Principles Atomic and Electronic Structure Study," *Journal of Physical Chemistry C*, vol. 119, no. 40, pp. 22832–22837, 2015.

[86] J.-P. Correa-Baena, A. Abate, M. Saliba, W. Tress, T. Jesper Jacobsson, M. Grätzel, and A. Hagfeldt, "The rapid evolution of highly efficient perovskite solar cells," *Energy & Environmental Science*, vol. 10, no. 3, pp. 710–727, 2017.

[87] Y. Hu, E. M. Hutter, P. Rieder, I. Grill, J. Hanisch, M. F. Aygüler, A. G. Hufnagel, M. Handloser, T. Bein, A. Hartschuh, K. Tvingstedt, V. Dyakonov, A.

Baumann, T. J. Savenije, M. L. Petrus, and P. Docampo, “Understanding the Role of Cesium and Rubidium Additives in Perovskite Solar Cells: Trap States, Charge Transport, and Recombination,” *Advanced Energy Materials*, vol. 8, no. 16, p. 1703057, 2018.

[88] Z. Xiao, Q. Dong, C. Bi, Y. Shao, Y. Yuan, and J. Huang, “Solvent annealing of perovskite-induced crystal growth for photovoltaic-device efficiency enhancement,” (eng), *Advanced Materials*, vol. 26, no. 37, pp. 6503–6509, 2014.

[89] M. Yang, T. Zhang, P. Schulz, Z. Li, G. Li, D. H. Kim, N. Guo, J. J. Berry, K. Zhu, and Y. Zhao, “Facile fabrication of large-grain CH3NH3PbI3−xBrx films for high-efficiency solar cells via CH3NH3Br-selective Ostwald ripening,” *Nature communications*, vol. 7, 12305 EP -, 2016.

[90] J. Cui, H. Yuan, J. Li, X. Xu, Y. Shen, H. Lin, and M. Wang, “Recent progress in efficient hybrid lead halide perovskite solar cells,” (eng), *Science and technology of advanced materials*, vol. 16, no. 3, p. 36004, 2015.

[91] S. de Wolf, J. Holovsky, S.-J. Moon, P. Löper, B. Niesen, M. Ledinsky, F.-J. Haug, J.-H. Yum, and C. Ballif, “Organometallic Halide Perovskites: Sharp Optical Absorption Edge and Its Relation to Photovoltaic Performance,” (eng), *The Journal of Physical Chemistry Letters*, vol. 5, no. 6, pp. 1035–1039, 2014.

[92] A. Sadhanala, A. Kumar, S. Pathak, A. Rao, U. Steiner, N. C. Greenham, H. J. Snaith, and R. H. Friend, “Electroluminescence from Organometallic Lead Halide Perovskite-Conjugated Polymer Diodes,” *Advanced Electronic Materials*, vol. 1, no. 3, p. 1500008, 2015.

[93] F. Brivio, K. T. Butler, A. Walsh, and M. van Schilfgaarde, “Relativistic quasiparticle self-consistent electronic structure of hybrid halide perovskite photovoltaic absorbers,” *Physical Review B*, vol. 89, no. 15, 2014.

[94] C. C. Stoumpos, C. D. Malliakas, and M. G. Kanatzidis, “Semiconducting Tin and Lead Iodide Perovskites with Organic Cations: Phase Transitions, High Mobilities, and Near-Infrared Photoluminescent Properties,” *Inorganic Chemistry*, vol. 52, no. 15, pp. 9019–9038, 2013.

[95] P. Umari, E. Mosconi, and F. de Angelis, “Relativistic GW calculations on CH3NH3PbI3 and CH3NH3SnI3 Perovskites for Solar Cell Applications,” *Scientific Reports*, vol. 4, 4467 EP -, 2014.

[96] E. M. Hutter, M. C. Gelvez-Rueda, A. Osherov, V. Bulovic, F. C. Grozema, S. D. Stranks, and T. J. Savenije, “Direct-indirect character of the bandgap in methylammonium lead iodide perovskite,” (eng), *Nature materials*, vol. 16, no. 1, pp. 115–120, 2017.

[97] T. Wang, B. Daiber, J. M. Frost, S. A. Mann, E. C. Garnett, A. Walsh, and B. Ehrler, "Indirect to direct bandgap transition in methylammonium lead halide perovskite," *Energy & Environmental Science*, vol. 10, no. 2, pp. 509–515, 2017.

[98] C. L. Davies, M. R. Filip, J. B. Patel, T. W. Crothers, C. Verdi, A. D. Wright, R. L. Milot, F. Giustino, M. B. Johnston, and L. M. Herz, "Bimolecular recombination in methylammonium lead triiodide perovskite is an inverse absorption process," *Nature communications*, vol. 9, no. 1, p. 293, 2018.

[99] T. M. Brenner, D. A. Egger, L. Kronik, G. Hodes, and D. Cahen, "Hybrid organic—inorganic perovskites: Low-cost semiconductors with intriguing charge-transport properties," *Nature Reviews Materials*, vol. 1, 15007 EP -, 2016.

[100] K. L. Shaklee and R. E. Nahory, "Valley-Orbit Splitting of Free Excitons?: The Absorption Edge of Si," *Physical Review Letters*, vol. 24, no. 17, pp. 942–945, 1970.

[101] G. W. Fehrenbach, W. Schäfer, and R. G. Ulbrich, "Excitonic Versus Plasma Screening in Highly Excited Gallium Arsenide," in *High Excitation and Short Pulse Phenomena*, M. H. Pilkuhn, Ed., Burlington: Elsevier Science, 2012, pp. 154–161.

[102] N. C. Giebink, G. P. Wiederrecht, M. R. Wasielewski, and S. R. Forrest, "Thermodynamic efficiency limit of excitonic solar cells," *Physical Review B*, vol. 83, no. 19, 2011.

[103] M. Hirasawa, T. Ishihara, T. Goto, K. Uchida, and N. Miura, "Magnetoabsorption of the lowest exciton in perovskite-type compound (CH3NH3)PbI3," *Physica B: Condensed Matter*, vol. 201, pp. 427–430, 1994.

[104] T. Ishihara, "Optical properties of PbI-based perovskite structures," *Journal of Luminescence*, vol. 60-61, pp. 269–274, 1994.

[105] Q. Lin, A. Armin, Nagiri, Ravi Chandra Raju, P. L. Burn, and P. Meredith, "Electro-optics of perovskite solar cells," *Nature Photonics*, vol. 9, 106 EP -, 2014.

[106] M. Saba, M. Cadelano, D. Marongiu, F. Chen, V. Sarritzu, N. Sestu, C. Figus, M. Aresti, R. Piras, A. Geddo Lehmann, C. Cannas, A. Musinu, F. Quochi, A. Mura, and G. Bongiovanni, "Correlated electron–hole plasma in organometal perovskites," *Nature communications*, vol. 5, p. 5049, 2014.

[107] K. Tanaka, T. Takahashi, T. Ban, T. Kondo, K. Uchida, and N. Miura, "Comparative study on the excitons in lead-halide-based perovskite-type crystals

CH3NH3PbBr3 CH3NH3PbI3," *Solid State Communications*, vol. 127, no. 9-10, pp. 619–623, 2003.

[108] A. Miyata, A. Mitioglu, P. Plochocka, O. Portugall, J. T.-W. Wang, S. D. Stranks, H. J. Snaith, and R. J. Nicholas, "Direct measurement of the exciton binding energy and effective masses for charge carriers in organic–inorganic tri-halide perovskites," *Nature Physics*, vol. 11, no. 7, pp. 582–587, 2015.

[109] K. Galkowski, A. Mitioglu, A. Miyata, P. Plochocka, O. Portugall, G. E. Eperon, J. T.-W. Wang, T. Stergiopoulos, S. D. Stranks, H. J. Snaith, and R. J. Nicholas, "Determination of the exciton binding energy and effective masses for methylammonium and formamidinium lead tri-halide perovskite semiconductors," *Energy & Environmental Science*, vol. 9, no. 3, pp. 962–970, 2016.

[110] S. D. Stranks, V. M. Burlakov, T. Leijtens, J. M. Ball, A. Goriely, and H. J. Snaith, "Recombination Kinetics in Organic-Inorganic Perovskites: Excitons, Free Charge, and Subgap States," *Physical Review Applied*, vol. 2, no. 3, 2014.

[111] V. D'Innocenzo, G. Grancini, M. J. P. Alcocer, A. R. S. Kandada, S. D. Stranks, M. M. Lee, G. Lanzani, H. J. Snaith, and A. Petrozza, "Excitons versus free charges in organo-lead tri-halide perovskites," (eng), *Nature communications*, vol. 5, p. 3586, 2014.

[112] S. D. Stranks, G. E. Eperon, G. Grancini, C. Menelaou, Alcocer, M. J. P., T. Leijtens, L. M. Herz, A. Petrozza, and H. J. Snaith, "Electron-Hole Diffusion Lengths Exceeding 1 Micrometer in an Organometal Trihalide Perovskite Absorber," *Science*, vol. 342, no. 6156, pp. 341–344, 2013.

[113] G. Xing, N. Mathews, S. Sun, S. S. Lim, Y. M. Lam, M. Grätzel, S. Mhaisalkar, and T. C. Sum, "Long-range balanced electron- and hole-transport lengths in organic-inorganic CH3NH3PbI3," (eng), *Science*, vol. 342, no. 6156, pp. 344–347, 2013.

[114] C. Wehrenfennig, G. E. Eperon, M. B. Johnston, H. J. Snaith, and L. M. Herz, "High Charge Carrier Mobilities and Lifetimes in Organolead Trihalide Perovskites," *Advanced Materials*, vol. 26, no. 10, pp. 1584–1589, 2014.

[115] E. Edri, S. Kirmayer, S. Mukhopadhyay, K. Gartsman, G. Hodes, and D. Cahen, "Elucidating the charge carrier separation and working mechanism of CH3NH3PbI3−xClx perovskite solar cells," *Nature communications*, vol. 5, 3461 EP -, 2014.

[116] Wanyi Nie, Hsinhan Tsai, Reza Asadpour, Jean-Christophe Blancon, Amanda J. Neukirch, Gautam Gupta, Jared J. Crochet, Manish Chhowalla, Sergei Tretiak, Muhammad A. Alam, Hsing-Lin Wang, Aditya D. Mohite, "High-efficiency

solution-processed perovskite solar cells with millimeter-scale grains," *Science*, vol. 347, no. 6221, pp. 522–525, 2015.

[117] Dong Shi, Valerio Adinolfi, Riccardo Comin, Mingjian Yuan, Erkki Alarousu, Andrei Buin, Yin Chen, Sjoerd Hoogland, Alexander Rothenberger, Khabiboulakh Katsiev, Yaroslav Losovyj, Xin Zhang, Peter A. Dowben, Omar F. Mohammed, Edward H. Sargent, Osman M. Bakr, "Low trap-state density and long Low trap-state density and long carrier diffusion in organolead trihalide perovskite single crystals," *Science*, vol. 347, no. 6221, pp. 519–522, 2015.

[118] G. E. Eperon, V. M. Burlakov, P. Docampo, A. Goriely, and H. J. Snaith, "Morphological Control for High Performance, Solution-Processed Planar Heterojunction Perovskite Solar Cells," *Advanced Functional Materials*, vol. 24, no. 1, pp. 151–157, 2014.

[119] J. M. Ball, M. M. Lee, A. Hey, and H. J. Snaith, "Low-temperature processed meso-superstructured to thin-film perovskite solar cells," *Energy & Environmental Science*, vol. 6, no. 6, p. 1739, 2013.

[120] Q. Chen, H. Zhou, Z. Hong, S. Luo, H.-S. Duan, H.-H. Wang, Y. Liu, G. Li, and Y. Yang, "Planar heterojunction perovskite solar cells via vapor-assisted solution process," (ENG), *Journal of the American Chemical Society*, vol. 136, no. 2, pp. 622–625, 2014.

[121] D. Liu and T. L. Kelly, "Perovskite solar cells with a planar heterojunction structure prepared using room-temperature solution processing techniques," *Nature Photonics*, vol. 8, no. 2, pp. 133–138, 2013.

[122] M. Liu, M. B. Johnston, and H. J. Snaith, "Efficient planar heterojunction perovskite solar cells by vapour deposition," *Nature*, vol. 501, no. 7467, pp. 395–398, 2013.

[123] Y. Shao, Z. Xiao, C. Bi, Y. Yuan, and J. Huang, "Origin and elimination of photocurrent hysteresis by fullerene passivation in CH3NH3PbI3 planar heterojunction solar cells," *Nature communications*, vol. 5, 5784 EP -, 2014.

[124] L. M. Herz, "Charge-Carrier Mobilities in Metal Halide Perovskites: Fundamental Mechanisms and Limits," *ACS Energy Letters*, vol. 2, no. 7, pp. 1539–1548, 2017.

[125] J. S. Manser and P. V. Kamat, "Band filling with free charge carriers in organometal halide perovskites," *Nature Photonics*, vol. 8, no. 9, pp. 737–743, 2014.

[126] R. L. Milot, G. E. Eperon, H. J. Snaith, M. B. Johnston, and L. M. Herz, "Temperature-Dependent Charge-Carrier Dynamics in CH 3 NH 3 PbI 3

Perovskite Thin Films," *Advanced Functional Materials*, vol. 25, no. 39, pp. 6218–6227, 2015.

[127] C. Wehrenfennig, M. Liu, H. J. Snaith, M. B. Johnston, and L. M. Herz, "Charge-carrier dynamics in vapour-deposited films of the organolead halide perovskite CH 3 NH 3 PbI 3−x Cl x," *Energy & Environmental Science*, vol. 7, no. 7, pp. 2269–2275, 2014.

[128] Y. Yamada, T. Nakamura, M. Endo, A. Wakamiya, and Y. Kanemitsu, "Photocarrier Recombination Dynamics in Perovskite CH 3 NH 3 PbI 3 for Solar Cell Applications," *Journal of the American Chemical Society*, vol. 136, no. 33, pp. 11610–11613, 2014.

[129] F. Deschler, M. Price, S. Pathak, L. E. Klintberg, D.-D. Jarausch, R. Higler, S. Hüttner, T. Leijtens, S. D. Stranks, H. J. Snaith, M. Atatüre, R. T. Phillips, and R. H. Friend, "High Photoluminescence Efficiency and Optically Pumped Lasing in Solution-Processed Mixed Halide Perovskite Semiconductors," *The Journal of Physical Chemistry Letters*, vol. 5, no. 8, pp. 1421–1426, 2014.

[130] T. J. Savenije, C. S. Ponseca, L. Kunneman, M. Abdellah, K. Zheng, Y. Tian, Q. Zhu, S. E. Canton, I. G. Scheblykin, T. Pullerits, A. Yartsev, and V. Sundström, "Thermally Activated Exciton Dissociation and Recombination Control the Carrier Dynamics in Organometal Halide Perovskite," (eng), *The Journal of Physical Chemistry Letters*, vol. 5, no. 13, pp. 2189–2194, 2014.

[131] Y. Bi, E. M. Hutter, Y. Fang, Q. Dong, J. Huang, and T. J. Savenije, "Charge Carrier Lifetimes Exceeding 15 μs in Methylammonium Lead Iodide Single Crystals," *The Journal of Physical Chemistry Letters*, vol. 7, no. 5, pp. 923–928, 2016.

[132] D. Pérez-del-Rey, D. Forgács, E. M. Hutter, T. J. Savenije, D. Nordlund, P. Schulz, J. J. Berry, M. Sessolo, and H. J. Bolink, "Strontium Insertion in Methylammonium Lead Iodide: Long Charge Carrier Lifetime and High Fill-Factor Solar Cells," (eng), *Advanced Materials*, vol. 28, no. 44, pp. 9839–9845, 2016.

[133] Q. Wang, Q. Dong, T. Li, A. Gruverman, and J. Huang, "Thin Insulating Tunneling Contacts for Efficient and Water-Resistant Perovskite Solar Cells," (eng), *Advanced Materials*, vol. 28, no. 31, pp. 6734–6739, 2016.

[134] J. M. Richter, M. Abdi-Jalebi, A. Sadhanala, M. Tabachnyk, J. P.H. Rivett, L. M. Pazos-Outón, K. C. Gödel, M. Price, F. Deschler, and R. H. Friend, "Enhancing photoluminescence yields in lead halide perovskites by photon recycling and light out-coupling," *Nature communications*, vol. 7, 13941 EP -, 2016.

[135] W. Tress, N. Marinova, T. Moehl, S. M. Zakeeruddin, M. K. Nazeeruddin, and M. Grätzel, "Understanding the rate-dependent J–V hysteresis, slow time component, and aging in CH 3 NH 3 PbI 3 perovskite solar cells: The role of a compensated electric field," *Energy & Environmental Science*, vol. 8, no. 3, pp. 995–1004, 2015.

[136] H.-W. Chen, N. Sakai, M. Ikegami, and T. Miyasaka, "Emergence of Hysteresis and Transient Ferroelectric Response in Organo-Lead Halide Perovskite Solar Cells," (eng), *The Journal of Physical Chemistry Letters*, vol. 6, no. 1, pp. 164–169, 2015.

[137] N. K. Elumalai and A. Uddin, "Hysteresis in organic-inorganic hybrid perovskite solar cells," *Solar Energy Materials & Solar Cells*, vol. 157, pp. 476–509, 2016.

[138] Y. Yuan, T. Li, Q. Wang, J. Xing, A. Gruverman, and J. Huang, "Anomalous photovoltaic effect in organic-inorganic hybrid perovskite solar cells," (eng), *Science advances*, vol. 3, no. 3, e1602164, 2017.

[139] F. Huang, L. Jiang, A. R. Pascoe, Y. Yan, U. Bach, L. Spiccia, and Y.-B. Cheng, "Fatigue behavior of planar CH3NH3PbI3 perovskite solar cells revealed by light on/off diurnal cycling," *Nano Energy*, vol. 27, pp. 509–514, 2016.

[140] W. Nie, J.-C. Blancon, A. J. Neukirch, K. Appavoo, H. Tsai, M. Chhowalla, M. A. Alam, M. Y. Sfeir, C. Katan, J. Even, S. Tretiak, J. J. Crochet, G. Gupta, and A. D. Mohite, "Light-activated photocurrent degradation and self-healing in perovskite solar cells," *Nature communications*, vol. 7, 11574 EP -, 2016.

[141] A. Walsh and S. D. Stranks, "Taking Control of Ion Transport in Halide Perovskite Solar Cells," *ACS Energy Letters*, vol. 3, no. 8, pp. 1983–1990, 2018.

[142] G. Y. Kim, A. Senocrate, T.-Y. Yang, G. Gregori, M. Grätzel, and J. Maier, "Large tunable photoeffect on ion conduction in halide perovskites and implications for photodecomposition," *Nature materials*, vol. 17, no. 5, pp. 445–449, 2018.

[143] C. Eames, J. M. Frost, Barnes, Piers R. F., B. C. O'Regan, A. Walsh, and M. S. Islam, "Ionic transport in hybrid lead iodide perovskite solar cells," *Nature communications*, vol. 6, p. 7497, 2015.

[144] J. Haruyama, K. Sodeyama, L. Han, and Y. Tateyama, "First-Principles Study of Ion Diffusion in Perovskite Solar Cell Sensitizers," (eng), *Journal of the American Chemical Society*, vol. 137, no. 32, pp. 10048–10051, 2015.

[145] G. E. Eperon and D. S. Ginger, "B-Site Metal Cation Exchange in Halide Perovskites," *ACS Energy Letters*, vol. 2, no. 5, pp. 1190–1196, 2017.

[146] G. E. Eperon, C. E. Beck, and H. J. Snaith, “Cation exchange for thin film lead iodide perovskite interconversion,” *Materials Horizons*, vol. 3, no. 1, pp. 63–71, 2016.

[147] S. J. Yoon, S. Draguta, J. S. Manser, O. Sharia, W. F. Schneider, M. Kuno, and P. V. Kamat, “Tracking Iodide and Bromide Ion Segregation in Mixed Halide Lead Perovskites during Photoirradiation,” *ACS Energy Letters*, vol. 1, no. 1, pp. 290–296, 2016.

[148] Y. Yuan and J. Huang, “Ion Migration in Organometal Trihalide Perovskite and Its Impact on Photovoltaic Efficiency and Stability,” (eng), *Accounts of chemical research*, vol. 49, no. 2, pp. 286–293, 2016.

[149] D. W. deQuilettes, S. Jariwala, S. Burke, M. E. Ziffer, J. T.-W. Wang, H. J. Snaith, and D. S. Ginger, “Tracking Photoexcited Carriers in Hybrid Perovskite Semiconductors: Trap-Dominated Spatial Heterogeneity and Diffusion,” (eng), *ACS nano*, vol. 11, no. 11, pp. 11488–11496, 2017.

[150] Z. H. Bakr, Q. Wali, A. Fakharuddin, L. Schmidt-Mende, T. M. Brown, and R. Jose, “Advances in hole transport materials engineering for stable and efficient perovskite solar cells,” *Nano Energy*, vol. 34, pp. 271–305, 2017.

[151] M. Saliba, J.-P. Correa-Baena, C. M. Wolff, M. Stolterfoht, N. Phung, S. Albrecht, D. Neher, and A. Abate, “How to Make over 20% Efficient Perovskite Solar Cells in Regular (n–i–p) and Inverted (p–i–n) Architectures,” *Chemistry of Materials*, vol. 30, no. 13, pp. 4193–4201, 2018.

[152] J. Burschka, N. Pellet, S.-J. Moon, R. Humphry-Baker, P. Gao, M. K. Nazeeruddin, and M. Grätzel, “Sequential deposition as a route to high-performance perovskite-sensitized solar cells,” *Nature*, vol. 499, no. 7458, pp. 316–319, 2013.

[153] P. Docampo, J. M. Ball, M. Darwich, G. E. Eperon, and H. J. Snaith, “Efficient organometal trihalide perovskite planar-heterojunction solar cells on flexible polymer substrates,” *Nature communications*, vol. 4, 2761 EP -, 2013.

[154] I. Almansouri, A. Ho-Baillie, and M. A. Green, “Ultimate efficiency limit of single-junction perovskite and dual-junction perovskite/silicon two-terminal devices,” *Japanese Journal of Applied Physics*, vol. 54, no. 8S1, p. 8, 2015.

[155] N. N. Lal, T. P. White, and K. R. Catchpole, “Optics and Light Trapping for Tandem Solar Cells on Silicon,” *IEEE Journal of Photovoltaics*, vol. 4, no. 6, pp. 1380–1386, 2014.

[156] T. P. White, N. N. Lal, and K. R. Catchpole, “Tandem Solar Cells Based on High-Efficiency c-Si Bottom Cells: Top Cell Requirements for >30% Efficiency,” *IEEE Journal of Photovoltaics*, vol. 4, no. 1, pp. 208–214, 2014.

[157] J. Werner, B. Niesen, and C. Ballif, “Perovskite/Silicon Tandem Solar Cells: Marriage of Convenience or True Love Story? - An Overview,” *Advanced Materials Interfaces*, vol. 9, p. 1700731, 2017.

[158] N. Tucher, O. Höhn, J. C. Goldschmidt, and B. Bläsi, “Optical modeling of structured silicon-based tandem solar cells and module stacks,” *Optics Express*, vol. 26, no. 18, A761, 2018.

[159] G. E. Eperon, T. Leijtens, K. A. Bush, R. Prasanna, T. Green, J. T.-W. Wang, D. P. McMeekin, G. Volonakis, R. L. Milot, R. May, A. Palmstrom, D. J. Slotcavage, R. A. Belisle, J. B. Patel, E. S. Parrott, R. J. Sutton, W. Ma, F. Moghadam, B. Conings, A. Babayigit, H.-G. Boyen, S. Bent, F. Giustino, L. M. Herz, M. B. Johnston, M. D. McGehee, and H. J. Snaith, “Perovskite-perovskite tandem photovoltaics with optimized bandgaps,” *Science*, 2016.

[160] D. Forgács, L. Gil-Escrig, D. Pérez-del-Rey, C. Momblona, J. Werner, B. Niesen, C. Ballif, M. Sessolo, and H. J. Bolink, “Efficient Monolithic Perovskite/Perovskite Tandem Solar Cells,” *Advanced Energy Materials*, vol. 348, p. 1602121, 2016.

[161] C.-Y. Chang, B.-C. Tsai, Y.-C. Hsiao, M.-Z. Lin, and H.-F. Meng, “Solution-Processed Conductive Interconnecting Layer for Highly-Efficient and Long-Term Stable Monolithic Perovskite Tandem Solar Cells,” *Nano Energy*, 2018.

[162] J. Werner, F. Sahli, F. Fu, J. J. Diaz Leon, A. Walter, B. A. Kamino, B. Niesen, S. Nicolay, Q. Jeangros, and C. Ballif, “Perovskite/Perovskite/Silicon Monolithic Triple-Junction Solar Cells with a Fully Textured Design,” *ACS Energy Letters*, vol. 3, no. 9, pp. 2052–2058, 2018.

[163] P. Gundel, F. D. Heinz, M. C. Schubert, J. A. Giesecke, and W. Warta, “Quantitative carrier lifetime measurement with micron resolution,” *Journal of applied physics*, vol. 108, no. 3, p. 33705, 2010.

[164] P. Gundel, M. Drießen, J. Bartsch, U. Jäger, D. Suwito, F. D. Heinz, W. Warta, and M. C. Schubert, “Comprehensive characterization of advanced cell concepts with sub-micron resolution,” in *Proceedings of the 26th European Photovoltaic Solar Energy Conference and Exhibition (EUPVSEC)*, Hamburg, Germany, 2011, pp. 250–256.

[165] P. Gundel, M. C. Schubert, F. D. Heinz, W. Kwapil, W. Warta, G. Martinez-Criado, M. Reiche, and E. R. Weber, “Impact of stress on the recombination at metal precipitates in silicon,” *J Appl Phys*, vol. 108, no. 10, p. 103707, 2010.

[166] P. Gundel, M. C. Schubert, W. Kwapil, J. Schön, M. Reiche, H. Savin, M. Yli-Koski, J. A. Sans, G. Martinez-Criado, W. Seifert, W. Warta, and E. R. Weber,

"Micro-photoluminescence spectroscopy on metal precipitates in silicon," *Physica Status Solidi RRL*, vol. 3, no. 7-8, pp. 230–232, 2009.

[167] P. Gundel, M. C. Schubert, and W. Warta, "Simultaneous stress and defect luminescence study on silicon," *Phys Status Solidi A*, vol. 207, no. 2, pp. 436–441, 2009.

[168] P. Gundel, M. C. Schubert, and W. Warta, "Simultaneous stress and defect luminescence study on silicon," *physica status solidi (a)*, vol. 207, no. 2, pp. 436–441, 2010.

[169] F. D. Heinz, *Microscopic Photoluminescence Spectroscopy on Silicon*. Stuttgart: Fraunhofer Verlag, 2017.

[170] F. D. Heinz, P. Gundel, W. Warta, and M. C. Schubert, "Doping Density in Silicon and Solar Cells Analyzed With Micrometer Resolution," *Ieee J Photovolt*, vol. PP, no. 99, pp. 1–7, 2012.

[171] F. D. Heinz, W. Warta, and M. C. Schubert, "Optimizing Micro Raman and PL Spectroscopy for Solar Cell Technological Assessment," *Energy Procedia*, vol. 27, pp. 208–213, 2012.

[172] B. Rezek, C. E. Nebel, and M. Stutzmann, "Laser beam induced currents in polycrystalline silicon thin films prepared by interference laser crystallization," *Journal of applied physics*, vol. 91, no. 7, pp. 4220–4228, 2002.

[173] M. Schwalm, C. Lange, W. W. Rühle, W. Stolz, K. Volz, and S. Chatterjee, "Characterization of solar cells by photocurrent spectroscopy and current-voltage characteristics with high spatial resolution," (eng), *Optics Express*, vol. 18, no. 6, pp. 6277–6287, 2010.

[174] M. de Vittorio, R. Cingolani, M. Mazzer, and D. B. Holt, "Sub-micron photocurrent mapping of heterostructures by micro-probe optical-beam induced current," *Review of Scientific Instruments*, vol. 70, no. 8, pp. 3429–3431, 1999.

[175] O. Breitenstein, W. Warta, and M. Langenkamp, *Lock-in Thermography*. Berlin, Heidelberg: Springer Berlin Heidelberg, 2010.

[176] O. Breitenstein, J. P. Rakotoniaina, van der Heide, A. S. H., and J. Carstensen, "Series resistance imaging in solar cells by lock-in thermography," *Prog Photovoltaics*, vol. 13, no. 8, pp. 645–660, 2005.

[177] H. Kampwerth, T. Trupke, J. W. Weber, and Y. Augarten, "Advanced luminescence based effective series resistance imaging of silicon solar cells," *Applied Physics Letters*, vol. 93, no. 202102, p. 202102, 2008.

[178] O. Breitenstein, "Local efficiency analysis of solar cells based on lock-in thermography," *Solar Energy Materials & Solar Cells*, vol. 107, pp. 381–389, 2012.

[179] O. Breitenstein, “Nondestructive local analysis of current–voltage characteristics of solar cells by lock-in thermography,” *Solar Energy Materials & Solar Cells*, vol. 95, no. 10, pp. 2933–2936, 2011.

[180] A. A. Bakulin, O. Selig, H. J. Bakker, Y. L. A. Rezus, C. Müller, T. Glaser, R. Lovrincic, Z. Sun, Z. Chen, A. Walsh, J. M. Frost, and T. L. C. Jansen, “Real-Time Observation of Organic Cation Reorientation in Methylammonium Lead Iodide Perovskites,” (eng), *The Journal of Physical Chemistry Letters*, vol. 6, no. 18, pp. 3663–3669, 2015.

[181] J. A. Aguiar, S. Wozny, T. G. Holesinger, T. Aoki, M. K. Patel, M. Yang, J. J. Berry, M. Al-Jassim, W. Zhou, and K. Zhu, “In situ investigation of the formation and metastability of formamidinium lead tri-iodide perovskite solar cells,” *Energy & Environmental Science*, vol. 9, no. 7, pp. 2372–2382, 2016.

[182] M. Alsari, O. Bikondoa, J. Bishop, M. Abdi-Jalebi, L. Y. Ozer, M. Hampton, P. Thompson, M. T. Hörantner, S. Mahesh, C. Greenland, J. E. Macdonald, G. Palmisano, H. J. Snaith, D. G. Lidzey, S. D. Stranks, R. H. Friend, and S. Lilliu, “In situ simultaneous photovoltaic and structural evolution of perovskite solar cells during film formation,” *Energy & Environmental Science*, vol. 11, no. 2, pp. 383–393, 2018.

[183] A. T. Barrows, S. Lilliu, A. J. Pearson, D. Babonneau, A. D. F. Dunbar, and D. G. Lidzey, “Monitoring the Formation of a CH 3 NH 3 PbI 3-x Cl x Perovskite during Thermal Annealing Using X-Ray Scattering,” *Advanced Functional Materials*, vol. 26, no. 27, pp. 4934–4942, 2016.

[184] J. L. Garrett, E. M. Tennyson, M. Hu, J. Huang, J. N. Munday, and M. S. Leite, “Real-Time Nanoscale Open-Circuit Voltage Dynamics of Perovskite Solar Cells,” (eng), *Nano letters*, vol. 17, no. 4, pp. 2554–2560, 2017.

[185] Q. Hu, L. Zhao, J. Wu, K. Gao, D. Luo, Y. Jiang, Z. Zhang, C. Zhu, E. Schaible, A. Hexemer, C. Wang, Y. Liu, W. Zhang, M. Grätzel, F. Liu, T. P. Russell, R. Zhu, and Q. Gong, “In situ dynamic observations of perovskite crystallisation and microstructure evolution intermediated from [PbI6]4− cage nanoparticles,” *Nature communications*, vol. 8, 15688 EP -, 2017.

[186] Q. Jeangros, M. Duchamp, J. Werner, M. Kruth, R. E. Dunin-Borkowski, B. Niesen, C. Ballif, and A. Hessler-Wyser, “In situ TEM analysis of organic-inorganic metal-halide perovskite solar cells under electrical bias,” (ENG), *Nano letters*, 2016.

[187] Y. Li, Z. Zhao, F. Lin, X. Cao, X. Cui, and J. Wei, “In Situ Observation of Crystallization of Methylammonium Lead Iodide Perovskite from Microdroplets,” (eng), *small*, vol. 13, no. 26, 2017.

[188] S. Lilliu, J. Griffin, A. T. Barrows, M. Alsari, B. Curzadd, T. G. Dane, O. Bikondoa, J. E. Macdonald, and D. G. Lidzey, "Grain rotation and lattice deformation during perovskite spray coating and annealing probed in situ by GI-WAXS," *Crystengcomm*, vol. 18, no. 29, pp. 5448–5455, 2016.

[189] K. Meng, L. Wu, Z. Liu, X. Wang, Q. Xu, Y. Hu, S. He, X. Li, T. Li, and G. Chen, "In Situ Real-Time Study of the Dynamic Formation and Conversion Processes of Metal Halide Perovskite Films," (eng), *Advanced Materials*, vol. 30, no. 11, 2018.

[190] T. Miyadera, Y. Shibata, T. Koganezawa, T. N. Murakami, T. Sugita, N. Tanigaki, and M. Chikamatsu, "Crystallization Dynamics of Organolead Halide Perovskite by Real-Time X-ray Diffraction," (eng), *Nano letters*, vol. 15, no. 8, pp. 5630–5634, 2015.

[191] D. T. Moore, H. Sai, K. W. Tan, D.-M. Smilgies, W. Zhang, H. J. Snaith, U. Wiesner, and L. A. Estroff, "Crystallization kinetics of organic-inorganic trihalide perovskites and the role of the lead anion in crystal growth," (eng), *Journal of the American Chemical Society*, vol. 137, no. 6, pp. 2350–2358, 2015.

[192] R. Munir, A. D. Sheikh, M. Abdelsamie, H. Hu, L. Yu, K. Zhao, T. Kim, O. E. Tall, R. Li, D.-M. Smilgies, and A. Amassian, "Hybrid Perovskite Thin-Film Photovoltaics: In Situ Diagnostics and Importance of the Precursor Solvate Phases," (eng), *Advanced Materials*, vol. 29, no. 2, 2017.

[193] K. W. Tan, D. T. Moore, M. Saliba, H. Sai, L. A. Estroff, T. Hanrath, H. J. Snaith, and U. Wiesner, "Thermally induced structural evolution and performance of mesoporous block copolymer-directed alumina perovskite solar cells," (eng), *ACS nano*, vol. 8, no. 5, pp. 4730–4739, 2014.

[194] A. Ummadisingu, L. Steier, J.-Y. Seo, T. Matsui, A. Abate, W. Tress, and M. Grätzel, "The effect of illumination on the formation of metal halide perovskite films," *Nature*, vol. 545, 208 EP -, 2017.

[195] S.-W. Lee, S. Kim, S. Bae, K. Cho, T. Chung, L. E. Mundt, S. Lee, S. Park, H. Park, M. C. Schubert, S. W. Glunz, Y. Ko, Y. Jun, Y. Kang, H.-S. Lee, and D. Kim, "UV Degradation and Recovery of Perovskite Solar Cells," (eng), *Scientific Reports*, vol. 6, p. 38150, 2016.

[196] Y. Zhong, R. Munir, J. Li, M.-C. Tang, M. R. Niazi, D.-M. Smilgies, K. Zhao, and A. Amassian, "Blade-Coated Hybrid Perovskite Solar Cells with Efficiency > 17%: An In Situ Investigation," *ACS Energy Letters*, vol. 3, no. 5, pp. 1078–1085, 2018.

[197] L. H. Rossander, T. T. Larsen-Olsen, H. F. Dam, T. M. Schmidt, M. Corazza, K. Norrman, I. Rajkovic, J. W. Andreasen, and F. C. Krebs, “In situ X-ray scattering of perovskite solar cell active layers roll-to-roll coated on flexible substrates,” *Crystengcomm*, vol. 18, no. 27, pp. 5083–5088, 2016.

[198] V. L. Pool, B. Dou, D. G. van Campen, T. R. Klein-Stockert, F. S. Barnes, S. E. Shaheen, M. I. Ahmad, van Hest, Maikel F. A. M., and M. F. Toney, “Thermal engineering of FAPbI3 perovskite material via radiative thermal annealing and in situ XRD,” *Nature communications*, vol. 8, 14075 EP -, 2017.

[199] J. J. van Franeker, K. H. Hendriks, B. J. Bruijnaers, M. W. G. M. Verhoeven, M. M. Wienk, and Janssen, René A. J., “Monitoring Thermal Annealing of Perovskite Solar Cells with In Situ Photoluminescence,” *Advanced Energy Materials*, vol. 2, p. 1601822, 2016.

[200] M. Anaya, J. F. Galisteo-Lopez, M. E. Calvo, C. Lopez, and H. Miguez, “Photophysical Analysis of the Formation of Organic-Inorganic Trihalide Perovskite Films: Identification and Characterization of Crystal Nucleation and Growth,” (eng), *The Journal of Physical Chemistry C*, vol. 120, no. 5, pp. 3071–3076, 2016.

[201] A. Dualeh, N. Tétreault, T. Moehl, P. Gao, M. K. Nazeeruddin, and M. Grätzel, “Effect of Annealing Temperature on Film Morphology of Organic-Inorganic Hybrid Pervoskite Solid-State Solar Cells,” *Advanced Functional Materials*, vol. 24, no. 21, pp. 3250–3258, 2014.

[202] W. Liu, L. Li, M. Chen, X. Ding, M. Wang, G. Liu, and X. Wang, “Nucleation mechanism of CH3NH3PbI3 with two-step method for rational design of high performance perovskite solar cells,” *Journal of Alloys and Compounds*, 2016.

[203] T.-Y. Hsieh, C.-K. Huang, T.-S. Su, C.-Y. Hong, and T.-C. Wei, “Crystal Growth and Dissolution of Methylammonium Lead Iodide Perovskite in Sequential Deposition: Correlation between Morphology Evolution and Photovoltaic Performance,” (eng), *ACS applied materials & interfaces*, vol. 9, no. 10, pp. 8623–8633, 2017.

[204] B. Wang, K. Young Wong, X. Xiao, and T. Chen, “Elucidating the Reaction Pathways in the Synthesis of Organolead Trihalide Perovskite for High-Performance Solar Cells,” *Scientific Reports*, vol. 5, 10557 EP -, 2015.

[205] Manuel Scheel, *Solvent Vapor Annealing and in situ Photoluminescence Measurements of Perovskite Absorber Layers in Photovoltaics*, 2018.

[206] L. Wagner, L. E. Mundt, G. Mathiazhagan, M. Mundus, M. C. Schubert, S. Mastroianni, U. Würfel, A. Hinsch, and S. W. Glunz, “Distinguishing crystallization stages and their influence on quantum efficiency during

perovskite solar cell formation in real-time," *Scientific Reports*, vol. 7, no. 1, p. 14899, 2017.

[207] Z. Ku, Y. Rong, M. Xu, T. Liu, and H. Han, "Full printable processed mesoscopic CH(3)NH(3)PbI(3)/TiO(2) heterojunction solar cells with carbon counter electrode," (eng), *Scientific Reports*, vol. 3, p. 3132, 2013.

[208] A. Mei, X. Li, L. Liu, Z. Ku, T. Liu, Y. Rong, M. Xu, M. Hu, J. Chen, Y. Yang, M. Gratzel, and H. Han, "A hole-conductor-free, fully printable mesoscopic perovskite solar cell with high stability," (eng), *Science*, vol. 345, no. 6194, pp. 295–298, 2014.

[209] A. Priyadarshi, L. J. Haur, P. Murray, D. Fu, S. Kulkarni, G. Xing, T. C. Sum, N. Mathews, and S. G. Mhaisalkar, "A large area (70 cm 2) monolithic perovskite solar module with a high efficiency and stability," *Energy & Environmental Science*, vol. 9, no. 12, pp. 3687–3692, 2016.

[210] C.-M. Tsai, G.-W. Wu, S. Narra, H.-M. Chang, N. Mohanta, H.-P. Wu, C.-L. Wang, and E. W.-G. Diau, "Control of preferred orientation with slow crystallization for carbon-based mesoscopic perovskite solar cells attaining efficiency 15%," *Journal of Materials Chemistry A*, vol. 5, no. 2, pp. 739–747, 2017.

[211] M. Mundus, *Ultrashort laser pulses for electrical characterization of solar cells*. [Place of publication not identified]: Fraunhofer Verlag, 2016.

[212] M. Mundus, B. Venkataramanachar, R. Gehlhaar, M. Kohlstädt, B. Niesen, W. Qiu, J. P. Herterich, F. Sahli, M. Bräuninger, J. Werner, J. Hohl-Ebinger, G. Uytterhoeven, U. Würfel, C. Ballif, M. C. Schubert, W. Warta, and S. W. Glunz, "Spectrally resolved nonlinearity and temperature dependence of perovskite solar cells," *Solar Energy Materials and Solar Cells*, vol. 172, pp. 66–73, 2017.

[213] J. Schlipf, P. Docampo, C. J. Schaffer, V. Korstgens, L. Biessmann, F. Hanusch, N. Giesbrecht, S. Bernstorff, T. Bein, and P. Muller-Buschbaum, "A Closer Look into Two-Step Perovskite Conversion with X-ray Scattering," (eng), *The Journal of Physical Chemistry Letters*, vol. 6, no. 7, pp. 1265–1269, 2015.

[214] A. Wakamiya, M. Endo, T. Sasamori, N. Tokitoh, Y. Ogomi, S. Hayase, and Y. Murata, "Reproducible Fabrication of Efficient Perovskite-based Solar Cells: X-ray Crystallographic Studies on the Formation of CH 3 NH 3 PbI 3 Layers," *Chemistry Letters*, vol. 43, no. 5, pp. 711–713, 2014.

[215] V. D'Innocenzo, A. R. Srimath Kandada, M. de Bastiani, M. Gandini, and A. Petrozza, "Tuning the Light Emission Properties by Band Gap Engineering in Hybrid Lead Halide Perovskite," *Journal of the American Chemical Society*, vol. 136, no. 51, pp. 17730–17733, 2014.

[216] G. Grancini, V. D'Innocenzo, E. R. Dohner, N. Martino, Srimath Kandada, A. R., E. Mosconi, F. de Angelis, H. I. Karunadasa, E. T. Hoke, and A. Petrozza, "CH 3 NH 3 PbI 3 perovskite single crystals: surface photophysics and their interaction with the environment," *Chemical Science*, vol. 6, no. 12, pp. 7305–7310, 2015.

[217] G. Grancini, A. R. Srimath Kandada, J. M. Frost, A. J. Barker, M. de Bastiani, M. Gandini, S. Marras, G. Lanzani, A. Walsh, and A. Petrozza, "Role of microstructure in the electron–hole interaction of hybrid lead halide perovskites," *Nature Photonics*, vol. 9, no. 10, pp. 695–701, 2015.

[218] C. Quarti, G. Grancini, E. Mosconi, P. Bruno, J. M. Ball, M. M. Lee, H. J. Snaith, A. Petrozza, and F. de Angelis, "The Raman Spectrum of the CH3NH3PbI3 Hybrid Perovskite: Interplay of Theory and Experiment," (ENG), *The Journal of Physical Chemistry Letters*, vol. 5, no. 2, pp. 279–284, 2014.

[219] S. Mastroianni, F. D. Heinz, J.-H. Im, W. Veurman, M. Padilla, M. C. Schubert, U. Würfel, M. Grätzel, N.-G. Park, and A. Hinsch, "Analysing the effect of crystal size and structure in highly efficient CH3NH3PbI3 perovskite solar cells by spatially resolved photo- and electroluminescence imaging," (eng), *Nanoscale*, vol. 7, no. 46, pp. 19653–19662, 2015.

[220] H. Diab, C. Arnold, F. Lédée, G. Trippé-Allard, G. Delport, C. Vilar, F. Bretenaker, J. Barjon, J.-S. Lauret, E. Deleporte, and D. Garrot, "Impact of Reabsorption on the Emission Spectra and Recombination Dynamics of Hybrid Perovskite Single Crystals," (eng), *The Journal of Physical Chemistry Letters*, vol. 8, no. 13, pp. 2977–2983, 2017.

[221] B.-W. Park, N. Kedem, M. Kulbak, D. Y. Lee, W. S. Yang, N. J. Jeon, J. Seo, G. Kim, K. J. Kim, T. J. Shin, G. Hodes, D. Cahen, and S. I. Seok, "Understanding how excess lead iodide precursor improves halide perovskite solar cell performance," *Nature communications*, vol. 9, no. 1, p. 3301, 2018.

[222] T. J. Jacobsson, J.-P. Correa-Baena, E. Halvani Anaraki, B. Philippe, S. D. Stranks, M. E. F. Bouduban, W. Tress, K. Schenk, J. Teuscher, J.-E. Moser, H. Rensmo, and A. Hagfeldt, "Unreacted PbI2 as a Double-Edged Sword for Enhancing the Performance of Perovskite Solar Cells," (eng), *Journal of the American Chemical Society*, vol. 138, no. 32, pp. 10331–10343, 2016.

[223] F. Liu, Q. Dong, M. K. Wong, A. B. Djurišić, A. Ng, Z. Ren, Q. Shen, C. Surya, W. K. Chan, J. Wang, A. M. C. Ng, C. Liao, H. Li, K. Shih, C. Wei, H. Su, and J. Dai, "Is Excess PbI 2 Beneficial for Perovskite Solar Cell Performance?," *Advanced Energy Materials*, vol. 6, no. 7, p. 1502206, 2016.

[224] D. H. Cao, C. C. Stoumpos, C. D. Malliakas, M. J. Katz, O. K. Farha, J. T. Hupp, and M. G. Kanatzidis, "Remnant PbI 2 an unforeseen necessity in high-efficiency hybrid perovskite-based solar cells?," *APL Materials*, vol. 2, no. 9, p. 91101, 2014.

[225] K. Galkowski, A. A. Mitioglu, A. Surrente, Z. Yang, D. K. Maude, P. Kossacki, G. E. Eperon, J. T.-W. Wang, H. J. Snaith, P. Plochocka, and R. J. Nicholas, "Spatially resolved studies of the phases and morphology of methylammonium and formamidinium lead tri-halide perovskites," (eng), *Nanoscale*, vol. 9, no. 9, pp. 3222–3230, 2017.

[226] Z. Song, J. Werner, N. Shrestha, F. Sahli, S. de Wolf, B. Niesen, S. C. Watthage, A. B. Phillips, C. Ballif, R. J. Ellingson, and M. J. Heben, "Probing Photocurrent Nonuniformities in the Subcells of Monolithic Perovskite/Silicon Tandem Solar Cells," (eng), *The Journal of Physical Chemistry Letters*, vol. 7, no. 24, pp. 5114–5120, 2016.

[227] S. Wieghold, J.-P. Correa-Baena, L. Nienhaus, S. Sun, K. E. Shulenberger, Z. Liu, J. Tresback, S. S. Shin, M. G. Bawendi, and T. Buonassisi, "Precursor Concentration Affects Grain Size, Crystal Orientation, and Local Performance in Mixed-Ion Lead Perovskite Solar Cells," *ACS Applied Energy Materials*, 2018.

[228] P. S. C. Schulze, A. J. Bett, K. Winkler, A. Hinsch, S. Lee, S. Mastroianni, L. E. Mundt, M. Mundus, U. Würfel, S. Glunz, M. Hermle, and J. C. Goldschmidt, "Novel Low-Temperature Process for Perovskite Solar Cells with a Mesoporous TiO2 Scaffold," (eng), *ACS applied materials & interfaces*, vol. 9, no. 36, pp. 30567–30574, 2017.

[229] S. Rafizadeh, K. Wienands, L. E. Mundt, A. J. Bett, P. S. C. Schulze, L. Cojocaru, L. C. Andreani, M. Hermle, S. W. Glunz, and J. C. Goldschmidt, "The Impact of the Thickness of the Charge Transportation Layers for the Crystallization and Optoelectronic Performance of Hybrid Evaporated-Spincoated Perovskite Solar Cells," *submitted for publication*.

[230] J. Kim, M. I. Saidaminov, H. Tan, Y. Zhao, Y. Kim, J. Choi, J. W. Jo, J. Fan, R. Quintero-Bermudez, Z. Yang, L. N. Quan, M. Wei, O. Voznyy, and E. H. Sargent, "Amide-Catalyzed Phase-Selective Crystallization Reduces Defect Density in Wide-Bandgap Perovskites," (eng), *Advanced Materials*, vol. 30, no. 13, e1706275, 2018.

[231] K. Sveinbjörnsson, K. Aitola, J. Zhang, M. B. Johansson, X. Zhang, J.-P. Correa-Baena, A. Hagfeldt, G. Boschloo, and E. M. J. Johansson, "Ambient air-processed mixed-ion perovskites for high-efficiency solar cells," *Journal of Materials Chemistry A*, vol. 4, no. 42, pp. 16536–16545, 2016.

[232] K. A. Bush, N. Rolston, A. Gold-Parker, S. Manzoor, J. Hausele, Z. J. Yu, J. A. Raiford, R. Cheacharoen, Z. C. Holman, M. F. Toney, R. H. Dauskardt, and M. D. McGehee, "Controlling Thin-Film Stress and Wrinkling during Perovskite Film Formation," *ACS Energy Letters*, vol. 3, no. 6, pp. 1225–1232, 2018.

[233] C. Haase and H. Stiebig, "Thin-film silicon solar cells with efficient periodic light trapping texture," *Applied Physics Letters*, vol. 91, no. 6, p. 61116, 2007.

[234] O. Höhn, N. Tucher, and B. Bläsi, "Impact of front side pyramid size on the light trapping performance of wafer based silicon solar cells and modules," in *Proceedings of the 44th IEEE Photovoltaic Specialists Conference (PVSC)*, Washington D.C., 2017.

[235] J. Oh, H.-C. Yuan, and H. M. Branz, "An 18.2%-efficient black-silicon solar cell achieved through control of carrier recombination in nanostructures," *Nature Nanotechnology*, vol. 7, 743 EP -, 2012.

[236] H. Savin, P. Repo, G. von Gastrow, P. Ortega, E. Calle, M. Garín, and R. Alcubilla, "Black silicon solar cells with interdigitated back-contacts achieve 22.1% efficiency," *Nature Nanotechnology*, vol. 10, 624 EP -, 2015.

[237] N. Tucher, J. Eisenlohr, H. Gebrewold, P. Kiefel, O. Höhn, H. Hauser, J. C. Goldschmidt, and B. Bläsi, "Optical simulation of photovoltaic modules with multiple textured interfaces using the matrix-based formalism OPTOS," *Optics Express*, vol. 24, no. 14, pp. A1083, 2016.

[238] N. Tucher, A.-K. Volk, J. Seiffe, H. Hauser, C. Müller, and B. Bläsi, "Large-area honeycomb texturing of Si-solar cells via nanoimprint lighography," in *Proceedings of the 29th European Photovoltaic Solar Energy Conference and Exhibition (EUPVSEC)*, Amsterdam, The Netherlands, 2014, pp. 1006–1011.

[239] K. X. Wang, Z. Yu, V. Liu, Y. Cui, and S. Fan, "Absorption Enhancement in Ultrathin Crystalline Silicon Solar Cells with Antireflection and Light-Trapping Nanocone Gratings," *Nano letters*, vol. 12, no. 3, pp. 1616–1619, 2012.

[240] J. Zhao, A. Wang, M. A. Green, and F. Ferrazza, "19.8% efficient "honeycomb" textured multicrystalline and 24.4% monocrystalline silicon solar cells," *Applied Physics Letters*, vol. 73, no. 14, pp. 1991–1993, 1998.

[241] A. R. Pascoe, S. Meyer, W. Huang, W. Li, I. Benesperi, N. W. Duffy, L. Spiccia, U. Bach, and Y.-B. Cheng, "Enhancing the Optoelectronic Performance of Perovskite Solar Cells via a Textured CH 3 NH 3 PbI 3 Morphology," *Advanced Functional Materials*, vol. 26, no. 8, pp. 1278–1285, 2016.

[242] M. Jošt, S. Albrecht, L. Kegelmann, C. M. Wolff, F. Lang, B. Lipovšek, J. Krč, L. Korte, D. Neher, B. Rech, and M. Topič, "Efficient Light Management by

Textured Nanoimprinted Layers for Perovskite Solar Cells," *ACS Photonics*, vol. 4, no. 5, pp. 1232–1239, 2017.

[243] A. Sharenko and M. F. Toney, "Relationships between Lead Halide Perovskite Thin-Film Fabrication, Morphology, and Performance in Solar Cells," (eng), *Journal of the American Chemical Society*, vol. 138, no. 2, pp. 463–470, 2016.

[244] M. I. Dar, A. Hinderhofer, G. Jacopin, V. Belova, N. Arora, S. M. Zakeeruddin, F. Schreiber, and M. Grätzel, "Function Follows Form: Correlation between the Growth and Local Emission of Perovskite Structures and the Performance of Solar Cells," *Advanced Functional Materials*, vol. 27, no. 26, p. 1701433, 2017.

[245] D. Bi, J. Luo, F. Zhang, A. Magrez, E. N. Athanasopoulou, A. Hagfeldt, and M. Grätzel, "Morphology Engineering: A Route to Highly Reproducible and High Efficiency Perovskite Solar Cells," (eng), *ChemSusChem*, vol. 10, no. 7, pp. 1624–1630, 2017.

[246] D. Forgács, M. Sessolo, and H. J. Bolink, "Lead acetate precursor based p-i-n perovskite solar cells with enhanced reproducibility and low hysteresis," *Journal of Materials Chemistry A*, vol. 3, no. 27, pp. 14121–14125, 2015.

[247] J. P. Correa Baena, L. Steier, W. Tress, M. Saliba, S. Neutzner, T. Matsui, F. Giordano, T. J. Jacobsson, A. R. Srimath Kandada, S. M. Zakeeruddin, A. Petrozza, A. Abate, M. K. Nazeeruddin, M. Grätzel, and A. Hagfeldt, "Highly efficient planar perovskite solar cells through band alignment engineering," *Energy & Environmental Science*, vol. 8, no. 10, pp. 2928–2934, 2015.

[248] H. Tan, A. Jain, O. Voznyy, X. Lan, F. P. García de Arquer, J. Z. Fan, R. Quintero-Bermudez, M. Yuan, B. Zhang, Y. Zhao, F. Fan, P. Li, L. N. Quan, Y. Zhao, Z.-H. Lu, Z. Yang, S. Hoogland, and E. H. Sargent, "Efficient and stable solution-processed planar perovskite solar cells via contact passivation," (eng), *Science*, vol. 355, no. 6326, pp. 722–726, 2017.

[249] D. Yang, X. Zhou, R. Yang, Z. Yang, W. Yu, X. Wang, C. Li, S. Liu, and Chang, Robert P. H., "Surface optimization to eliminate hysteresis for record efficiency planar perovskite solar cells," *Energy & Environmental Science*, vol. 9, no. 10, pp. 3071–3078, 2016.

[250] H. Yoon, S. M. Kang, J.-K. Lee, and M. Choi, "Hysteresis-free low-temperature-processed planar perovskite solar cells with 19.1% efficiency," *Energy & Environmental Science*, vol. 9, no. 7, pp. 2262–2266, 2016.

[251] J. You, L. Meng, T.-B. Song, T.-F. Guo, Y. Yang, W.-H. Chang, Z. Hong, H. Chen, H. Zhou, Q. Chen, Y. Liu, and N. de Marco, "Improved air stability of perovskite solar cells via solution-processed metal oxide transport layers," *Nature Nanotechnology*, 2015.

[252] W. Chen, Y. Wu, Y. Yue, J. Liu, W. Zhang, X. Yang, H. Chen, E. Bi, I. Ashraful, M. Gratzel, and L. Han, "Efficient and stable large-area perovskite solar cells with inorganic charge extraction layers," *Science*, vol. 350, no. 6263, pp. 944–948, 2015.

[253] W. Chen, F.-Z. Liu, X.-Y. Feng, A. B. Djurišić, W. K. Chan, and Z.-B. He, "Cesium Doped NiO x as an Efficient Hole Extraction Layer for Inverted Planar Perovskite Solar Cells," *Advanced Energy Materials*, vol. 7, no. 19, p. 1700722, 2017.

[254] J. W. Jung, C.-C. Chueh, and A. K.-Y. Jen, "A Low-Temperature, Solution-Processable, Cu-Doped Nickel Oxide Hole-Transporting Layer via the Combustion Method for High-Performance Thin-Film Perovskite Solar Cells," (eng), *Advanced Materials*, vol. 27, no. 47, pp. 7874–7880, 2015.

[255] Y. Bai, H. Chen, S. Xiao, Q. Xue, T. Zhang, Z. Zhu, Q. Li, C. Hu, Y. Yang, Z. Hu, F. Huang, K. S. Wong, H.-L. Yip, and S. Yang, "Effects of a Molecular Monolayer Modification of NiO Nanocrystal Layer Surfaces on Perovskite Crystallization and Interface Contact toward Faster Hole Extraction and Higher Photovoltaic Performance," *Advanced Functional Materials*, vol. 26, no. 17, pp. 2950–2958, 2016.

[256] C. Chen, G. Yang, J. Ma, X. Zheng, Z. Chen, Q. Zhang, and G. Fang, "Surface treatment via Li-bis-(trifluoromethanesulfonyl) imide to eliminate the hysteresis and enhance the efficiency of inverted perovskite solar cells," *Journal of Materials Chemistry C*, vol. 5, no. 39, pp. 10280–10287, 2017.

[257] A. Tejada, S. Braunger, L. Korte, S. Albrecht, B. Rech, and J. A. Guerra, "Optical characterization and bandgap engineering of flat and wrinkle-textured FA 0.83 Cs 0.17 Pb(I 1–x Br x) 3 perovskite thin films," *Journal of applied physics*, vol. 123, no. 17, p. 175302, 2018.

[258] C. M. Wolff, F. Zu, A. Paulke, L. P. Toro, N. Koch, and D. Neher, "Reduced Interface-Mediated Recombination for High Open-Circuit Voltages in CH3 NH3 PbI3 Solar Cells," (eng), *Advanced Materials*, vol. 29, no. 28, 2017.

[259] M. Abdi-Jalebi, Z. Andaji-Garmaroudi, S. Cacovich, C. Stavrakas, B. Philippe, J. M. Richter, M. Alsari, E. P. Booker, E. M. Hutter, A. J. Pearson, S. Lilliu, T. J. Savenije, H. Rensmo, G. Divitini, C. Ducati, R. H. Friend, and S. D. Stranks, "Maximizing and stabilizing luminescence from halide perovskites with potassium passivation," (eng), *Nature*, vol. 555, no. 7697, pp. 497–501, 2018.

[260] B. Wenger, P. K. Nayak, X. Wen, S. V. Kesava, N. K. Noel, and H. J. Snaith, "Consolidation of the optoelectronic properties of CH3NH3PbBr3 perovskite single crystals," *Nature communications*, vol. 8, no. 1, p. 590, 2017.

[261] Laura E. Mundt, Wolfram Kwapil, Mohammed A. Yakoob, Jan P. Herterich, Markus Kohlstädt, Uli Würfel, Martin C. Schubert, and Stefan W. Glunz, "Quantitative Local Loss Analysis of Blade Coated Perovskite Solar Cells," *submitted for publication*.

[262] M. Kohlstädt, M. A. Yakoob, and U. Würfel, "A Matter of Drying: Blade-Coating of Lead Acetate Sourced Planar Inverted Perovskite Solar Cells on Active Areas >1 cm 2," *physica status solidi (a)*, vol. 26, p. 3, 2018.

[263] A. Pisoni, J. Jaćimović, O. S. Barišić, M. Spina, R. Gaál, L. Forró, and E. Horváth, "Ultra-Low Thermal Conductivity in Organic-Inorganic Hybrid Perovskite CH3NH3PbI3," (eng), *The Journal of Physical Chemistry Letters*, vol. 5, no. 14, pp. 2488–2492, 2014.

[264] H. Straube, O. Breitenstein, and J.-M. Wagner, "Thermal wave propagation in thin films on substrate: The time-harmonic thermal transfer function," *physica status solidi (b)*, vol. 218, n/a-n/a, 2011.

[265] H. Straube and O. Breitenstein, "Infrared lock-in thermography through glass substrates," *Solar Energy Materials & Solar Cells*, vol. 95, no. 10, pp. 2768–2771, 2011.

[266] M. Padilla, B. Michl, B. Thaidigsmann, W. Warta, and M. C. Schubert, "Short-circuit current density mapping for solar cells," *Solar Energy Materials and Solar Cells*, vol. 120, pp. 282–288, 2014.

[267] C. Barugkin, J. Cong, T. Duong, S. Rahman, H. T. Nguyen, D. Macdonald, T. P. White, and K. R. Catchpole, "Ultralow Absorption Coefficient and Temperature Dependence of Radiative Recombination of CH 3 NH 3 PbI 3 Perovskite from Photoluminescence," (englisch), *The Journal of Physical Chemistry Letters*, vol. 6, no. 5, pp. 767–772, 2015.

[268] T. J. Jacobsson, L. J. Schwan, M. Ottosson, A. Hagfeldt, and T. Edvinsson, "Determination of Thermal Expansion Coefficients and Locating the Temperature-Induced Phase Transition in Methylammonium Lead Perovskites Using X-ray Diffraction," (eng), *Inorganic Chemistry*, vol. 54, no. 22, pp. 10678–10685, 2015.

[269] Y. Yamada, T. Nakamura, M. Endo, A. Wakamiya, and Y. Kanemitsu, "Near-band-edge optical responses of solution-processed organic–inorganic hybrid perovskite CH 3 NH 3 PbI 3 on mesoporous TiO 2 electrodes," *Applied Physics Express*, vol. 7, no. 3, p. 32302, 2014.

[270] H. Nesswetter, P. Lugli, A. W. Bett, and C. G. Zimmermann, "Electroluminescence and Photoluminescence Characterization of Multijunction Solar Cells," *IEEE Journal of Photovoltaics*, vol. 3, no. 1, pp. 353–358, 2013.

[271] S. Roensch, R. Hoheisel, F. Dimroth, and A. W. Bett, “Subcell I-V characteristic analysis of GaInP/GaInAs/Ge solar cells using electroluminescence measurements,” *Appl Phys Lett*, vol. 98, no. 25, p. 251113, 2011.

[272] L. E. Mundt, M. C. Schubert, J. Schon, B. Michl, T. Niewelt, F. Schindler, and W. Warta, “Spatially Resolved Impurity Identification via Temperature- and Injection-Dependent Photoluminescence Imaging,” *IEEE Journal of Photovoltaics*, vol. 5, no. 5, pp. 1503–1509, 2015.

[273] C. Yi, J. Luo, S. Meloni, A. Boziki, N. Ashari-Astani, C. Grätzel, S. M. Zakeeruddin, U. Röthlisberger, and M. Grätzel, “Entropic stabilization of mixed A-cation ABX 3 metal halide perovskites for high performance perovskite solar cells,” *Energy & Environmental Science*, vol. 9, no. 2, pp. 656–662, 2016.

Publications

Peer-reviewed journal publications

(sorted by date of publication)

1) L. Cojocaru, K. Wienands, Ulas Erdil, P.S.C. Schulze, **L.E. Mundt**, A.J. Bett, M. Breitwieser, F. Lombeck, M. Prescher, L. Kirste, J.C. Goldschmidt, S.W. Glunz, "*Hybrid Evaporation/Spray-Coating Process for a Simplified and Controllable Production of Perovskite Solar Cells*", (submitted)
   DOI:

2) P.S.C. Schulze, K. Wienands, A.J. Bett, S. Rafizadeh, **L.E. Mundt,** L. Cojocaru, M. Hermle, S.W. Glunz, J.C. Goldschmidt, "*High Bandgap Perovskite Deposition via a Hybrid Evaporation/ Spin Coating Method for Application in Fully Textured Monolithic Silicon-Based Tandem Stacks*", (submitted)
   DOI:

3) S. Rafizadeh, K. Wienands, **L.E. Mundt,** A.J. Bett, P.S.C. Schulze, L. Cojocaru, L. Andreani, M. Hermle, S.W. Glunz, J.C. Goldschmidt, "*The Impact of the Thickness of Charge Transportation Layers for the Crystallization and Optoelectronic Performance of Hybrid Evaporated-Spincoated Perovskite Solar Cells*", (submitted)
   DOI:

4) M. Niemeyer, P. Kleinschmidt, **L.E. Mundt**, C. Tumm, T. Hannappel, D. Lackner, "*Measurement Method for the Determination of the Nonradiative Recombination Lifetime and the Radiative Recombination Coefficient in Direct Semiconductors*", (submitted)
   DOI:

5) **L.E. Mundt**, W. Kwapil, M. Yakoob, J. Herterich, M. Kohlstädt, U. Würfel, M.C. Schubert, S.W. Glunz, "*Quantitative Local Loss Analysis of Blade Coated Perovskite Solar Cells*", IEEE Journal of Photovoltaics vol. 9 (2), pp. 452 - 459, 2019
   DOI: 10.1109/JPHOTOV.2018.2888835

6) S. Braunger, **L.E. Mundt**, C. Wolff, M. Mews, C. Rehermann, M. Jost, A. Tejada, D. Eisenhauer, C. Becker , J.A. Guerra, E. Unger, L. Korte, D Neher, M.C. Schubert, B. Rech, S. Albrecht, "*$Cs_xFA_{1-x}Pb(I_{1-y}Br_y)_3$ Perovskite Compositions: the Appearance of Wrinkled Morphology and its Impact on Solar Cell Performance*", Journal of Physical Chemistry C, 122 (30), pp. 17123–17135, 2018
DOI: 10.1021/acs.jpcc.8b06459

7) S. Mastroianni, L. Wagner, L.S. Subramaniam, S. Chacko, K. Yasaroglu, W. Kwapil, **L.E. Mundt**, M.C. Schubert, T. Kroyer, A. Hinsch, "*Optimization of Electron Selective Layer and Perovskite Crystallization for Efficient Outdoor and Indoor Light Harvesting in Graphite-Based Perovskite Solar Cells*", Proceedings of 3rd International Conference on Perovskite Thin Film Photovoltaics, Photonics and Optoelectronics, 2018
DOI: 10.29363/nanoge.abxpvperopto.2018.077

8) L. Wagner, **L.E. Mundt**, G. Mathiazhagen, M. Mundus, M.C. Schubert, S. Mastroianni, U. Würfel, A. Hinsch, S.W. Glunz, "*Distinguishing crystallization stages and their influence on quantum efficiency during perovskite solar cell formation in real-time*", Scientific Reports vol. 7: 14899, pp. 1-6, 2017
DOI: 10.1038/s41598-017-13855-6

9) A.J. Bett, P.S.C. Schulze, K. Winkler, J. Gasparetto, P.F. Ndione, M. Bivour, A. Hinsch, M. Kohlstädt, S. Lee, S. Mastroianni**, L.E. Mundt**, M. Mundus, C. Reichel, A. Richter, C. Veit, K. Wienands, U. Würfel, W. Veurman, S.W. Glunz, M. Hermle, J.C. Goldschmidt, "*Low temperature perovskite solar cells with an evaporated TiO_2 compact layer for perovskite silicon tandem solar cells*", Energy Procedia vol. 124, pp. 567-576, 2017
DOI: 10.1016/j.egypro.2017.09.293

10) P.S.C. Schulze, A.J. Bett, K. Winkler, A. Hinsch, S. Lee, S. Mastroianni, **L.E. Mundt**, M. Mundus, U. Würfel, S.W. Glunz, M. Hermle, J.C. Goldschmidt, "*Novel Low-Temperature Process for Perovskite Solar Cells with a Mesoporous TiO_2 Scaffold*", ACS applied materials & interfaces vol. 9 (36), pp. 30567-3057, 2017
DOI: 10.1021/acsami.7b05718

11) **L.E. Mundt**, F.D. Heinz, S. Albrecht, M. Mundus, M. Saliba, J.P. Correa-Baena, E.H. Anaraki, L. Korte, M. Grätzel, A. Hagfeld, B. Rech, M.C. Schubert, S.W. Glunz, "*Nondestructive Probing of Perovskite Silicon Tandem Solar Cells Using Multiwavelength Photoluminescence Mapping*", IEEE Journal of Photovoltaics vol. 7 (4), pp. 1081-1056, 2017
DOI: 10.1109/JPHOTOV.2017.2688022

12) S.-W. Lee, S. Kim, S. Bae, K. Cho, T. Chung, **L. E. Mundt**, S. Lee, S. Park, H. Park, M. C. Schubert, S. W. Glunz, Y. Ko, Y. Jun, Y. Kang, H.-S. Lee, D. Kim, "*UV Degradation and Recovery of Perovskite Solar Cells*", Scientific Reports vol. 6: 38150, pp. 1-10, 2016
DOI: 10.1038/srep38150

13) J. Schön, A. Youssef, S. Park, **L.E. Mundt**, T. Niewelt, S. Mack, K. Nakajima, K. Morishita, R. Murai, M.A. Jensen, T. Buonassisi, M.C. Schubert, "*Identification of Lifetime Limiting Defects by Temperature- and Injection-Dependent Photoluminescence Imagings*", Journal of Applied Photovoltaics vol. 120 (10), pp. 105703, 2016
DOI: 10.1063/1.4961465

14) F.D. Heinz, **L.E. Mundt**, W. Warta, M.C. Schubert, "*A Combined Transient and Steady State Approach for Robust Lifetime Spectroscopy with Micrometer Resolution*", physica status solidi (RRL) vol. 9 (12), pp. 697-700, 2015
DOI: 10.1002/pssr.201510364

15) F.D. Heinz, J. Giesecke, **L.E. Mundt**, M. Kasemann W. Warta, M.C. Schubert, "*On the Implication of Spatial Carrier Density Non-Uniformity on Lifetime Determination in Silicon*", Journal of Applied Physics vol. 118 (10), pp. 105706, 2015
DOI: 10.1063/1.4930799

16) M.C. Schubert, M. Padilla, B. Michl, **L.E. Mundt**, J. Giesecke, J. Hohl-Ebinger, J. Benick, W. Warta, M. Tajima, A. Ogura, "*Iron Related Solar Cell Instability: Imaging Analysis and Impact on Cell Performance*", Solar Energy Materials and Solar Cells vol. 138, pp. 96-101, 2015
DOI: 10.1016/j.solmat.2015.03.001

17) **L.E. Mundt**, M.C. Schubert, J. Schön, B. Michl, T. Niewelt, F. Schindler, W. Warta, "*Spatially Resolved Impurity Identification via Temperature- and Injection-Dependent Photoluminescence Imaging*", IEEE Journal of Photovoltaics vol. 5 (5), pp. 1503-1509, 2015
DOI: 10.1109/JPHOTOV.2015.2447837

Contributions to conferences and workshops

(sorted by date of presentation, presenting author(s) underlined)

1) MRS 2018:

L. Rakocevic, **L.E. Mundt**, R. Gehlhaar, T. Merckx, T. Aernouts, M.C. Schubert, S.W. Glunz, J. Poortmans, "*Area Loss Analysis of Perovksite Modules Using Thermography and Luminescence Imaging*"

- Poster presentation

2) PSCO 2018:

L. Rakocevic, **L.E. Mundt**, R. Gehlhaar, T. Aernouts, M.C. Schubert, S.W. Glunz, J. Poortmans, "*Luminescence Imaging Characterization of Perovskite Modules*"

- Poster presentation

3) PSCO 2018:

P.S.C. Schulze, Ö. Kabakli, M. Daub, I. Ketterer, **L.E. Mundt**, A.J. Bett, Y. Wu, S.W. Glunz, H. Hillebrecht, J.C. Goldschmidt, "*Spoilt for choice – perovskite bandgap tuning for monolithic perovskite/silicon tandem devices*"

- Poster presentation

4) WCPEC-7 2018:

L. Mundt, M. Yakoob, J. Herterich, M. Kohlstädt, U. Würfel, M.C. Schubert, S.W. Glunz, "*Quantitative Local Loss Analysis of Blade Coated Perovskite Solar Cells*"

- Oral presentation
- Nominated for Best Student Paper Award
- Paper invited for publication in IEEE Journal of Photovoltaics

5) HOPV 2018:

S. Rafizadeh, K.Wienands, **L.E. Mundt**, A.J. Bett, P.S. C. Schulze, L. Cojocaru, L.C. Andreani, M. Hermle, S.W. Glunz, J.C. Goldschmidt, "*Record Stabilized Efficiencies Exceeding 18% for Hybrid Evaporation-Spincoating Planar Perovskite Solar Cells*"

- Poster presentation

6) HOPV 2018:

M. Kohlstädt, M. A. Yakoob, J. Herterich, **L.E. Mundt**, U. Würfel, " *From Cell to Mini-Module – Blade Coating and Controlled Drying for Planar Inverted Perovskite Solar Cells*"

- Poster presentation

7) ABXPV 2018:

S. Mastroianni, L. Wagner, S.L.Subramaniam, S. Chacko, W.Kwapil, **L.E. Mundt**, M.C.Schubert, T.Kroyer, A.Hinsch, "*Optimization of Electron-Selective Layer and Perovskite Crystallization for Efficient Outdoor and Indoor Light Harvesting in Graphite-Based Perovskite Solar Cells*"

- Poster presentation

8) SiliconFOREST 2017:

L.E. Mundt, S. Braunger, S. Albrecht, M.C. Schubert, S.W. Glunz, "*Orts- und Tiefenaufgelöste Charakterisierung von Perowskit-Silizium-Tandemsolarzellen"*

- Oral presentation

9) PSCO 2017:

L. Wagner, **L.E. Mundt**, G. Mathiazhagan, M. Mundus, M.C. Schubert, S. Mastroianni, U. Würfel, A. Hinsch, S.W. Glunz, "*Closing the Gap: Real-Time Photovoltaic Evolvement During Perovskite Crystallization"*

- Oral presentation

10) PSCO 2017:

S.L. Subramaniam, **L.E. Mundt**, S. Mastroianni, M.C. Schubert , A. Hinsch, "*Dark Lock-In Thermography Characterization: Towards a Pin-Hole Free Hole-Blocking Layer for Perovskite Solar Cells"*

- Poster presentation

11) ICMAT 2017:

L. Wagner, **L.E. Mundt**, G. Mathiazhagan, M. Mundus, M.C. Schubert, S. Mastroianni, U. Würfel, A. Hinsch and S.W. Glunz, "*Monitoring Of Crystallization Kinetics In Graphite Based Perovskite Solar Cells"*

- Poster presentation

12) HOPV 2017:

S.L. Subramaniam, S. Chacko, K. Yasaroglu, W. Kwapil, **L.E. Mundt**, B.K. Das, M.C. Schubert, T. Kroyer, S. Mastroianni, A. Hinsch, "*Optimization of Electron-Transport Layer in Perovskite Solar Cells by Characterization using Dark Lock-in Thermography"*

- Poster presentation

13) Silicon PV 2017:

A.J. Bett, P.S.C. Schulze, K. Winkler, J. Gasparetto, P. Ndione, M. Bivour, A. Hinsch, M. Kohlstädt, S. Lee, S. Mastroianni, **L.E. Mundt**, M. Mundus, C. Reichel, A. Richter, N. Tucher, C. Veit, K. Wienands, U. Würfel, W. Veurman, M.C. Schubert, S.W. Glunz, M. Hermle, J.C. Goldschmidt, "*Low-Temperature Perovskite Solar Cells for Tandem Applications"*

- Poster presentation

14) PSCO 2016:

L.E. Mundt, F.D. Heinz, S. Albrecht, L. Korte, M. Saliba, J.P. Correa-Baena, E. Halvani Anaraki, B. Rech, M.C. Schubert, S.W. Glunz, "*A Glance Inside Monolithic Tandem Solar Cells"*

- Poster presentation

15) Energy International Joint R&D Program Workshop 2016:

L.E. Mundt, B. Michl, S. Mastroianni, M.C. Schubert, W. Warta, S.W. Glunz, S.W. Lee, S. Bae, S. Kim, S. Park, S. Lee, H. Park, D. Kim, "*Hybrid Silicon Solar Cells with Advanced Layer System Including Perovskite"*

- Oral presentation

16) PSCO 2015:

L.E. Mundt, F.D. Heinz, S. Mastroianni, M.C. Schubert, S.W. Glunz, "*Micro-Spectroscopic Characterization of Perovskite Films"*

- Poster presentation

17) Energy International Joint R&D Program Workshop, 2015:

L.E. Mundt, B. Michl, S. Mastroianni, M.C. Schubert, W. Warta, S.W. Glunz, S. Park, S. Lee, H. Park, S. Kim, D. Kim, "*Hybrid Silicon Solar Cells with Advanced Layer System Including Perovskite"*

- Oral presentation

List of Figures

List of Tables

Acknowledgements

It has been a joy and a privilege to spend the past years amongst so many intelligent, spirited and kind individuals. I am truly grateful for each and every person who was part of this unique experience “PhD thesis”.

I would like to thank Prof. Dr. Stefan Glunz for the academic supervision, for his unmatched dedication to ISE festivities, for raising me in the ISE spirit and for cheering at my kickboxing match. I thank Prof. Dr. Steve Albrecht for his examination of this thesis and for the fruitful collaboration throughout the past years.

I thank Dr. Martin Schubert for giving me the opportunity to do my PhD at Fraunhofer ISE, for his guidance and encouragement. Also for the fact that he, unlike me, never lost faith in the success of my work.

To Janosch, Uli, Markus, Alexander, Patricia and the entire perovskite working group: thank you for the numerous collaborations and discussions.

For proof-reading the bits and pieces of this thesis, I want to thank Martin, Wolfram, Dave, Giles, Tim, Freddie and Jens.

Special gratitude goes to the entire characterization group and the D311 originals: Freddie – for the crack and the light. Tim – for all the chocolate and simply for being you. Wolfram – for all the early morning coffee. Flori – for each any every concert. And as a ghost of the past I thank Päivikki, both her spirit and her spirits still linger in the office. Of course I also thank the new girls’ gang in D311, Hannah and Rebekka, for putting up with my writing-mania and for every surprised look on peoples’ faces as they enter an office full of female scientists.

It is a great comfort to know that there are capable and couragous people looking out for the ISE employees. I am deeply impressed by such dedication and grateful to be part of the „Betriebsrat“.

To the members of the Kickbox Team Freiburg: thank you for all the exhausting practice sessions, for keeping me from going crazy at work.

I feel very grateful to my flatmate Sarah for her company, following our heroine Alanna and our friend Fitz. To Jens, for countless gin & tonic sessions and Lorettoberg walks. And to Dave for believing in me and for restoring contrast, as well as the entire Colorado-crew for rescuing me out of my writing-mania.

I thank my sister Sarah for going first and for raising the bar. For relieving me from the need to outdo her and instead leaving me being impressed and proud of the first Dr. Mundt.

Finally, I wholeheartedly thank my parents for their unconditional love and support. For giving me both roots and wings. For everything.

"...it's like this. Sometimes, when you've a very long street ahead of you, you think how terribly long it is and feel sure you'll never get it swept.

And then you start to hurry. You work faster and faster and every time you look up there seems to be just as much left to sweep as before, and you try even harder, and you panic, and in the end you're out of breath and have to stop--and still the street stretches away in front of you. That's not the way to do it.

You must never think of the whole street at once, understand? You must only concentrate on the next step, the next breath, the next stroke of the broom, and the next, and the next. Nothing else.

That way you enjoy your work, which is important, because then you make a good job of it. And that's how it ought to be.

And all at once, before you know it, you find you've swept the whole street clean, bit by bit. what's more, you aren't out of breath. That's important, too..."

Michael Ende, Momo